On the Scale Interaction between African Easterly Waves and Convection

by

Bruce, Ting-Hsin Kuo

B.S., Atmospheric Sciences
National Taiwan University, 1989

M.S., Atmospheric Sciences
National Taiwan University, 1991

SUBMITTED IN PARTIAL FULFILLMENT OF THE REQUIREMENTS
FOR THE DEGREE OF

MASTER OF SCIENSE

at the

MASSACHUSETTES INSTITUTE OF TECHNOLOGY
August, 1998

Signature of Author_____
Department of Earth, Atmospheric and Planetary Sciences
Massachusettes Institute of Technology

Certified by_____
Kerry A. Emanuel
Professor of Meteorology
Thesis Supervisor

Accepted by_____
Ronald G. Prinn
Professor of Atmospheric Chemistry and Department Head

On the Scale Interaction between African Easterly waves and Convection

by

Bruce Ting-Hsin Kuo

Submitted to the Massachusettes Institute of Technology/Department of Earth, Atmospheric, and Planetary Sciences on August 24, 1998, in partial fulfillment of the requirements for the degree of Master of Science

ABSTRACT

In this study a β-plane quasi-geostrophic channel model is used to study the dynamics of African waves. In part I the structure and energetics of the African easterly waves are well replicated compared to observations. Highly simplified physical processes, including Ekman damping and relaxation, are included to study the dynamic equilibrium problem. Similar to the results of observation, the barotropic process is important during the linear stage of the life cycle. The structure during the nonlinear stage is similar to observations, especially the upper-level meridional wind field. During the nonlinear stage, baroclinic processes dominate. Afterwards, the system reaches saturation and stays in an oscillatory state due to the nonlinear wave-mean flow interaction.

Simple bulk aerodynamic formulae are used to parameterize the surface heat fluxes. Ekman damping works to spin down the circulation. Relaxation is used to restore the zonal mean field back to its initial condition and works a simple way to mimic the radiative processes which maintains the strength of the environment. The experiment with Ekman damping and relaxation shows that the system reaches a state of dynamic equilibrium. The relaxation restores the strength of the jet and the kinetic energy is dissipated due to Ekman damping. The results of different sensitivity experiments are compared to the control run to see the effects of parameterized processes.

In part II we deal with the quasi-equilibrium problem. Wind-induced heat and water vapor fluxes from the ocean surface are also calculated using the bulk aerodynamic formulae. By adopting the Emanuel convection scheme, we put together different diabatic processes including

radiative cooling, Ekman damping and convection. Although physical processes are idealized, the results demonstrate strong interaction between the circulation of African disturbances and convection. The scenario is that the African waves works as the synoptic-scale forcing to modify the entropy of the subcloud layer. Convection, in response to the large-scale forcing, redistributes the heat and water vapor upward. The interaction of convection and African easterly waves ultimately reaches a state of quasi-equilibrium.

Two-dimensional perturbations are introduced at the lower boundary as the system reaches a two-dimensional equilibrium state. The structure and evolution of the African easterly waves are well replicated. The results show that wave disturbances grow in the expense of zonal mean available potential energy and kinetic energy trough barotropic and baroclinic energy conversions. The trough has a cold core below and warm core above structure. The geographic distribution of precipitation rate shows that the convection is enhanced by the dynamic forcing of the approaching mid-level trough of the African waves. The structure and evolution of the African disturbances is modified by the convective processes. The results show much resemblance to the observations.

Sensitivity experiments show that higher SST with fixed temperature gradient results in higher and weaker jet and weaker vertical wind shear below the jet. According to Miller and Lindzen's results, the effect of higher SST on jet properties is a possible cause that leads to later organization of convections over the Atlantic. Larger temperature gradient with fixed SST gives rise to a stronger jet. The results are insensitive to the initial background humidity but sensitive to the surface water vapor flux over the land.

Acknowledgement

Acknowledgement is the hardest part of my thesis to write. So many people have helped me wholeheartedly. I would like to take this chance to say thank you.

First of all I would like to thank my advisor Professor Emanuel. He is so elegant in not only scientific research but also teaching. I learned a lot from my advisor in his courses and his attitude toward scientific research. He inspired me with his unique way of attacking scientific problems. If there was a chance, I would like to work with him again. I also want to thank Professor Lindzen for his generous support using his project. His critique about the research paper helped me improve my thesis to the form it is.

This thesis could not have come to the status it is without the work of others. Rebecca gave me some direction to run the quasi-geostrophic model when she was very busy preparing her general examination. She gave me many hand-on experience about this model that really helped a lot. During my study at MIT I received countless help and comfort from my best friends, they are Becky Hsieh, I-Ching Wu, Yuku, Sofia Kuo, Chin Wu, Yuan-Long Hu, Ginger Wang, Catherine Hsieh, Yi-jan Chen, etc. They made my life here much easier and happier and gave me very sweet memory of my graduate study at MIT.

Most of all, I would like to thank my families, my dear parents, brother, and three sisters for their full support and love. They are my inspiration. Without them none of this would be possible. I love them and miss them. Hope God blesses my dear families and lovely friends.

Table of Content

List of Figures and Tables

Chapter 1

Introduction

1.1 General Remarks

Summer convection is an important feature over tropical Africa and the Atlantic ocean (Duvel, 1990). Observations indicated that the cloudiness and convection over West Africa and the north Atlantic region are usually associated with African wave activity (Carlson 1969; Frank 1969; Duvel 1990). Convective systems such as cloud clusters and squall lines are sometimes triggered or enhanced by the approach of a mid-level trough in the easterlies (Aspliden *et al.* 1976; Frank 1978; Thompson *et al.* 1979). The maximum cloud amount does not show any preference in location (Burpee 1972). Many numerical experiments support the idea that the vertical wind shear associated with African easterly jet supports the long-lived squall lines in the tropical Atlantic region (Moncrieff and Miller 1976; Raymond 1984; Rotunno *et al.* 1988). In the GATE region, the easterly flow at 600 mb usually moves faster than the trough axis. The associated distribution of divergence field thus favors convection to the west of the trough (Frank 1978). African waves are also often observed to precede the occurrence of tropical cyclones (Anthes, 1982). It is frequently stated that tropical cyclogenesis in the eastern Pacific Ocean occurs in association with easterly waves that have propagated from Africa across the Atlantic and Caribbean and into the eastern Pacific (Avila 1991; Avila and Pasch 1992). Some of the Atlantic disturbances developed into hurricanes that threatened North America. Table 1 shows some statistics about the African wave related tropical systems for the Atlantic basin during 1991-1993.

Many theories have been proposed to explain the dynamic link between convection and African waves. However, their interactive relationships remain to be determined. Considering so many devastating convective systems (e.g. thunderstorms, squall lines and hurricanes) relevant to the African jet and its accompanied wave disturbances, the issues deserve our consideration.

Table 1: Three years of statistics about African waves related tropical systems in the Atlantic basin. The ratios indicate the number between that of tropical systems related to African waves and the total number of tropical systems in a year, where - means data unclear (AW, TD and TS are African waves, tropical depression and tropical storm, respectively).

Year	number of AWs	TDs	TSs	Hurricanes
1991	73	7/-	3/11	0/4
1992	69	4/9	1/6	1/4
1993	70	-	9/10	0/0

Cyclonic storms of low pressure that move from west to east across the Sahel during the rainy season (usually defined in this region from June to September), called African wave disturbances, are one of the most important mechanisms to modify Sahel summer precipitation. During this century, the Sahelian region on the southern fringes of the Sahara, which is affected by these waves, has experienced considerable interannual variability in summer rainfall. Drought is still severe and has continued since 1968 (Lamb 1982). Recent West African drought is found relevant to the anomalous SST and tropical atmospheric circulation although the dynamic causes are not completely ascertained. One possible cause is that SST anomalies associated with observed dry years reduced rainfall over West Africa because of weaker monsoon flow from the Gulf of Guinea (Semazzi *et al.* 1993). A zonally symmetric model has been used to study the monsoon circulation as a thermal direct circulation (Plumb and Hou 1992; Zheng 1997). The change in SST of the Gulf of Guinea mainly comes from the variability in the strength of upwelling (Bakun 1978; Bah 1987). Dry (wet) years in the Sahel are characterized by the presence of warm (cold) surface waters in almost all the Gulf of Guinea (Lamb 1978). Several studies (Kidson 1977; Newell and Kidson 1984; Landsea and Gray 1992; Druyan 1989; Druyan and Hall 1996; Fontaine *et al.* 1995; Jenkins 1997) show there are stronger 700-mb easterly winds near $15°N$, and a weaker tropical easterly jet near 200 mb during dry years. These results again presume that summer convection and rainfall over the east Atlantic region

and West Africa is dynamically linked to the activity of African Waves and African easterly jet from short-term and/or long-term climatological point of view.

1.2 Observed Behavior

The GARP Atlantic Tropical Experiment (GATE) was the first project with dense observations designed to understand the interactions between convective activity and large-scale weather systems (ICSU/WMO,1972). Some of the main achievements of this experiment included the identification of the African wave disturbances and their origin, the portrait of their structure, and advanced understanding of their behavior and properties, e.g., Reed *et al.* (1977), Norquist *et al.* (1977), Stevens 1979; Thompson *et al.* (1979), Reeves *et al.* (1979), and Chen and Ogura (1982). Nitta (1977) postulated that the appearance of the jet wind profile seems to act as an obstacle for the downward penetration of the downdraft. He also suggested the importance of the interaction between downdrafts and vertical wind shear.

Some other pioneer studies based on non-GATE data include Carlson (1969), Burpee (1972) and Mass (1977). Substantial differences in wave characteristics, large-scale environments and energetics between tropical western Pacific and eastern Atlantic regions were highlighted by Thompson *et al.* (1979). These observational analyses are usually used to evaluate the results of numerical modelling.

Output data from ECMWF analyses have also been used to study African waves. For example, Reed *et al.* (1988) used ECMWF analyses 700-mb bandpass vorticity variances to identify the tracks of African waves. Their results identified two preferred tracks for easterly waves—one track near $15°N$, the other track near $8°N$. The two tracks combine into one over the Atlantic. Druyan *et al.* (1996) used ECMWF gridded analyses and Niamey station data to examine the synoptic circumstances associated with the occurrence of precipitation at Niamey during July-August 1987 and 1988. They found that occasionally heavy precipitation can result from uplift driven by upper tropospheric divergence which is related to the upper-level Tropical easterly jet ($\sim$200mb). Druyan *et al.* (1997) used ECMWF reanalyses of two different horizontal resolution and Niamey station data to diagnose the spatial distributions of meteorological and kinematic fields including several synoptic cases. They found that vertical

motion patterns at 500 mb are not well correlated with areas of low-level convergence and wave troughs.

1.3 Previous Numerical and Theoretical Studies

African wave disturbances are a particularly inviting target for numerical simulation because of the inherently diverse scales involved including cumulus-scale and/or meso-scale convections, synoptic-scale African waves and large-scale monsoonal flow. A number of investigators have constructed numerical models to explore the genesis, evolution and energetics of African waves and their interaction with convections. For example, Mass (1977) used a linearized primitive equation model to perform a numerical study. Kwon (1989), Kwon and Mak (1990) used a quasi-geostrophic model to reexamine the genesis of African waves and compare the cases with and without a tropical easterly jet. Thorncroft and Hoskins (1994, part I, II, III) used a baroclinic spectral model developed by Hoskins and Simmons (1975) with enhanced resolution to study diabatic effects on the evolution and structure of African waves. Nonlinear evolution and equilibration of shear instability were also discussed in their papers (Part II). Paradise *et al.* (1995) used a linearized non-hydrostatic model to study the relationship between African waves and convection. Basically, these numerical studies focused on the structure and energetics of the African waves, and the effect of convections on the large-scale systems. Their results indicated the critical role of vertical shear in the growth rate, wavelength, induced ascent and low-level convergence. All these experiments can be thought of initial value problems since their results are sensitive to the prescribed initial state, including the properties of the African jet.

One theory to explain the organization of rainfall by African waves is the wave-CISK theory (Lindzen 1974; Raymond 1975, 1976; Stark 1976; Steven et al. 1977). However, as addressed by Stevens and Lindzen (1978), wave-CISK models produce a horizontal scale which is not compatible with the observed length scale. Miller and Lindzen (1992) proposed that rainfall is organized only if the unstable jet is within a few kilometers of the moist layer and separated by large shear. This criterion is necessary for the African waves, which originate from shear instability of the unstable jet, to induce sufficient amplitude of ascent.

1.4 The Role of Convection

Since the scale jump between cumulus convections and African waves is too large for large-scale models to explicitly resolve the convection, their effects are usually parameterized. To account for the effects of convection, most of the above numerical and dynamical models adopted CISK-type schemes (Rennick 1976- Mass 1977; Kwon 1989; Paradis et al. 1995; Thorncroft and Hoskins 1994). The heating and moistening profiles in CISK-type scheme are prescribed functions of height. These schemes are too simple to capture the essence of the rather complicated convective processes and will result in unrealistic vertical heating and moistening effects. Small errors in the determination of cumulus heating can produce very large errors in the difference between heating and adiabatic cooling and will thus result in large errors in the dynamics of circulations in convecting atmospheres (Emanuel 1987, Emanuel *et al.* 1994). In this paper, the Emanuel scheme (Emanuel 1991), which is built on the basis of cloud thermodynamics and microphysics (Rennó et al.,1994), is employed to deal with the convective processes.

The characteristic of tropical soundings is a manifestion of convective adjustment responding to the large-scale forcing. The tropical atmosphere is convectively adjusted on a time scale that is rather short compared to the time scale for substantial change in large-scale destabilization for convection. It's the near balance between the input of convective potential energy by large-scale processes and its consumption by convection that highlights the concept of quasi-equilibrium advanced by Arakawa and Schubert (1974). Large-scale thermodynamical forcing that forces convection in this model includes radiative cooling, advective processes and boundary fluxes. Xu and Emanuel (1989) suggested that further investigations of large-scale tropical circulations should focus on processes that affect the subcloud layer entropy content. Since cumulus convection works as an agent to redistribute the heat acquired from the ocean surface upward, it is more critical to understand the physical and dynamic processes that lead to the actual addition of surface heat flux rather than the convection itself. African waves may work as large-scale disturbances to modify the subcloud layer entropy by wind induced sensible heat exchange (WISHE) processes.

The air-sea interaction theory has been applied to explain the development and maintenance of tropical cyclones (Emanuel 1986; Rotunno and Emanuel 1987), and simulate the intraseasonal oscillations in the tropics (Emanuel 1987; Neelin *et al.* 1987). The air-sea interaction processes

are considered in this paper, whereby surface fluxes are parameterized using the simple bulk aerodynamic formulae described in chapter 2.

1.5 Methodology

As described in section 1.3, most of the numerical studies treated the African wave dynamics as an initial value problem. This type of studies focused on the structure, energetics and evolution. The results can be verified by comparing with observational evidence. Studies of this category can also be used to test the accuracy and validation of a numerical model. In this thesis I treat the initial value problem first in part I. The basic condition for part I is constructed with analytic functions. Perturbations at the lower boundary are introduced to start the wave disturbances. The time evolution of the model can be compared with the behavior of African waves. Various cross-sections will be presented to demonstrate the internal structure of the wave disturbances.

However, the tropical atmosphere is not far away from a state of convective quasi-equilibrium since the time-scale for the convection to consume the instability is short compared to the accumulation of instability by large-scale forcing. It is instructive to investigate how convection, as responding to the large-scale forcing, interacts with African waves. The equilibrium state is itself critical to illustrate the impact of convection on the large-scale circulation and the behavior of the African waves. In part II, we only prescribe the sensible heat and water vapor fluxes from the lower boundary and a constant tropospheric radiative cooling rate to study the equilibrium state of the system. After reaching equilibrium, the perturbations will be put in at the lower boundary with small initial amplitude. The methodology here is to numerically simulate the African waves and incorporate the effects of convection using the Emanuel scheme without the need to prescribe the African jet, which is taken to be a dynamic response to the unique distribution of meridional surface temperature over North Africa and the Gulf of Guinea. Under the hypothesis of quasi-equilibrium, we are interested in understanding what the equilibrium state is and how African waves and convection interact. What is the result as the system reaches the state of quasi-equilibrium with and without African waves? How do African waves change the surface fluxes? Does it lead to the organization of convection? What are the

effects of convections on the large-scale circulation and African waves? The results will provide some clues to resolve the dynamic relationship between the African waves and convection. The quasi-equilibrium hypothesis helps us to make this argument clear.

One important feature of the Emanuel scheme to be noted here is the explicit hypothesis of quasi-equilibrium. Thus, the final equilibrium state is more meaningful than any particular transient state. A test of the more restrictive strict quasi-equilibrium hypothesis(SQE) on long temporal and spatial scales that assumes changes in CAPE are dynamically negligible are performed by Brown and Bretherton (1997).

In essence, we want the model to be simple so we can clearly interpret the dynamics of the system. Hence, we choose a β-plane quasi-geostrophic channel model to study the proposed internal baroclinic instability problem associated with the African easterly jet. The β-plane quasi-geostrophic model is described in section 1.6. Chapter 2 contains the zonally symmetric experiments with assigned initial jet structure. The construction of the initial condition is explained in section 2.1. Section 2.2 surveys the stability of the constructed basic state. The control run and its results will be portrayed in chapter 3. Chapter 4 describes several experiments with different simplified physical processes. Part II starts with chapter 5, which explains the physical processes. Chapter 6 includes the control run of the boundary value problem. Section 6.2 surveys the stability of the equilibrium state. Some sensitivity experiments are performed and discussed in chapter 7. Chapter 8 contains the African wave experiments. Conclusions are presented in chapter 9. Appendix 1 lists the energy equations and some basic formulae. In appendix 2 and 3, we collect the observational results concerning the structure and energetics of African waves for comparison.

1.6 β-plane Quasi-Geostrophic Channel Model

To justify the usage of the quasi-geostrophic model in the simulation of African waves over the tropical region, we start with some scaling arguments and observational evidence to support the methodology. The center of the African easterly jet is climatologically located at $20^{\circ}N$ with a typical wind velocity scale of 10 $m/$ sec, Buoyancy frequency N of 0.01 $\sec^{-1}$ and scale height of 10 km to do the scaling.

Thus, we have Stratified Rossby radius of

$$L_S = \frac{NH}{f} \sim 2000km.$$

The observed wavelength of the African waves is order of 2500km. Hence, the scale of the African waves that we are interested in has similar length scale to the Stratified Rossby radius, i.e.,

$$L \sim L_S.$$

We also have an aspect ratio of

$$\delta = \frac{H}{L} \sim 3.34 \times 10^{-3},$$

Rossby number

$$\varepsilon = \frac{U}{fL} \sim 0.08 - 0.2,$$

External Rossby radius

$$R = \frac{\sqrt{gH}}{f} \sim 6286km,$$

and Froude number of

$$F = (\frac{L_S}{R})^2 \sim 0.13.$$

To verify β-plane approximation, we have

$$\beta_0 L_y / f_0 = 0.343$$

with L_y of 800km. The above scaling parameters show that the quasi-geostrophic model with the β-plane approximation is still a valid tool for the scale and area we considered in this study. Although the domain in the meridional direction used in this experiment extends to 3000km, we are only interested in the central strip zone of about 1500km. The extension in domain is to reduce the impact of boundary reflection in the channel model.

As pointed out by Hoskins *et al.* (1985), the dynamics of large scales are best understood by considering the conservation of potential vorticity following the motion. The essence of potential vorticity theory is that the flow redistributes potential vorticity, and the new flow is uniquely

determined by the new distribution of potential vorticity (Robinson 1987). In quasi-geostrophic theory, we can derive pseudo-potential vorticity, which is very useful since streamfunction and geostrophic velocity can be obtained through three dimensional invertability. The prognostic variables in the quasi-geostrophic model are pseudo-potential vorticity in the interior and potential temperature at the upper and lower boundaries (Charney and Stern,1962). When the motion is adiabatic and frictionless, the pseudo-potential vorticity is conserved following the horizontal geostrophic wind. When convection is considered, there is a source/sink term due to condensation or evaporation of water substance. That is

$$\frac{\partial q_g}{\partial t} + J(\psi, q_g) = \rho_s^{-1} \frac{\partial}{\partial z}(\frac{\rho_s}{S}\frac{H}{C_p}). \tag{1.1}$$

The diabatic heating H due to convective processes is calculated through the Emanuel scheme. $q_g = \beta y + \frac{\partial^2 \overline{\psi}}{\partial y^2} + \rho_s^{-1}\frac{\partial}{\partial z}(\rho_s S^{-1}\frac{\partial \overline{\psi}}{\partial z})$ is the pseudo-potential vorticity; $S = (N(z)/f_0)^2$ is the static stability parameter. The prognostic equations for the lower and upper boundaries are

$$(\frac{\partial}{\partial t} + V_g \cdot \nabla)\theta_i = \frac{Q}{C_p}, \tag{1.2}$$

where i represents the top or bottom boundary. Thus with eq. (2.1) and (2.2) the time evolution of pesudo-potential vorticity can be evaluated.

The integrations are performed in a zonally periodic channel centered at $20°N$ with width of $3000km$ in the y direction, and with height of $20km$ in the z direction. The model domain in the x direction allows two wavelengths. The resolution is $100km$ in horizontal directions, and $500m$ in the z direction. The time step is chosen to be 8 minutes for computational stability. The numerical scheme for time integration is Euler forward scheme for the first time step only and Leap-frog scheme after. A time filter is applied to damp the computational model. The spatial discretization is a second-order centered difference scheme. The boundary conditions for this model are walls at the north and south boundaries, periodic in the east and west boundaries, and rigid at the upper and lower horizontal boundaries.

Part I

Initial Value Problem

Chapter 2

Model Formulation

2.1 Construction of the Basic State

The basic state in part I is constructed using analytical functions. The characteristics of the basic state are controlled by prescribing five parameters. The zonal wind structure is a very important feature in the simulation of African waves since the African easterly jet is the principal dynamic source of the waves, as emphasized by Rennick (1976), Simmons (1977), Mass (1977), and Kwon (1989). The zonal wind of the basic state is analytically expressed as

$$\overline{u}(y,z) = U \cdot F(y) \cdot G(z), \tag{2.1}$$

with

$$F(y) = \frac{1}{2}\left[\tanh(\frac{y-y_1}{L_1}) - \tanh(\frac{y-y_2}{L_2})\right]$$

and

$$G(z) = \frac{1}{2}\left[\tanh(\frac{z-z_1}{H_1}) - \tanh(\frac{z-z_2}{H_2})\right],$$

where $y_1 = 1100km$, $y_2 = 1950km$, $z_1 = 1500m$, and $z_2 = 5950m$. The African easterly jet core is centered at $20°N$, at $Z = 3400m$ with a maximum easterly wind of $15m/s$. Note that, for simplicity, features such as the tropical easterly jet and low-level westerlies are absent. The zonal current of the jet stream has both horizontal and vertical shears in structure. The meridional shear is $2.5 \times 10^{-5}s^{-1}$, while shears above and below the jet are, respectively, $2.5 \times 10^{-3}s^{-1}$,

and $6 \times 10^{-3} s^{-1}$. The five control parameters (U, L_1, L_2, H_1, H_2) determine the meridional and vertical wind shears and the intensity of the jet. The reference zonal wind is presented in Fig. 1(a).

Once the zonal wind is constructed, we can use thermal wind balance to get the meridional distribution of potential temperature. Then the base-state potential temperature $\overline{\theta}(y, z)$ can be constructed by superposing the deduced vertical profile and the meridional distribution. The distribution of base-state potential temperature is also shown in Fig. 1(a). The potential temperature increases with latitude in the lower troposphere. The maximum meridional potential temperature gradient is located at $z = 1.5km$. The potential temperature gradient reverses above $z = 3.4km$ with the negative maximum gradient located at about $z = 6.5km$. The potential temperature gradient at the surface is about $3 \times 10^{-3} K/km$, similar to that observed by Reed *et al.*(1977). The buoyancy frequency $N(z) = (\frac{g}{\theta_0} \frac{\partial \overline{\theta}}{\partial z})^{1/2}$ is a function of height and latitude.

2.2 Stability of the Basic State

In general, the necessary condition for instability is that the set of functions

$$(\partial \overline{q}/\partial y)_{interior},$$

$$(\partial \overline{\theta}/\partial y)_{lower},$$

$$-(\partial \overline{\theta}/\partial y)_{upper} \tag{2.2}$$

must not have the same sign throughout, but must include both positive and negative values (Gill, 1982). This is the Charney-Stern criterion for instability (Charney and Stern, 1962). Conversely, a sufficient condition for stability is that they have the same sign everywhere.

To survey the satisfaction of the necessary condition, the distributions of basic state potential vorticity gradient $\overline{q_y}$ is plotted in Fig. 1(b). Since, as shown in Fig. 1(c)., $(\partial \overline{\theta}/\partial y)_{lower}$ is positive, $-(\partial \overline{\theta}/\partial y)_{upper}$ is close to zero, and $(\partial \overline{q}/\partial y)_{interior}$ has $+, -, +$ pattern, we can deduce that the necessary condition is satisfied by the basic state.

Baroclinic instability is associated with vertical shear of the mean flow. Baroclinic insta-

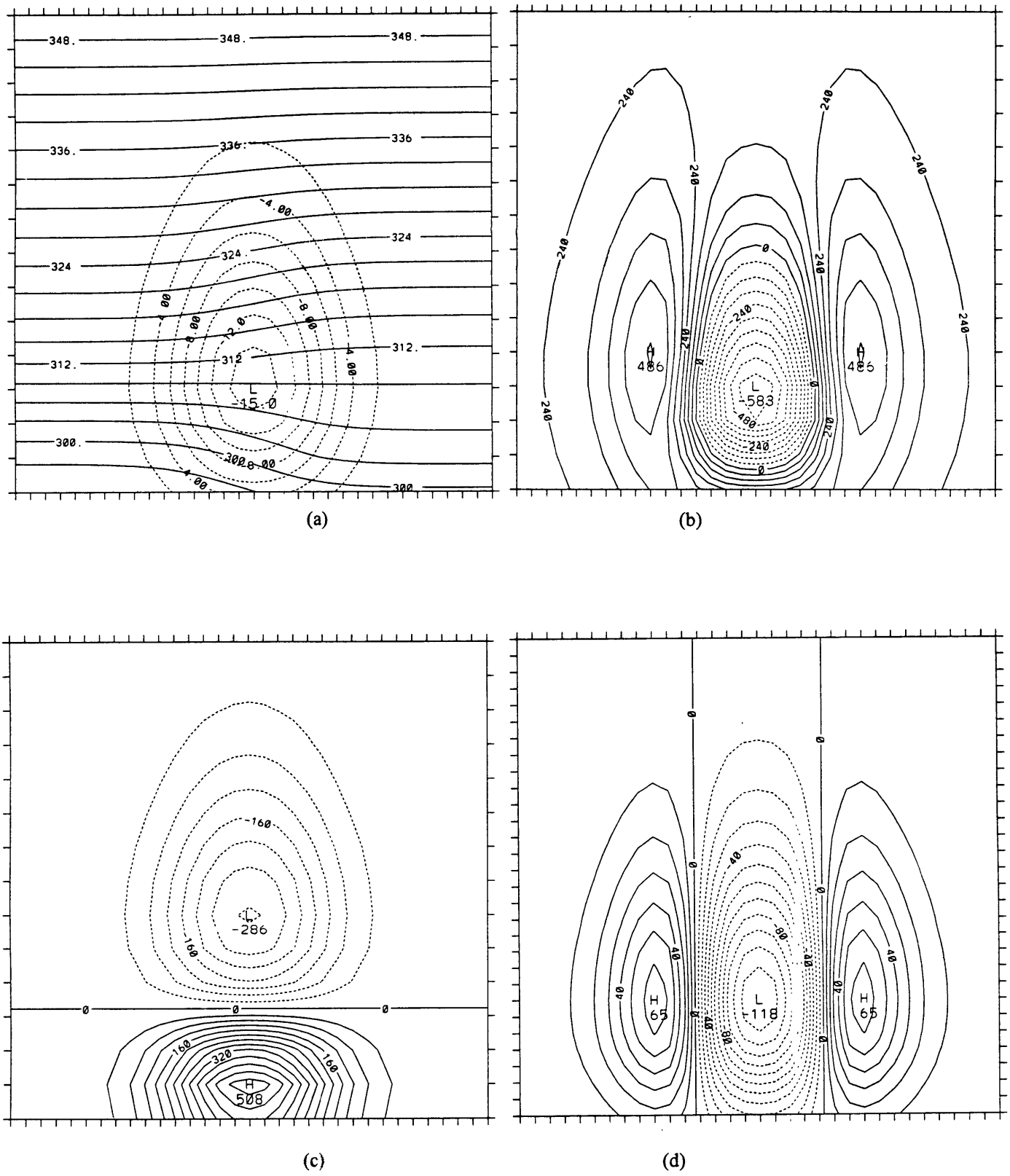

(a) (b)

(c) (d)

Fig. 1: The y-z profile of the initial condition. (a) Basic state zonal wind and potential temperature. (b) Meridional gradient of potential vorticity. (c) Meridional gradient of potential temperature. (d) Meridional gardient of absolute vorticity. The domain is 15 km high and 3200km wide.

bilities grow by converting potential energy associated with the mean horizontal temperature gradient that must exist to provide thermal wind balance for the vertical shear in the basic state flow. Barotropic instability, on the other hand, is a wave instability associated with the horizontal shear in a jetlike current. Barotropic instabilities grow by extracting kinetic energy from the zonal mean flow. Reed *et al.* (1977) show that the zonal current of the African wave disturbances satisfied not only the necessary condition for Charney and Stern instability but also the necessary condition for barotropic instability. That is, the gradient of absolute vorticity must change sign somewhere. Note that the basic state we have used in this simulation does satisfy the barotropic instability criterion as shown in Fig. 1(d).

2.3 Initial Perturbations

To assert that the basic state is stable, it is necessary to show that the initial state is stable with respect to all possible initial disturbances. However, instability may be demonstrated by the presence of a single perturbation ψ' to which the initial state is unstable (Pedlosky, 1979). In this article, a potential temperature perturbation which is zonally periodic at the lower boundary is assigned as the initial disturbance. An important element of potential vorticity theory, first pointed out by Bretherton (1966), is that the potential temperature variations at rigid boundaries have the same effect on the interior flow as do sheets of potential vorticity located just within the boundaries. The potential temperature perturbation will induce a cyclonic circulation when the anomaly is positive and vice versa. The basic state has been described in section 2.1. We will use this basic state to examine the structure and energetics of the African waves in the following two chapters.

Chapter 3

Structure and Evolution

3.1 Vertical Structure

Vertical longitudinal cross-sections at $20°N$ are presented here for fields of meridional wind, temperature, perturbation zonal wind, relative vorticity, perturbation potential vorticity, and vertical velocity at day 7.

The meridional wind shown in Fig. 2(a) has one maximum just below the jet level and another maximum at the surface. The meridional wind composited by Reed *et al.* (1977) also had two maxima, one is just below jet level but the other is at a higher level, above 12km, in disagreement with our results at this moment. It is not surprising to have a maximum at the surface since the initial perturbation is put at the lower boundary. Later evolution at day 17, termed as the nonlinear stage, does have an upper level maximum at about $z = 11km$, as shown in Fig. 2(b). The trough can be identified as the place where meridional velocity is zero and is marked by a heavy solid line in Fig. 2. As shown in Fig. 2(a), the vertical profile of the trough line tilts eastward with height below the jet and tilts westward with height above the jet. The tilting direction is basically against the wind shear vector of the base-state zonal flow and is consistent with the results of Mass (1978). Comparing to Fig. 2(a), the trough line for day 17, as shown in Fig. 2(b), constantly tilts westward with height and looks very similar to the composited result. That is primarily because, during the phase III of GATE, the observed African waves have already gained strong intensity and are therefore in a nonlinear stage of development.

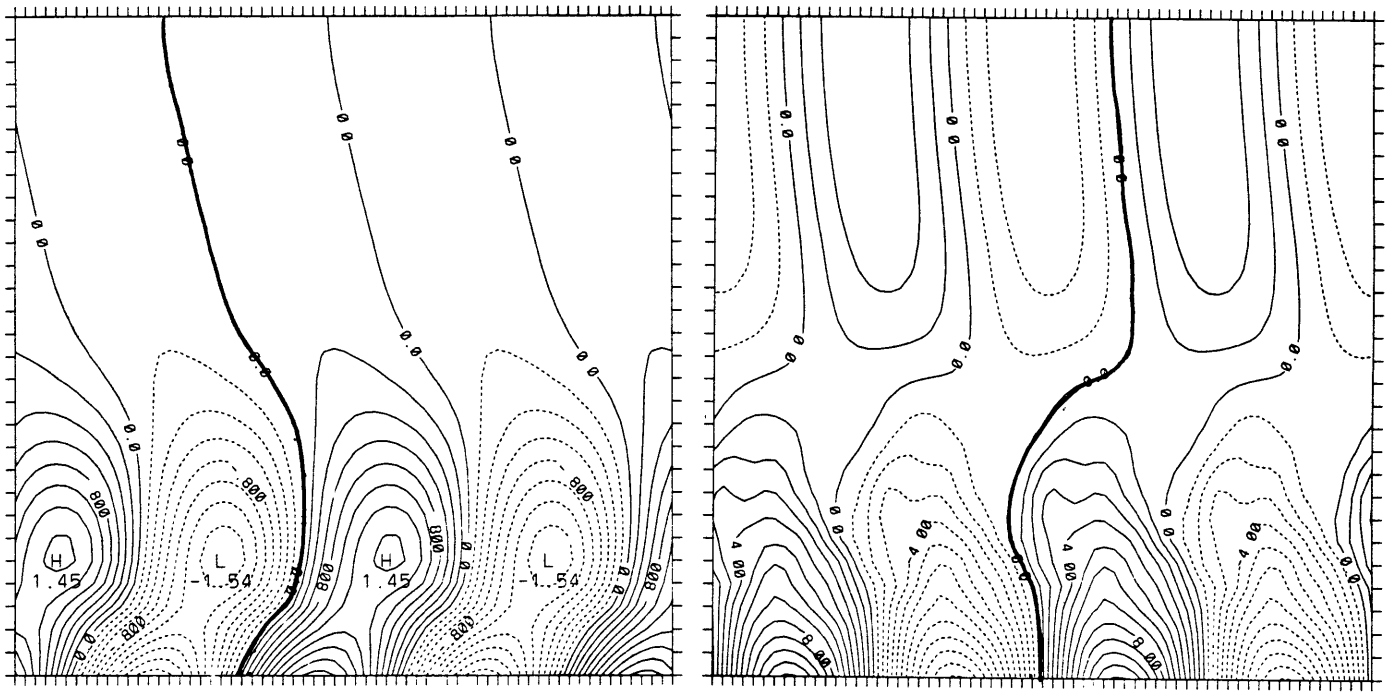

(a) (b)

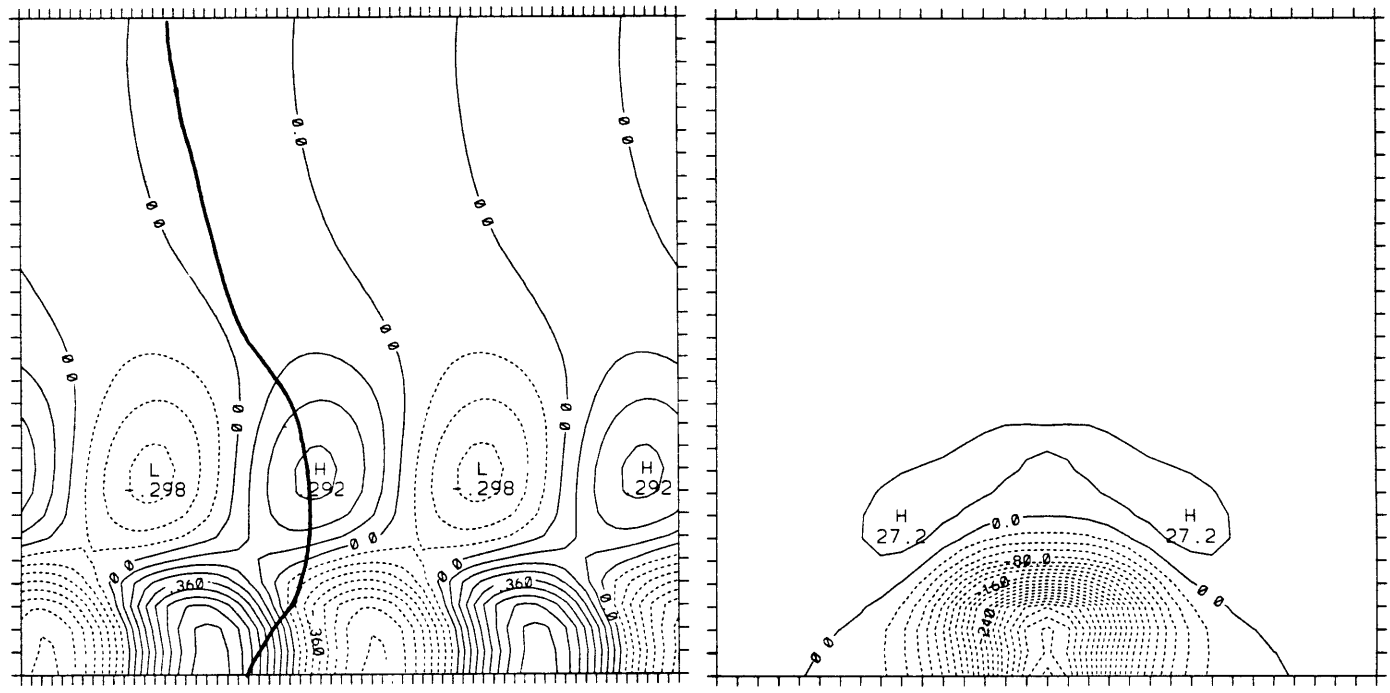

(c) (d)

Fig. 2: The x-z profile the African Easterly waves. (a) Meridional velocity at day 7. (b) Meridional velocity at day 17. (c) Perturbation potential temperature at day 7. (d) Horizontal heat flux. The domain is 15 km high and 6400km wide.

For the cross-sections at $20°N$, the vertical tilts are significant, whereas poleward and equatorward of the jet the tilts become insignificant (not shown here). The temperature field tilts in the opposite sense to the meridional wind below the jet as shown in Fig. 2(c), consistent with a growing baroclinic structure. It should also be noted that at $20°N$ the vertical structure of the trough resembles the letter V with the upper and lower tilts in the right sense for positive baroclinic energy conversions. Corresponding to this structure, we can anticipate warm advection by the northerlies and cold advection by the southerlies below the jet and vice versa above the jet. That is, there are negative northward heat fluxes $\overline{v'\theta'}$ below the jet and positive heat fluxes above the jet, as shown in Fig. 2(d). That is, the eddy heat flux has down gradient transport. With the distribution of base-state potential temperature, there exists positive conversion C_A from zonal mean available potential energy to eddy available potential energy as shown in Fig. 2(e). The positive value is located at lower baroclinic zone. The central part of the trough line in the region of the jet is upright, which implies very small baroclinic energy conversions because only trivial horizontal temperature gradients exist (Fig. 1(c)).

The zonal wind, shown in Fig. 2(f), also has a similar tilting structure. The lower half of the trough falls in the positive zonal wind regime as in Reed *et al.* (1977). The Reynolds stress or horizontal momentum flux $\overline{u'v'}$, as shown in Fig. 2(g), has a positive value in the cyclonic shearing flank and is negative in the anti-cyclonic shearing flank. Again the eddy momentum flux is down-gradient. We see that the maximum v' is located at the lower boundary and at the jet level but the maximum $\overline{u'v'}$ is located at the jet level since the distribution of u' has a maximum value near the jet level. With the distribution of the jet, the conversion from zonal mean kinetic energy to eddy kinetic energy C_K is positive in this structure as shown in Fig. 2(h).

The relative vorticity $\frac{\partial^2\psi}{\partial x^2} + \frac{\partial^2\psi}{\partial y^2}$, in Fig. 3(a) has a maximum of $0.63 \times 10^{-5}\,\mathrm{sec}^{-1}$just below the jet. The GATE composite (Reed *et al.,* 1977) also had maximum just below the jet. In Fig. 3(a) at $20°N$ we identify a secondary maximum at the surface from which there is a clear eastward tilting with height towards the maximum near the jet level; above the jet there is only minor westward tilting with height. The GATE composite of relative vorticity is dominated by cyclonic vorticity around the jet level, with the largest relative anti-cyclonic vorticity above 12km. It is clearly not a simple sinusoidal structure in Reed *et al.*(1977), which suggests that

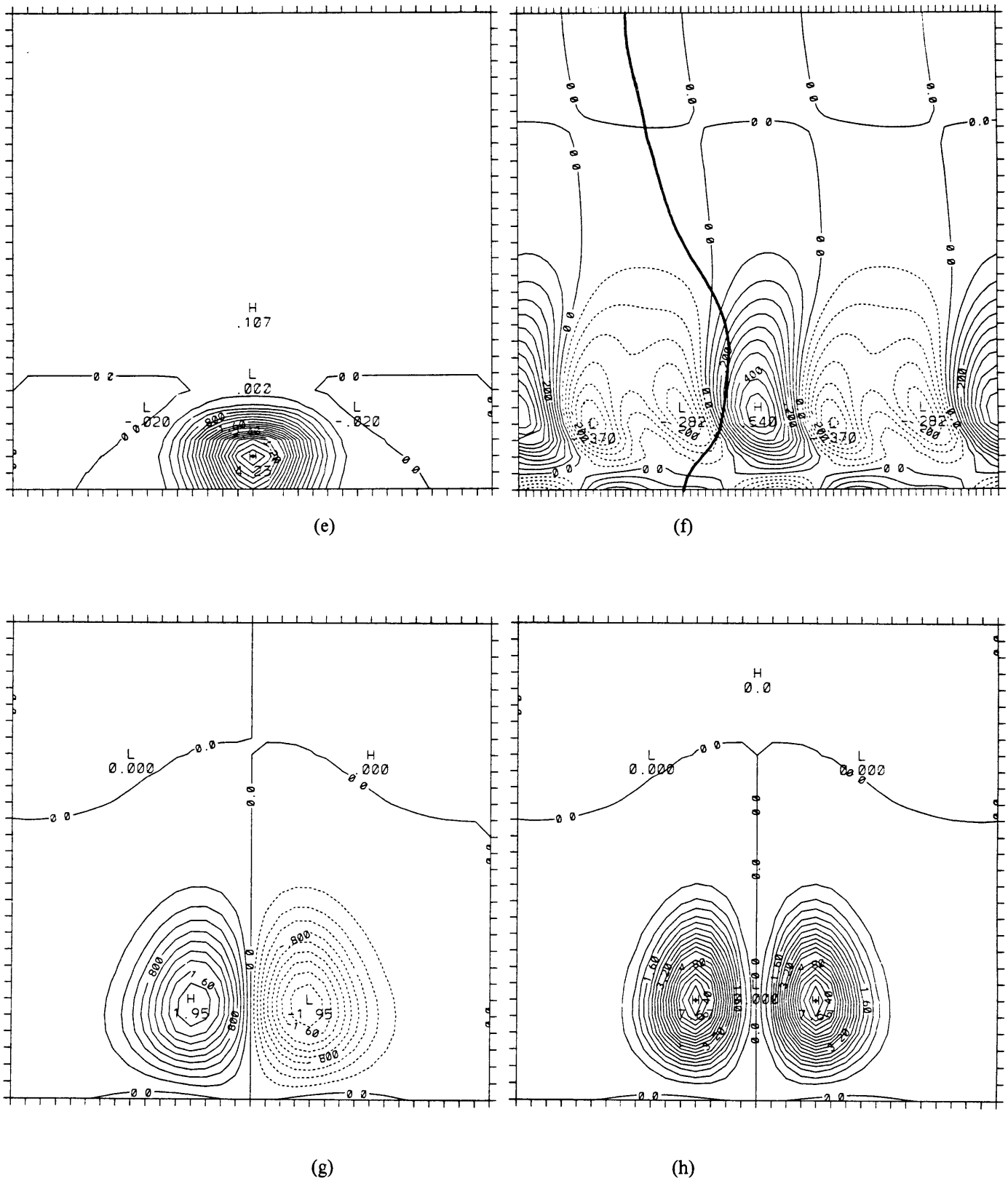

Fig. 2: Continue. (e) Potential energy conversion at day 7. (f) Perturbation zonal velocity at day 7. (g) Horizontal momentum flux at day 7. (h) Barotropic kinetic conversion at day 7.

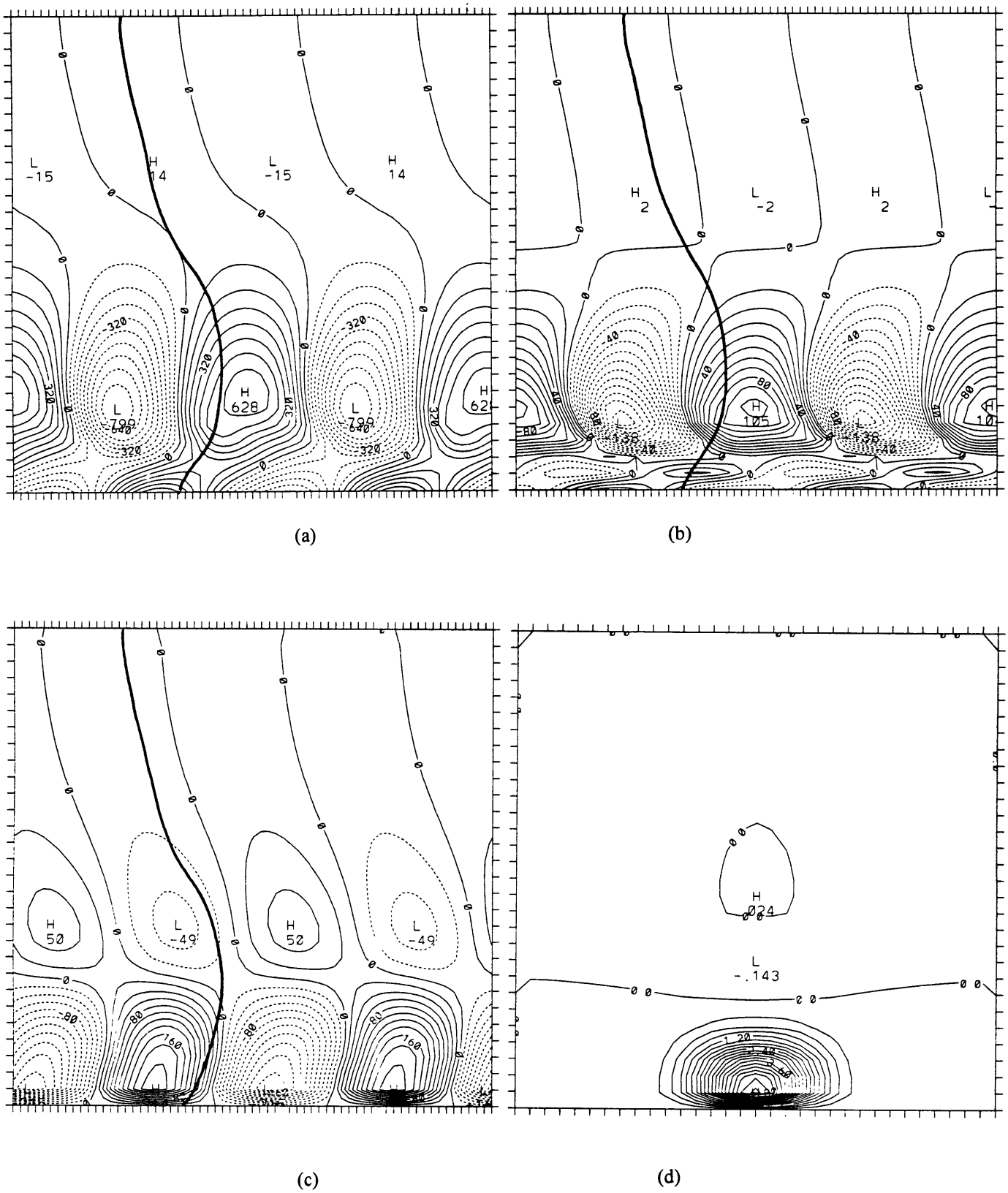

Fig. 3: The x-z profile the African Easterly waves at day 7. (a) Relative vorticity (*10^-8 s^-2). (b) Perturbation potential vorticity (*10^-7 s^-2). (c) Vertical velocity (*10^-5 m/s). (d) Vertical heat flux (K*m/s). The domain is 15 km high and 6400km wide.

moist or nonlinear processes might be important in real situations. Note especially that the trough line is accompanied by positive relative vorticity as observations show. Now turn to see the x-z cross-section of perturbation potential vorticity in Fig. 3(b). Basically, the pattern is similar to relative vorticity with minor difference located below $1km$. They result from the vertical gradient of perturbation potential temperature.

The vertical velocity can be diagnosed from the omega equation. The checkerboard pattern in the vertical velocity, shown in Fig. 3(c), is consistent with quasi-geostrophic theory. A vorticity anomaly on a jet with opposite baroclinicity, above and below, immediately gives this checkerboard pattern (Hoskins and Pedder, 1980). Fig. 3(d) show that the vertical heat fluxes $\overline{w'\theta'}$ are positive. This implies positive baroclinic energy conversion C_E from the eddy available potential energy to eddy kinetic energy through the thermally direct circulation.

3.2 Horizontal Structure

In this section, perturbation fields of potential vorticity and relative vorticity at 3.5 km height and temperature at the lowest level will be used to illustrate the horizontal structure of the African waves. Fig. 4(a) shows the perturbation potential vorticity at $z = 3.5km$. This level is chosen because it transects the jet (Fig. 1(a)). Potential vorticity anomalies are present in the three different regions of potential vorticity gradient (Fig. 1(b)), on the poleward flank, on the equatorward flank and in the jet region itself. The largest potential vorticity anomalies are in the jet region while the weaker ones on the flanks have the expected westward displacement relative to the largest one. This implies barotropic growth. In this control run, the jet is symmetric, but the potential vorticity perturbations on both flanks are asymmetric due to the beta effect. Using the same definition, the position of the trough is marked in the $x - y$ plane. Take a close look at the position of the trough and find that the trough line is accompanied by relatively high potential vorticity anomalies. The relative vorticity anomalies near the level of the jet have the same pattern as the potential vorticity, as shown in Fig. 4(b). This indicates the importance of the relative vorticity contribution to the perturbation potential vorticity at the jet level, since the vertical gradient of perturbation potential temperature at this level is small. This also implies the relative importance of the barotropic process at this stage. The temperature

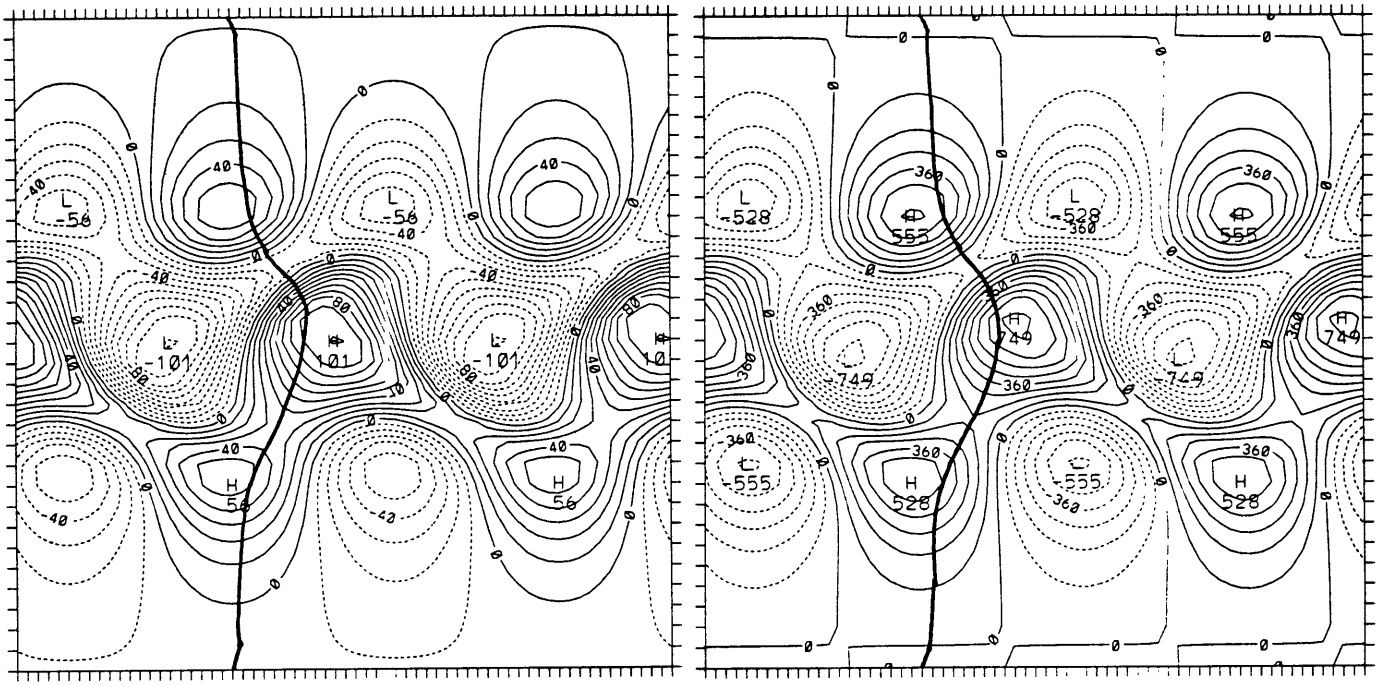

(a) (b)

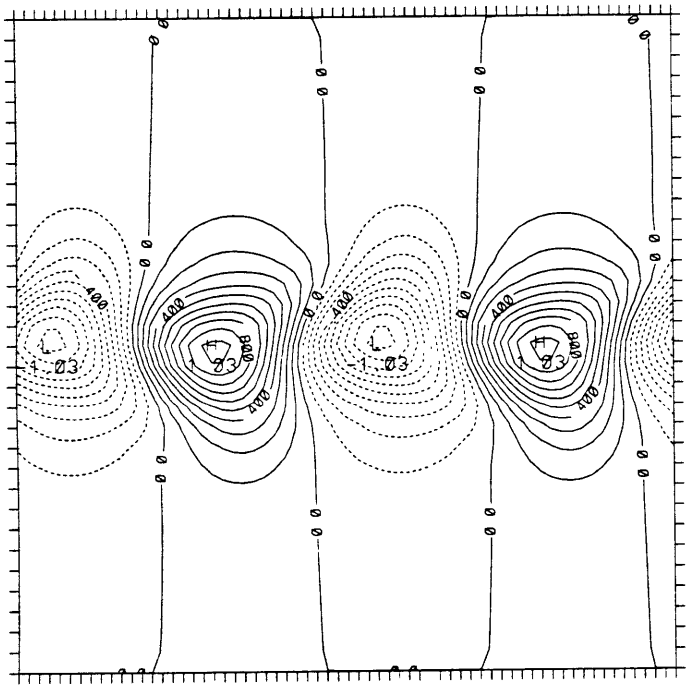

(c)

Fig. 4: The x-y profile the African Easterly waves at day 7. (a) Perturbation potential vorticity (*10^-7 s^-2). (b) Relative vorticity (*10^-8 s^-2). (c) Perturbation potential temperature (K).The domain is 3200 km in y direction and 6400km in x direction.

perturbations at the surface, shown in Fig. 4(c), have a simple sinusoidal variation centered at about $15°N$. The pattern shifts westwards relative to the potential vorticity pattern in the jet. The relative vorticity perturbations at low levels are also consistent with this pattern, with cold temperature anomalies accompanied by negative vorticity anomalies and vice versa (not shown here). The temperature trough, shown in Fig. 4(c), lags the streamline trough line about 1/4 wavelength at the jet zone but almost out of phase at the northward and southward flanks. This lagging phase leads to a negative correlation of $\overline{v'\theta'}$ at the jet meridian and trivial correlation elsewhere. This heat flux, as addressed previously, implies a down-gradient transport. Thus, we come to the conclusion that the eddies grow at the expense of zonal mean APE and KE through both barotropic and baroclinic processes. The strength of the jet weakens during the growing stage of the disturbances. Some further calculations related to energetics will be discussed below.

3.3 Energetics

The conversion of available potential energy from the zonal mean to eddy C_A, as shown in Fig. 2(e), is positive during the linear stage. The patterns broaden in the meridional direction with time and are mainly below the jet level. The eddy available potential energy A_E, as shown in Fig. 5(a), has a pattern similar to C_A with some smaller value located above the jet level. The conversion of kinetic energy from zonal mean to eddy C_K, as shown in Fig. 2(h), is positive. The maximum is located at the surface in the beginning since the circulations induced by the temperature perturbation decay with height (not shown here). The value increases with time and the altitude of the maximum also increases with time up to the jet level. Fig. 5(b) shows the pattern of kinetic energy. The zero curve extends vertically and horizontally with time and reaches over $z = 6.5km$ and covers the whole meridional domain with the maximum located at the jet level.

The figures shown above reveal the linear stage of fast baroclinic and especially barotropic development. The zonal mean wind profile is weakened both vertically and horizontally because the energy is converted into eddy APE and KE (not shown here). Note that the distribution of the wind profile and trough line in both vertical and horizontal planes consistently indicates

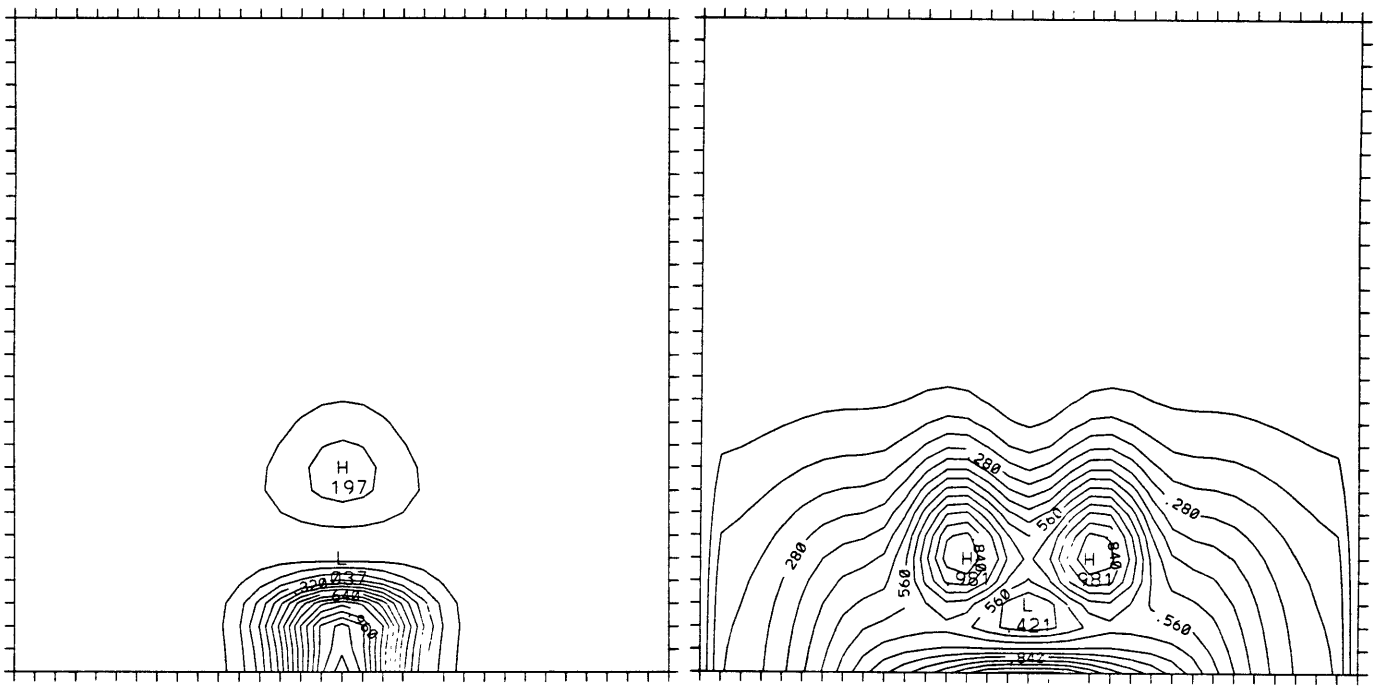

Fig. 5: The x-z profile the African Easterly waves. (a) Eddy available potential energy at day 7. (b) Eddy kinetic energy at day 17. The domain is 15 km high and 6400km wide.

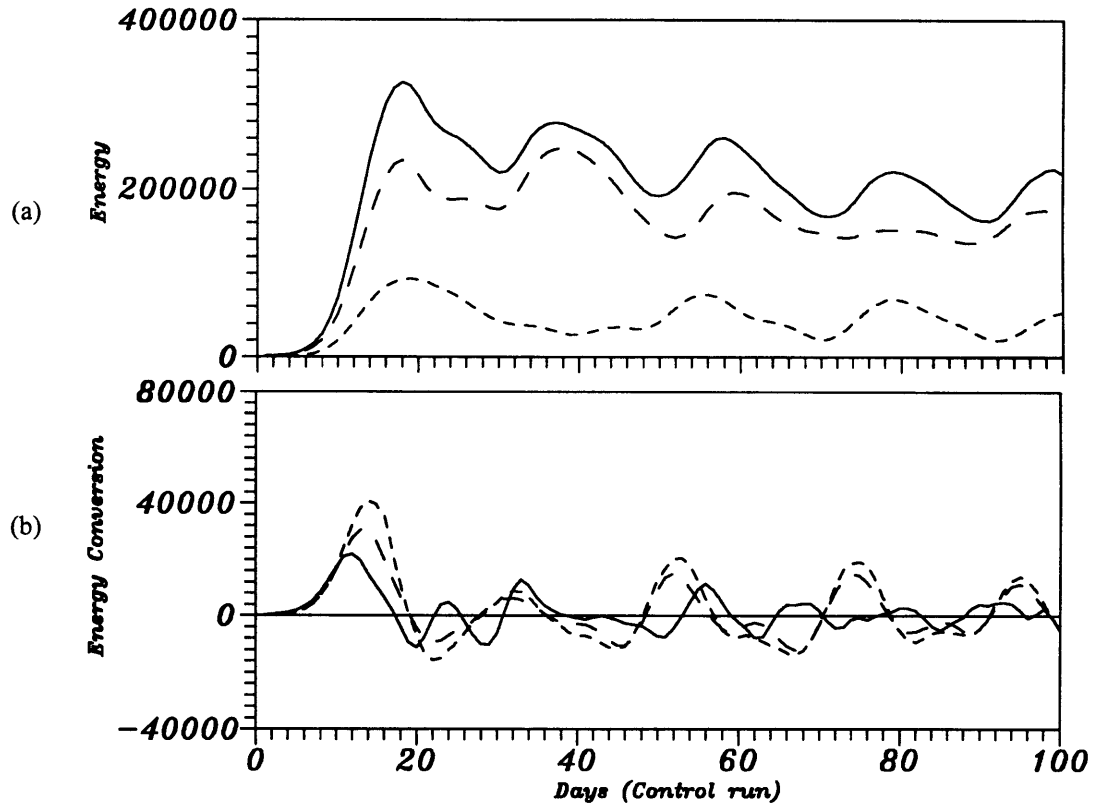

Fig. 6: Time series of the control run. (a) Eddy total energy (solid), eddy kinetic energy (long dash) and eddy potential energy (short dash). (b) CK (solid), CA (long dash) and CE (short dash).

that the waves are in a developing stage.

The time series of eddy kinetic energy (EKE), eddy available potential energy (EAPE), and eddy total energy (ETE) are shown in Fig. 6(a). They peak at day 18. This indicates that the perturbation has gained the most strength from the basic state and reached saturation. After that, EKE, EAPE and ETE decrease and go through a series of oscillatory periods. Note in Fig. 6(a) that the peak value of eddy available potential energy is only about one quarter of the peak value of eddy kinetic energy most of the time. The pattern oscillates with time and stays at an equilibrium level. The picture is a exhibition of nonlinear wave-mean flow interaction. Fig. 6(b) shows the time series of various energy conversion terms. The barotropic conversion term C_K is positive during the developing period and then has similar oscillatory behavior after the system reaches saturation. For the first 10 days the barotropic conversion process C_K is more important than the baroclinic conversion processes $C_A + C_E$. Later on, the perturbation grows mainly through the baroclinic conversion process C_E. Comparing Fig. 6(a) with Fig. 6(b), we find that the energy decay of the perturbation is closely linked to both C_A and C_E. The energy conversions associated with the nonlinear stage described here have much in common with those found in the GATE study over west Africa, and with GCM integrations.

3.4 EP Flux and Nonlinear Evolution

Fig. 7(a) shows the EP fluxes at day 7. There is divergent pattern in the jet region and convergent patterns at the flanks. This implies the deceleration of the mean flow and increase of eddy wave-activity density. EP fluxes are especially useful to see how the eddy grows at the expense of the jet and also how dynamical instability is removed.

Since this is a nonlinear quasi-geostrophic model, the disturbances in this model go through a nonlinear life cycle. As the waves grow approximately linearly up to day 7, the total pseudo-potential vorticity evolution at $z = 3.5km$ is shown from day 7 to day 13 in Fig. 7 at two-day intervals. We can identify the anomalies from the full fields by comparing these figures with the perturbation fields. The pattern is basically zonal uniform during the linear stage. As the waves grow further, asymmetric isolated contours form around the positive potential vorticity anomaly on the jet. By day 11, two isolated contours start pinching together. The

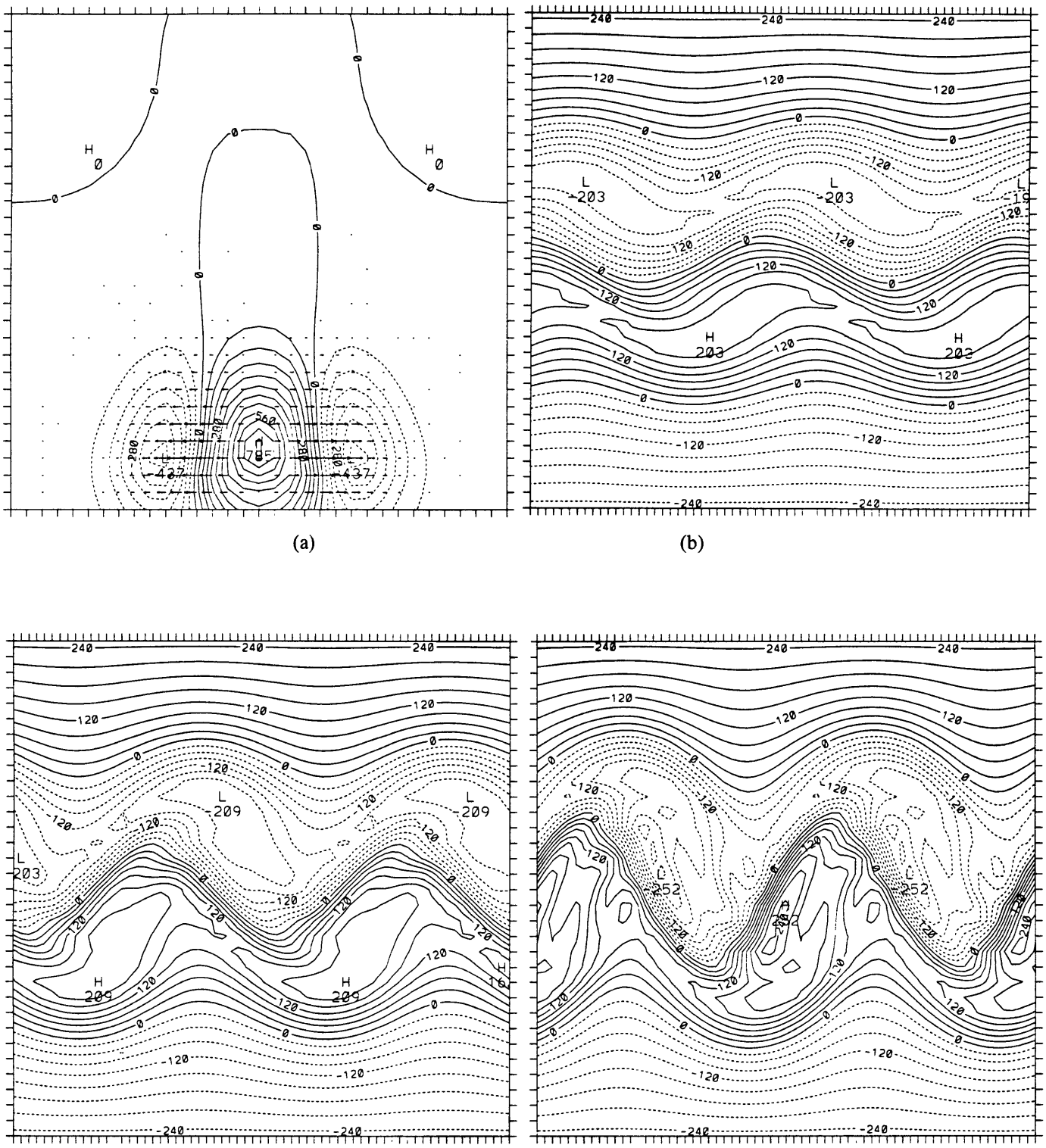

Fig. 7: (a) The x-z profile of EP flux and its divergence at day 7. (b) x-y profile of PV at day 7. (c) x-y profile of PV at day 9. (d) x-y profile of PV at day 11.

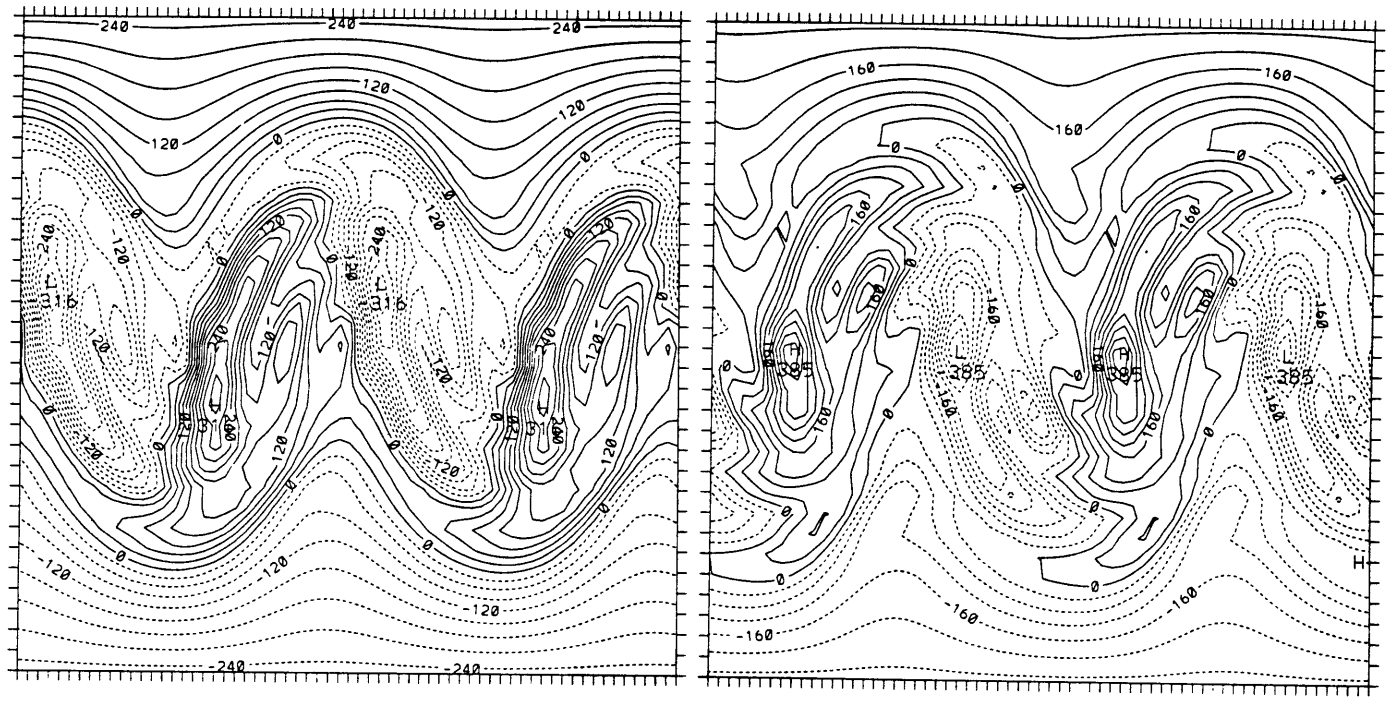

(e) (f)

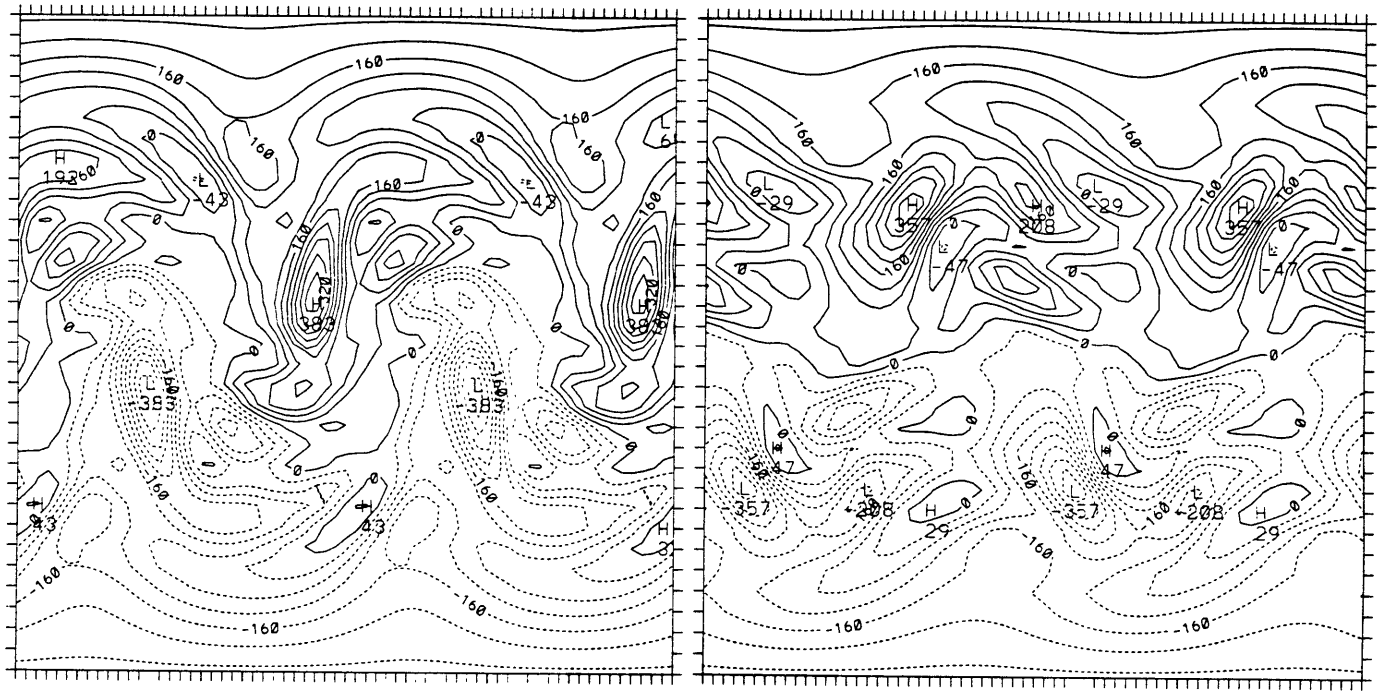

(g) (h)

Fig. 7: Continue. (e). x-y profile of PV at day 13. (f) x-y profile of PV at day 15. (g) x-y profile of PV at day 17. (h) x-y profile of PV at day 19.

behavior afterwards is clearly an indication of dissipation and marks saturation of the instability. Similar behavior was also seen by Malardel et al. (1993) and Schär and Davies (1990). After day 15, the main positive/negative potential vorticity anomalies that form in the jet region move poleward/equatorward away from the jet region. Positive and negative anomalies move anticyclonically around each other and then move equatorward and poleward respectively. Note that the anomalies dissipate as they move. By day 17 the positive centre has moved poleward of $20°N$. Throughout the life cycle, the potential vorticity pattern is more disturbed in the jet zone than on the flanks. The meridional scale of the anomalies associated with the jet is much larger during nonlinear stage than during linear stage.

The structure at day 17 is shown here because by then the wave shows significant nonlinear structure and also the magnitude of the meridional wind has comparable magnitude to that observed off the west coast of Africa, as shown in Fig. 2(b). The perturbation potential vorticity has stronger anomalies at the jet level. At high levels, perturbation potential vorticity contours exhibit a wavelike distortion. West of the positive potential vorticity anomaly at the jet level, high potential vorticity has descended, whereas above it low potential vorticity has also descended as shown in Fig. 8(a). These potential vorticity anomalies induce a high level circulation and is seen in Fig. 2(b). As pointed out previously, the meridional wind looks more similar to observations during the nonlinear stage. The amplification of the meridional wind at upper level is associated with upward propagation of Rossby waves and takes place mainly after the system reaches saturation.. The strongest meridional winds are at the surface at day 17. The magnitude of the meridional wind at the surface is about $12m/s$, whereas at the jet level it is about 2.3 m/s. Note, in Fig. 8(b) and (c), that the surface winds are associated more with the surface temperature anomalies than with the lower level vorticity anomalies. During the nonlinear stage, the surface temperature anomalies become stronger relative to the vorticity anomalies at jet level, which dominate during the linear stage. The vertical velocity, Fig. 8(d), still has checkerboard pattern but the value is larger and comparable to that of observations.

The evolutions of EP flux from day 9 to day 19 are shown in Fig. 9. As pointed out previously, during the linear stage the vectors point horizontally and indicate that barotropic processes are more important than baroclinic processes. By day 13, the system enters the nonlinear stage and the divergence pattern expands horizontally while the vectors become

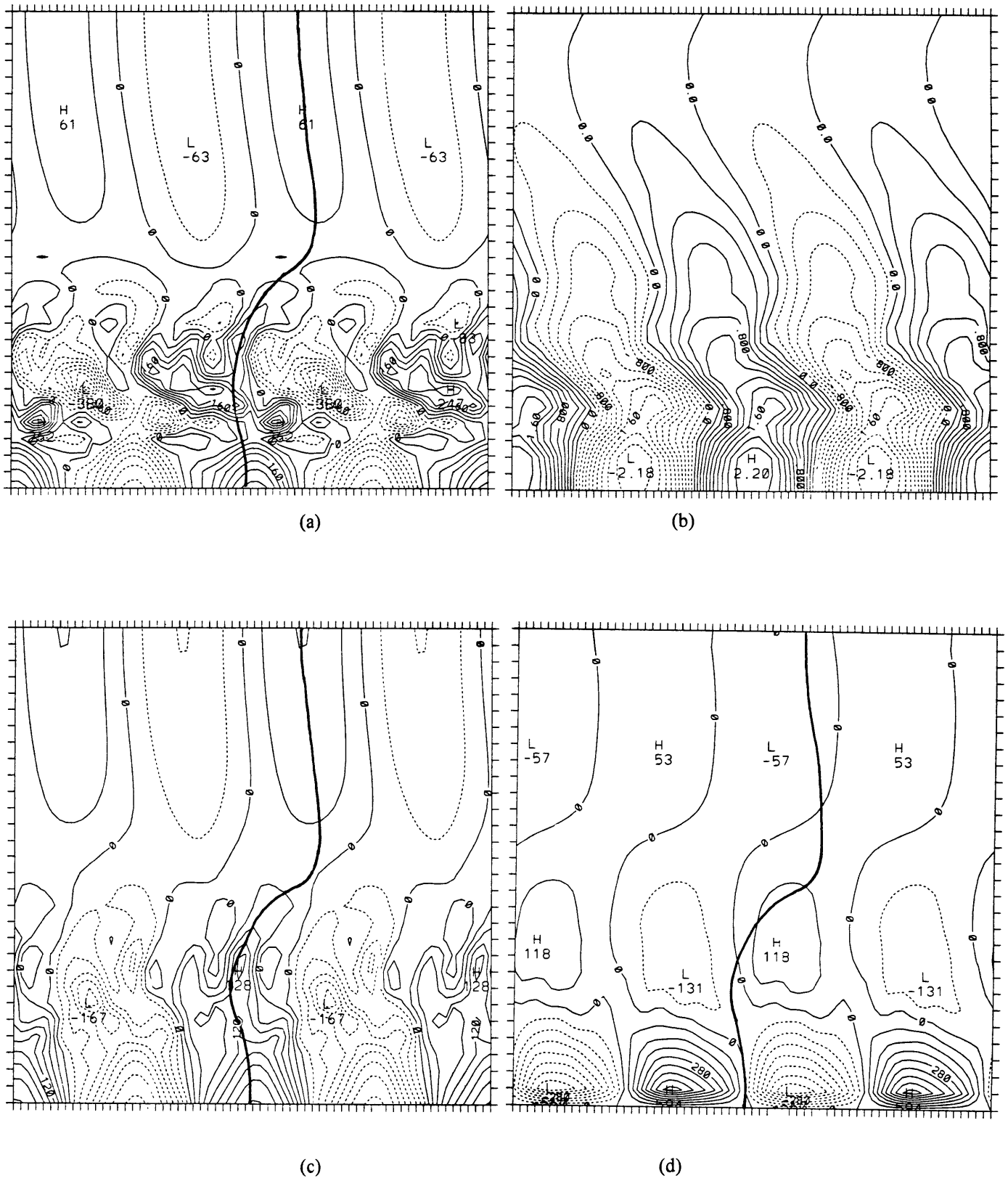

Fig. 8: The x-z profile the African Easterly waves at day 17. (a) Perturbation PV. (b) Perturbation potential temperature. (c) Relative vorticity. (d)Vertical velocity. The domain is 15 km high and 6400km wide.

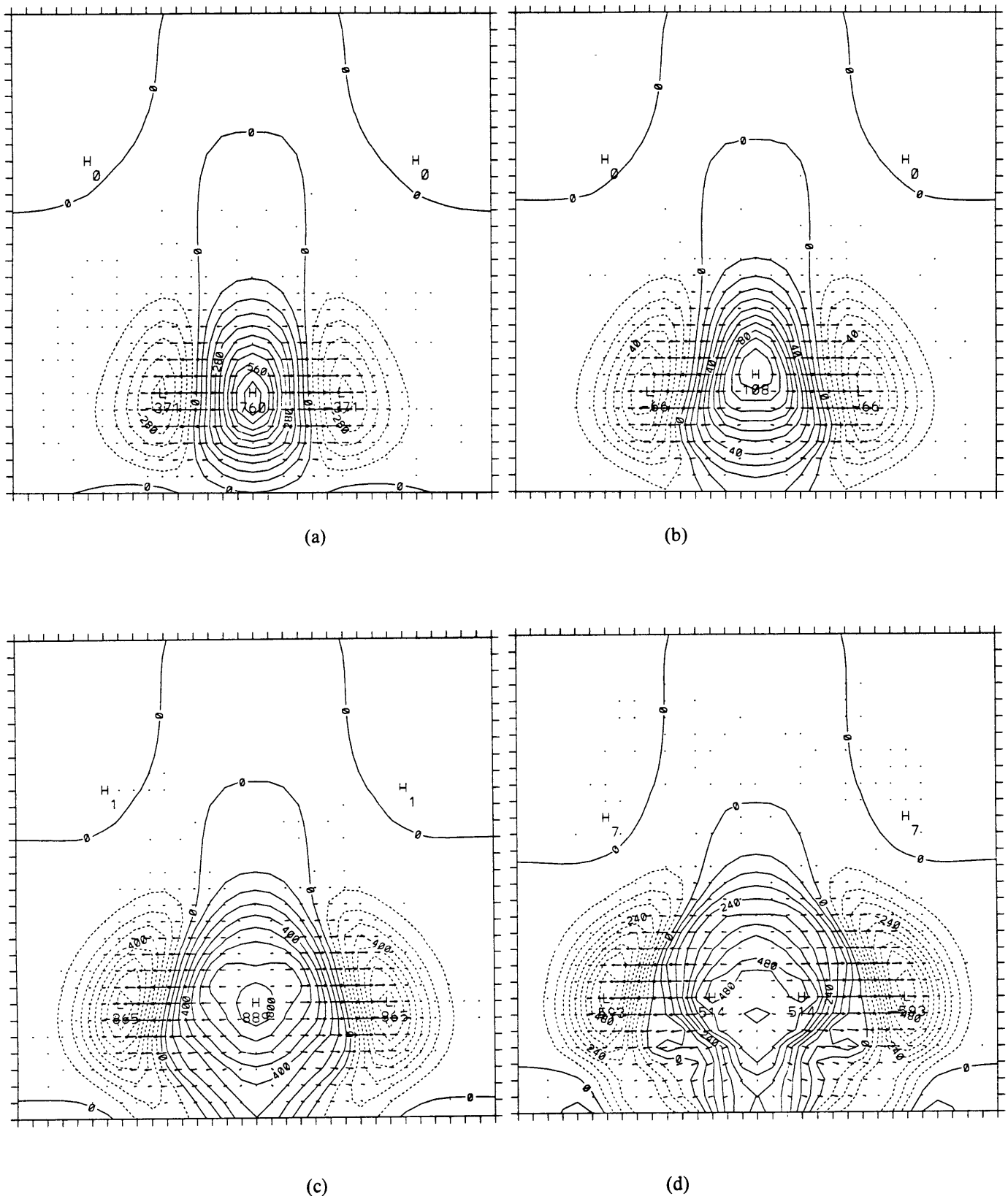

Fig. 9: EP flux and its divergence. (a). Day 9. (b) Day 11. (c) Day 13. (d) Day 15.

gradually more vertical. The divergence values decrease as the strength of the jet weakens. By day 17, low level convergence has formed due to the downward propagating of Rossby waves. Rossby waves also propagate upward and can be identified by the outline of the vectors. Upward propagating Rossby waves is linked to the appearance of upper level circulation which is not seen during the linear stage.

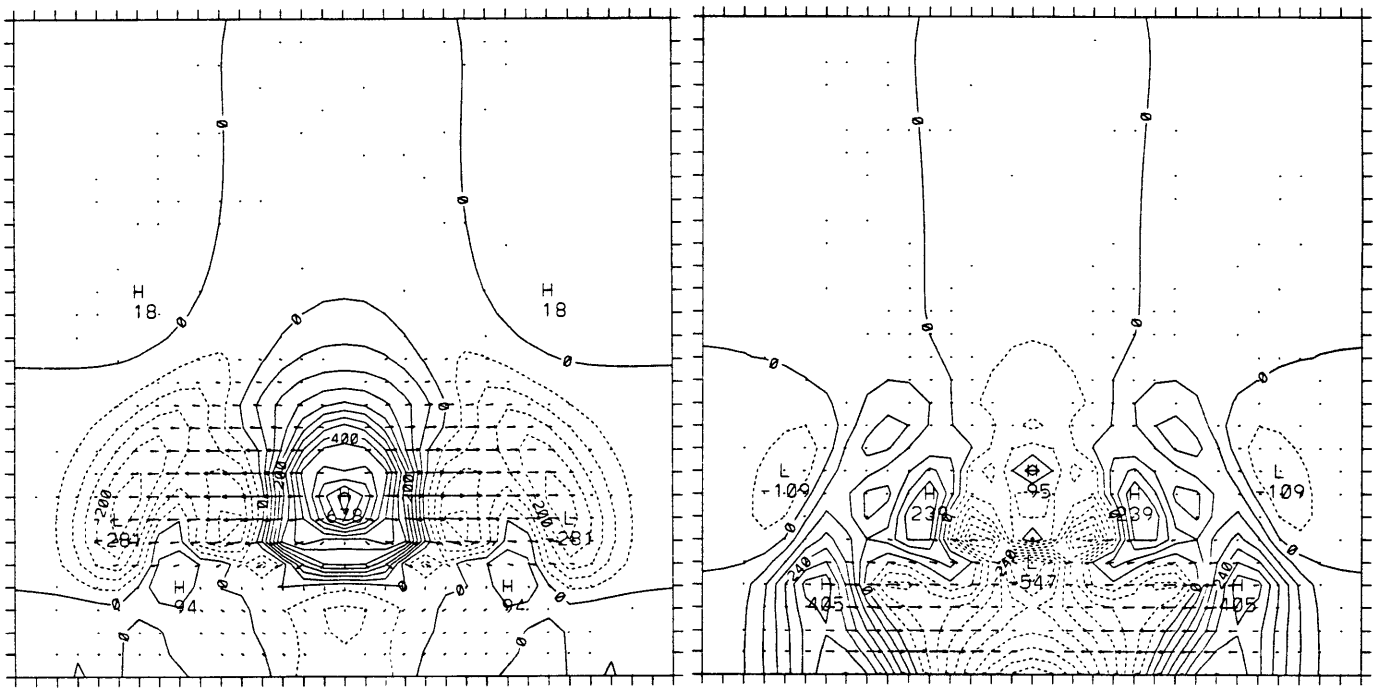

Fig. 9: Continue. (e). Day 17. (f) Day 19.

Chapter 4

Statistic Equilibrium Dynamics

The structure and energetics described above consistently point out the importance of nonlinearity and vertically propagating Rossby waves. They contribute to the upper level circulation and result in a energy cycle different from that of the linear stage. However, our goal is not to perform a case simulation. The atmosphere is continually forced by diabatic processes and destabilized to convection. We are interested in the final state the system will reach after a long run. In this section, different diabatic processes will be incorporated into this model. The results are discussed separately after each subsection.

4.1 Ekman Damping: Bulk Aerodynamic Method

The most important characteristic of the planetary boundary layer is that the horizontal wind has a component directed toward lower pressure due to the presence of friction. This implies mass convergence in a cyclonic circulation and mass divergence in an anti-cyclonic circulation, which in turn by mass continuity requires vertical motion out of and into the boundary layer, respectively. Observations indicate that surface momentum fluxes can be represented by a bulk aerodynamic formulae as

$$\tau_x = \overline{(u'w')}_s = -C_D u(u^2 + v^2)^{1/2},$$

and

$$\tau_y = \overline{(v'w')}_s = -C_D v(u^2 + v^2)^{1/2},$$

where C_D is a nondimensional drag coefficient with a value of 2.0×10^{-3}, the subscript s denotes surface. They appear in the vorticity equation as $-\widehat{k}\cdot(\overrightarrow{\nabla}\times\frac{\partial\overrightarrow{\tau}}{\partial z})$. The effect of surface momentum fluxes works to reduce the absolute value of relative vorticity. This simple parameterization is verified by the results of Reeves et al. (1979), see Fig. 10, that the individual values of surface residual and surface vorticity are almost always opposite in sign. In this way the effect of boundary layer momentum fluxes is communicated to the free atmosphere. The Ekman damping effect is considered in both part I and II.

4.2 Relaxation

As shown in chapter 3, the jet strength, the horizontal and vertical wind shears and the corresponding potential vorticity gradients are considerably weakened during the growing period. The zonal mean flow has also weakened considerably by day 10. One would require the processes resulting in the easterly jet still active during the life cycle just as the radiation continue to maintain the strength of the meridional temperature gradient and the easterly jet. On the other hand, wind stress will induce vertical heat flux and water vapor flux from the ocean surface. Convection will redistribute the excess latent heat and sensible heat upward. In that case, relaxation works reduce the temperature contrast. Without explicitly modelling these processes, mainly radiative processes in this case, it is possible to parameterize them by linearly relaxing the zonal mean potential temperature and potential vorticity back to its initial state. The life cycle presented here has a relaxation time-scale of 5 days. This time-scale is chosen since it is the typical observed period for easterly waves. The formulas for restoration of the zonal mean potential vorticity and boundary potential temperature are

$$\overline{q}^t = \overline{q}^t - \frac{1}{\tau}(\overline{q}^t - \overline{q}^i), \tag{4.1}$$

and

$$\overline{\theta}_b^t = \overline{\theta}_b^t - \frac{1}{\tau}(\overline{\theta}_b^t - \overline{\theta}_b^i) \tag{4.2}$$

where $\overline{q}^t$,$\overline{\theta}_b^t$ and $\overline{\theta}_t^t$are zonal mean potential vorticity and lower boundary potential temperature at time t; index i denotes the initial state.

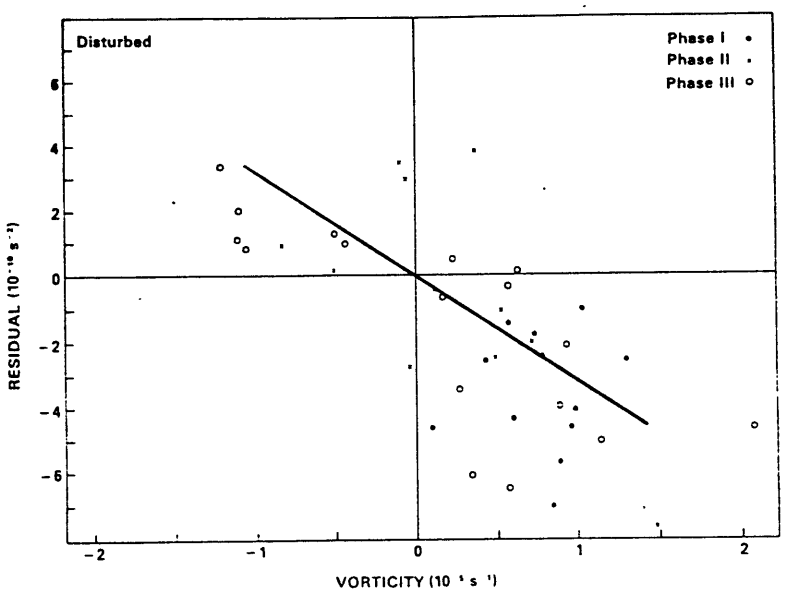

Fig. 10 The relationship between vorticity and residual term for disturbed conditions. (From Reeves et al. 1979)

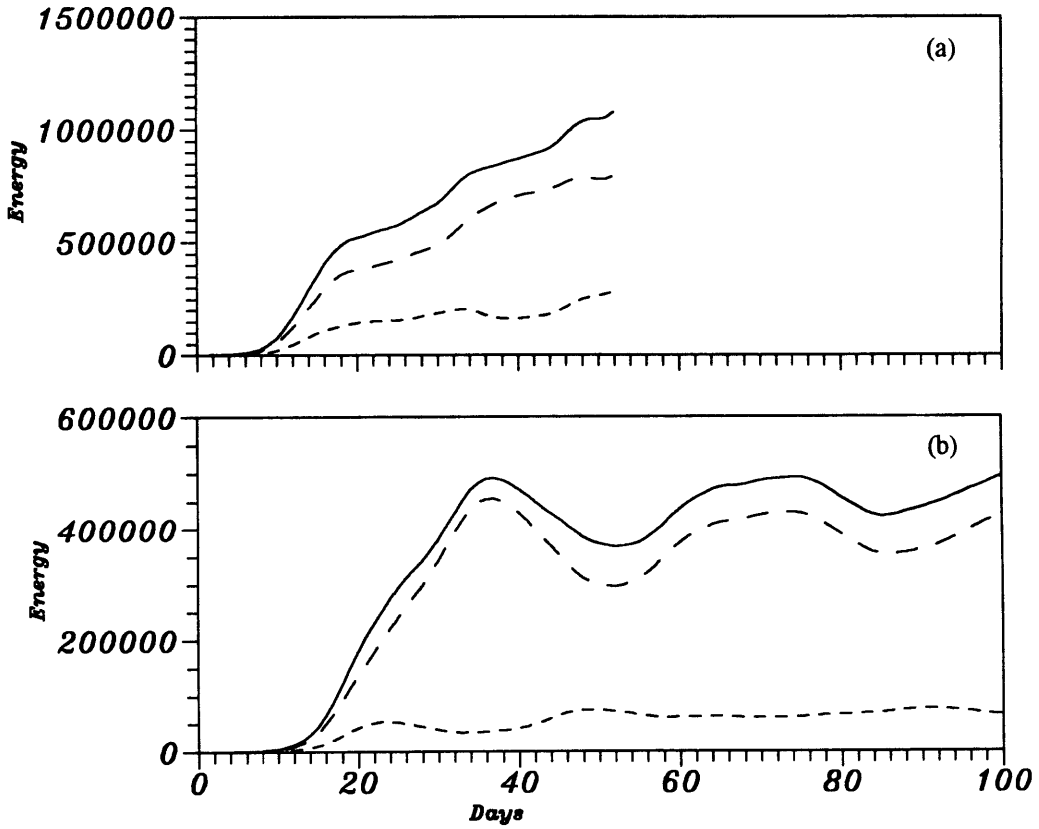

Fig. 11: Time series of (a) Eddy total energy (solid), eddy kinetic energy (long dash) and eddy potential energy (short dash) with relaxation. (b) Same as (a) but with Ekman damping and relaxation.

The evolution of ETOT, EKE and EAPE are shown in Fig. 11(a). Up to about day 16, the energy grows at almost the same rate as in the control run. However, it continues to grow and reaches a maximum at day 21 for $\tau = 10$ days. There is no indication of decay of the energy.

4.3 Statistic Equilibrium Dynamics

As discussed in previous sections that Ekman damping tends to dissipate the eddy energy from below and results in smaller energy conversions. On the other hand, relaxation restores the zonal mean back to the initial condition on the time scale of 5 days. It is interesting and instructive to see what would happen if these two physical processes are both considered. The result is presented in Fig. 11(b). After integrating over 100 days of model time, it is apparent that the system has reached a state of dynamic equilibrium. Total eddy energy, EKE and EAPE all reach and stay at the equilibrium level. It is not surprising if we recall that the typical time scale of Ekman damping is about 5 days and the time scale is selected for relaxation.

Part II

Inclusion of Diabatic Processes

Chapter 5

Physical Processes

5.1 Radiative Cooling

The troposphere and stratosphere in the tropical region have an average radiative cooling rate of nearly constant with value of 1.2°C/day and 0.2°C/day respectively as shown in Fig. 12 (from Thompson et al. 1979). Constant values of 1.8°C/day and 0.2°C/day are used as the radiative cooling rate for the troposphere and stratosphere respectively. Radiative cooling effects are considered in part II only.

5.2 WISHE Process: Water Vapor and Sensible Heat Fluxes

Consider the lower boundary with a fixed temperature distribution which has a positive temperature gradient in the y direction. The southern half of the domain, which is occupied by the ocean has a constant sea surface temperature with saturated value of specific humidity. Since the saturated value of water vapor pressure is a function of temperature only, the saturated value of specific humidity over the ocean is also fixed. The land over the northern half of the domain has a water vapor flux that decreases hyperbolically from the coast line. The distribution of fixed surface temperature is shown in Fig. 13a. Thus, the wind-induced surface sensible heat flux and water vapor flux can be expressed, using the bulk aerodynamic formulae, as

$$F_z^\theta = C_E U(\theta_s - \theta_{1/2})$$

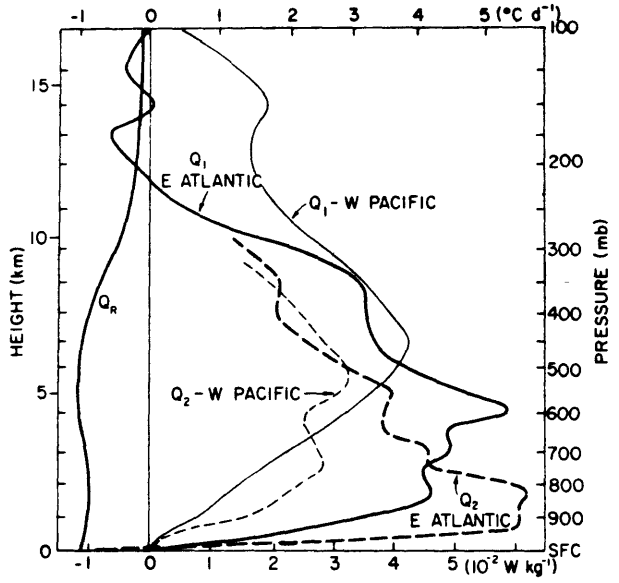

Fig. 12 Variation with height of the apparent sensible heat source Q_1 and apparent latent heat sink Q_2 for the B-scale area and KEP triangle. Also shown is the profile of mean radiational heating Q_R for the B-scale area.
(From Thompson et al. 1979)

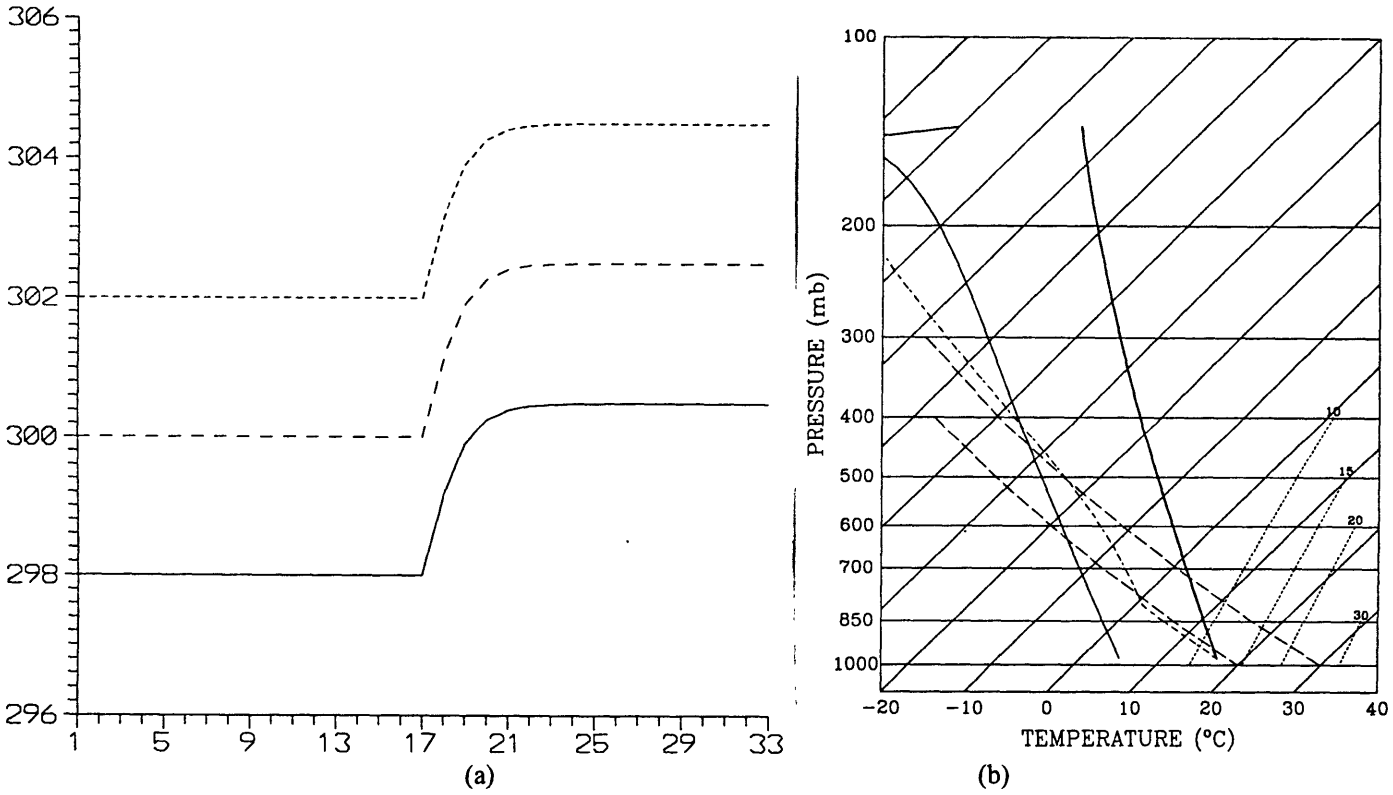

Fig. 13 (a) The meridional distribution of surface temperature, (b) initial sounding.

and

$$F_z^q = C_E U(q_s - q_{1/2})$$

where the nondimensional coefficient C_E is identical to C_D used in Ekman damping, with a value of 2.0×10^{-3}, and U is the constant wind speed of 5 m/sec. In African wave experiments, the total boundary wind $\sqrt{(\overline{u^2+v^2})}$ is used to replace U. Assume that the atmosphere has the initial sounding as shown in Fig. 13b. Through the wind-induced vertical fluxes of heat and water vapor, the atmosphere is moistened and heated from below through the Wind induced sensible heat flux (WISHE) process. The equilibrium-sounding profile is expected to be substantially different from the initial sounding. Note that WISHE processes are considered in part II only.

Chapter 6

Experimental Design

6.1 Zonally Symmetric Experiment: the Response of a Moist Atmosphere to Prescribed Contrasting Boundary Properties

In this experiment, we first conduct a zonally symmetric simulation in a moist atmosphere. There is no motion in the initial state and no perturbations will be introduced in this zonally symmetric experiment. This experiment is inspired by the obvious fact that the African easterly jet is the result of thermal wind balance as subject to contrasting surface temperature as that of North Africa.

The land-ocean contrasts in this experiment are manifest in varying surface temperature and surface water vapor and sensible heat fluxes. The surface temperature and nondimensional drag coefficient C_d for the surface fluxes calculation are prescribed as fixed external factors and are not allowed to change by any possible feedback from the atmosphere. The initial background relative humidity is set to be rather dry, as shown in Fig. 15, which has a relative humidity gradient in y and z directions with higher values over the ocean. Different background relative humidity will be examined to test the sensitivity of the equilibrium state to the background relative humidity in section 7.4. The ocean surface temperature has a constant value but surface temperature over land increases hyperbolically northward to capture the unique geographical distribution of surface temperature over West Africa, see Fig. 13a. The sensitivity to differ-

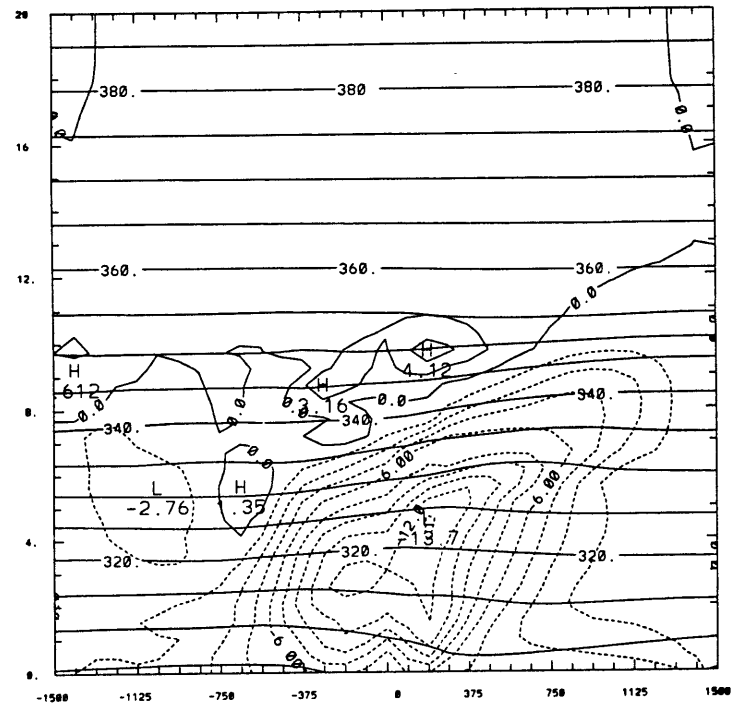

(a)

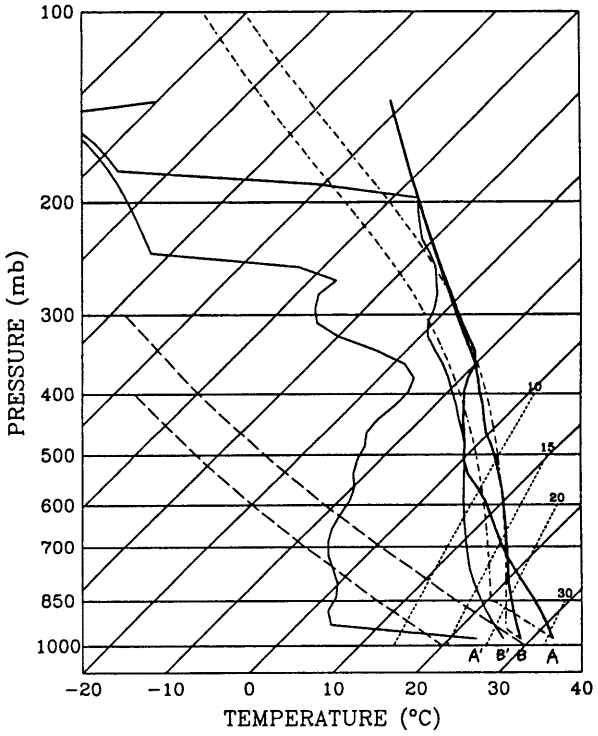

(b)

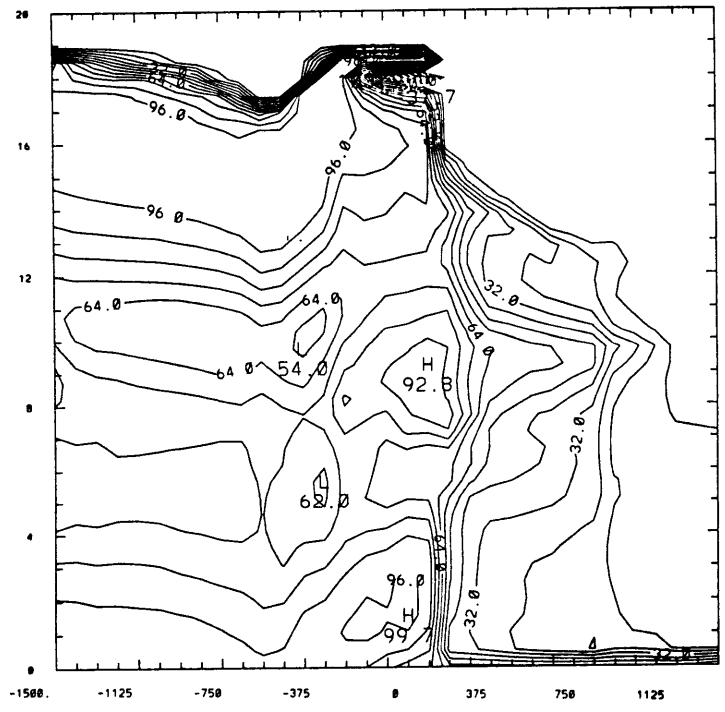

(c)

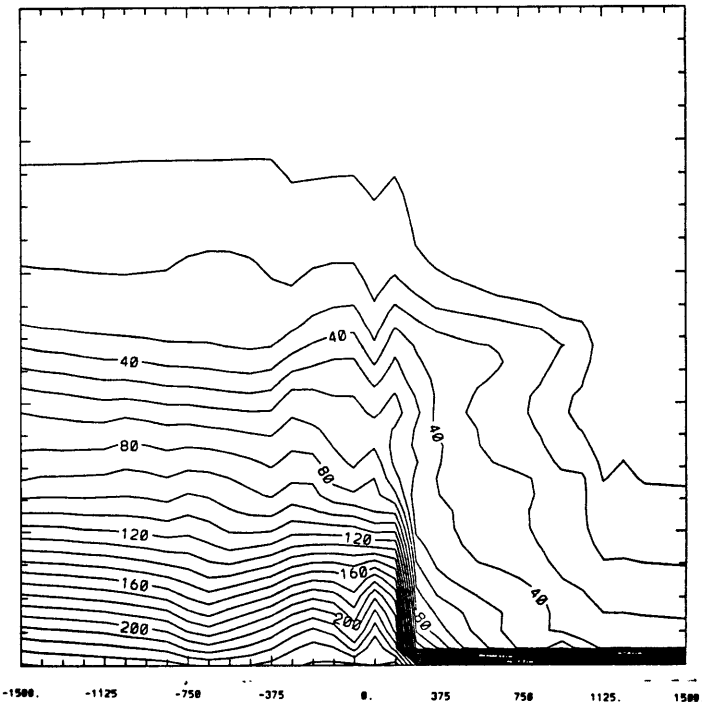

(d)

Fig. 14 Fields at equilibrium state (a) y-z profile of mean zonal wind, contour interval of 2 m/sec. (b) sounding profiles, A and A' represent T and Td over land; B and B' for T and Td over the ocean. (c) y-z profile of relative humidity (d) y-z profile of specific humidity, label scaled by 10000.

ent SSTs and temperature gradients will also be explored in section 7.2. The initial vertical temperature profile for the experiments is plotted in Fig. 13b. The integration begins with a prescribed tropospheric radiative cooling rate of 1.8°C/day and surface heat fluxes from the lower boundary. The surface fluxes are calculated by simple bulk aerodynamic formulae as described in chapter 2. Radiative cooling, sensible heat and water vapor fluxes at the lower boundary are the ultimate large-scale forcing. Note that the convection Scheme used here is that of Emanuel (1991), optimized using TOGA COARE data as described in Emanuel et al. (1998). With the combination of these physical precesses, it is instructive to exploit and analyze the system when the model atmosphere has reached a state of quasi-equilibrium..

The system is run long enough to be sure of reaching an equilibrium state. Fig. 15 shows the time series diagrams of the relative humidity. They are chosen to represent the moist ocean regime, see Fig. 16a, and the dry land regime, see Fig. 16b. Note that the relative humidity fields approach an equilibrium state after about 70 days. Due to the efficient input of water vapor from the ocean surface, the relative humidity is everywhere above 55% in Fig. 16a. Water vapor is transported and redistributed vertically. Over the land, the relative humidity field shows a substantial dearth of water vapor. Time series of precipitation rate for 5 locations over the ocean are plotted in Fig. 17. It is obvious that the system takes about 80 days to reach an equilibrium state.

As shown in Fig. 14a, an African easterly jet-like wind profile forms which has the same order of magnitude as the observed jet. The easterly maximum is located at 4.1 km height with a value of -13.7m/sec. There are westerlies above the easterlies due to temperature gradient reversal above the jet. The soundings in the equilibrium state over the land and ocean are plotted together in Fig. 14b. Note in Fig. 14b that the temperature profile is very close to moist adiabatic over the ocean (marked B). Convection does consume the instability accumulated by the large scale destabilization as indicated by the temperature profile. Basically, the equilibrium state is nearly convectively neutral in a average sense over the ocean without any substantial change with time in the sounding profile. Comparatively, the sounding over the land (markA) has a lapse rate which falls in between dry and moist adiabatics. Cross-sections of relative humidity and specific humidity in y-z plane are shown in Fig. 14c. Generally speaking, the relative humidity over the ocean has a maximum near the ocean surface. The relative humidity

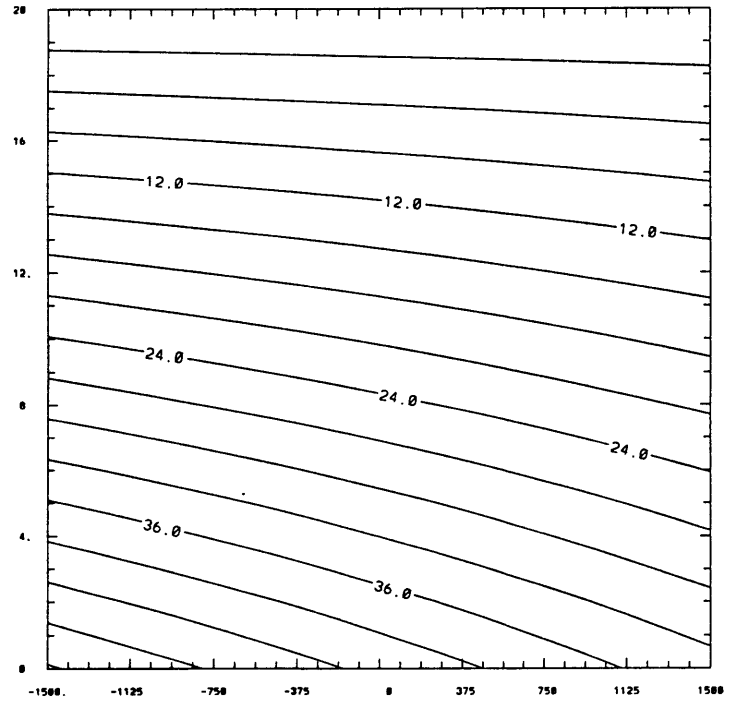

Fig. 15 y-z profile of background relative humidity

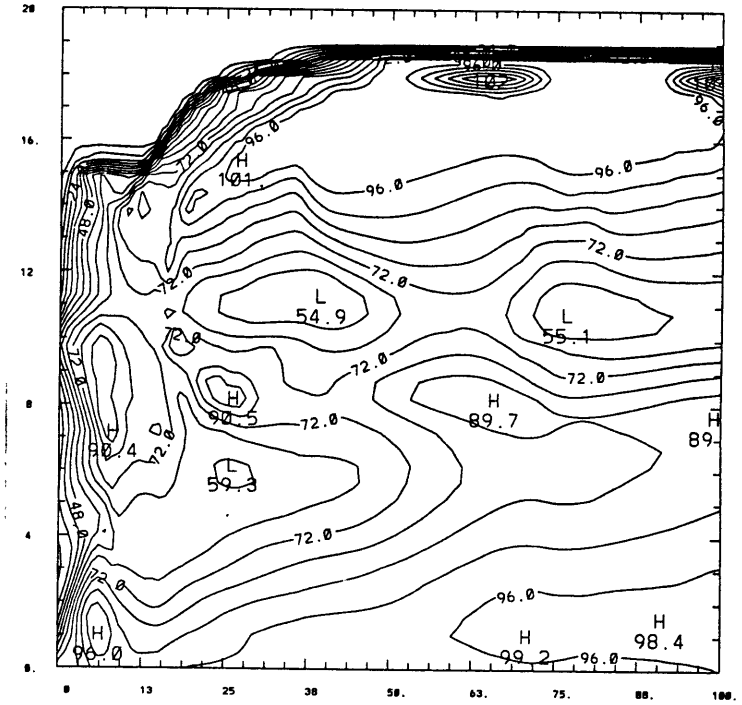

(a)

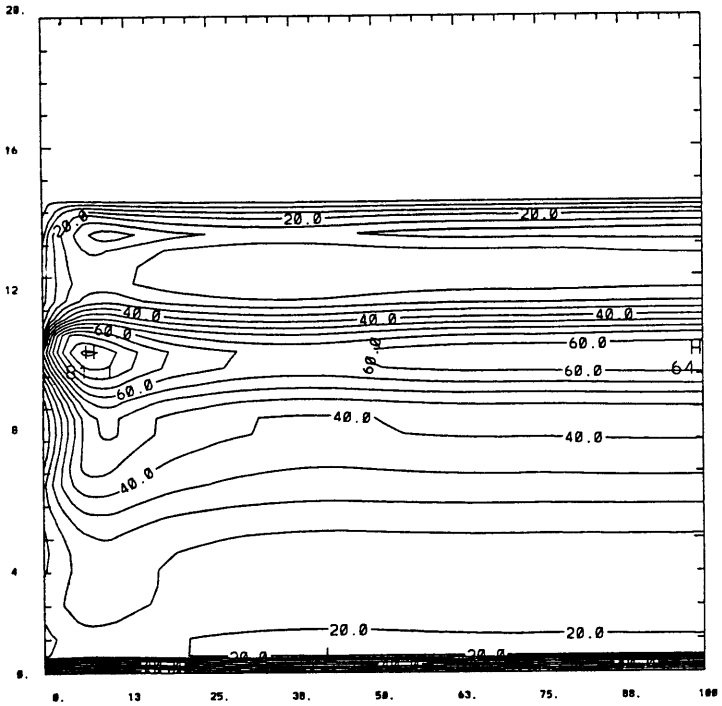

(b)

Fig. 16 Time series of vertical profile (a) over the ocean, (b) over the land.

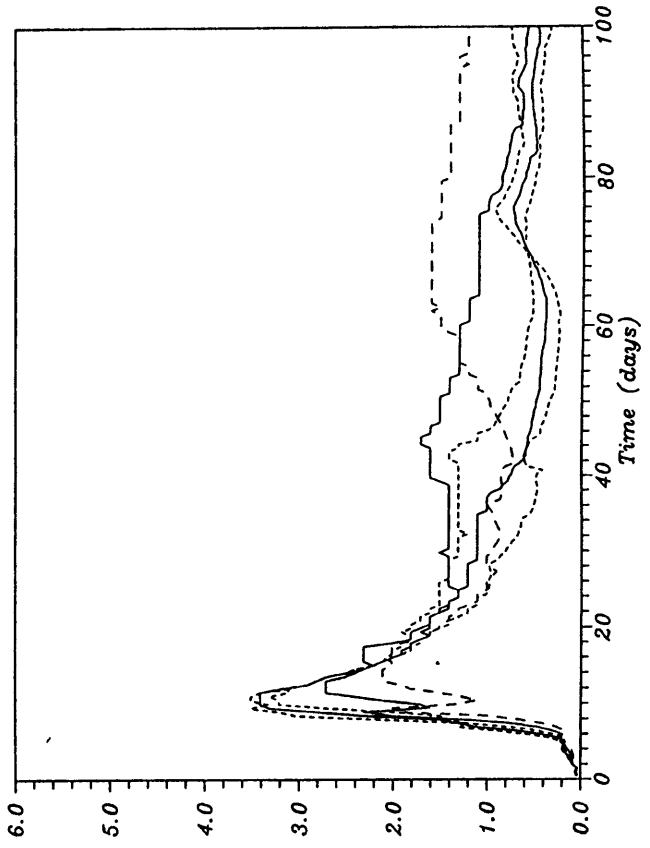

Fig . 17 Time series of precipitation rate over the ocean. 5 different cations are shown here.

decreases upward, has a minimum near 10km and then increases upward to 16km. From there, it decreases rapidly upward. The relative humidity shows relatively lower values throughout the atmosphere over the land. Specific humidity, in Fig. 14d, shows a strong gradient between land and ocean.

Over the land the sensible heat flux is larger. Qualitatively speaking, since the water vapor flux is smaller over the land, the adjustment there is closer to dry adiabatic adjustment than to moist adiabatic adjustment. Over the ocean, much more water vapor is pumped up into the free atmosphere. The sensible heat flux, though smaller compared to that over land is also input from the lower ocean surface. Thus the adjustment is much closer to moist adiabatic one. We can anticipate a larger vertical lapse rate over the land than over the ocean. Some sensitivity experiments are examined to see the effects of surface flux calculations over the land in section 7.4.

Note that the temperature is higher over the land below 3.5 km and lower above as seen in Fig. 14b. The vertical wind shear may be examined in terms of the thermal wind relationship:

$$\frac{\partial \overline{u}}{\partial z} = -\frac{g}{fT}\frac{\partial \overline{T}}{\partial y}.$$

Since the zonal mean temperature is a function of y and z, the strength of the jet is determined by both the surface temperature gradient and the horizontal distribution of vertical temperature lapse rate according to the thermal wind balance. Since the temperature lapse rate is larger over the land than over the ocean due to the differential in latent heat release, the height of the temperature contrast reversal is determined by the contrast of the surface water vapor flux and thus the differential latent heat release. The reversal of temperature contrast between land and ocean changes the sign of vertical wind shear and thus results in a jet structure, as shown in Fig. 14a.

6.2 Stability of the Equilibrium State

To determine if the equilibrium state obtained satisfies the Charney-Stern necessary condition for instability, the potential vorticity gradient of the equilibrium state is plotted in Fig. 18. Since $(\partial\theta/\partial y)_{lower}$ is positive as prescribed, $(\partial\theta/\partial y)_{upper}$ is zero, and $(\partial\theta/\partial y)_{interior}$ has -,+,-,

+ pattern over the lower central part of the domain, the flow satisfies the necessary condition for instability. A different pattern is located above 6 km, accompanying the westerly maximum. The zero gradient is marked by a heavy solid curve. Thus the equilibrium state established in zonally symmetric experiment satisfies the Charney and Stern criteria for instability in that the gradient of potential vorticity changes sign in the interior. This equilibrium state will be used as the basic state to perform African wave experiments as described in the next chapter.

Chapter 7

Sensitivity Experiments

7.1 Different SSTs

In this section, different SSTs, as plotted in Fig. 13a, are used to test the sensitivity of jet properties to different SSTs. Note that the temperature gradient is still kept constant in these experiments. The results are shown in Fig. 19 and summarized in Table 2.

Table 2: The results of sensitivity experiments with different SSTs.

SST	jet height	jet value	vertical shear below the jet
298K	5.0 km	-11.9 m/sec	-1.68 $msec^{-1}km^{-1}$
300K	4.1 km	-13.7 m/sec	-2.64 $msec^{-1}km^{-1}$
302K	1.8 km	-16.0 m/sec	-5.60 $msec^{-1}km^{-1}$

The results show a positive correlation between the strength of the jet core and SST similar to the observational results (Kidson 1977; Newell and Kidson 1984; Landsea and Gray 1992; Druyan and Hall 1994,1996; Fontaine et al. 1995). However, the height of the easterly maximum is negatively correlated with SST. Chen and Ogura (1982) demonstrated that African waves are about 100mb higher during Phase I of GATE than Phase III in late summer. The vertical wind shear below the jet core has larger values with larger SST. The results are consistent with the results reached by Miller and Lindzen (1992). They proposed that rainfall is organized only if the unstable jet with sufficient strength of shear is within a few kilometers of the moist layer. The controlling factors rely mainly on vertical wind shear and the height of the jet.

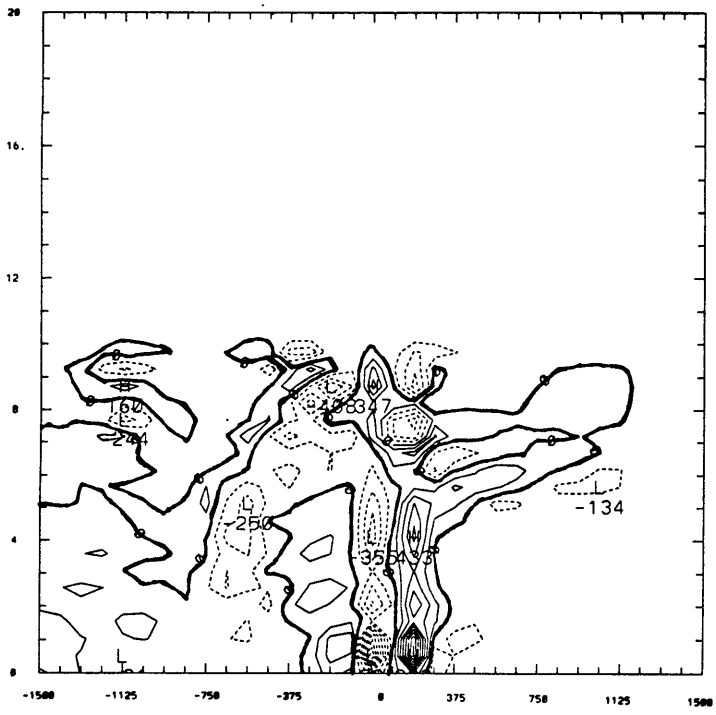

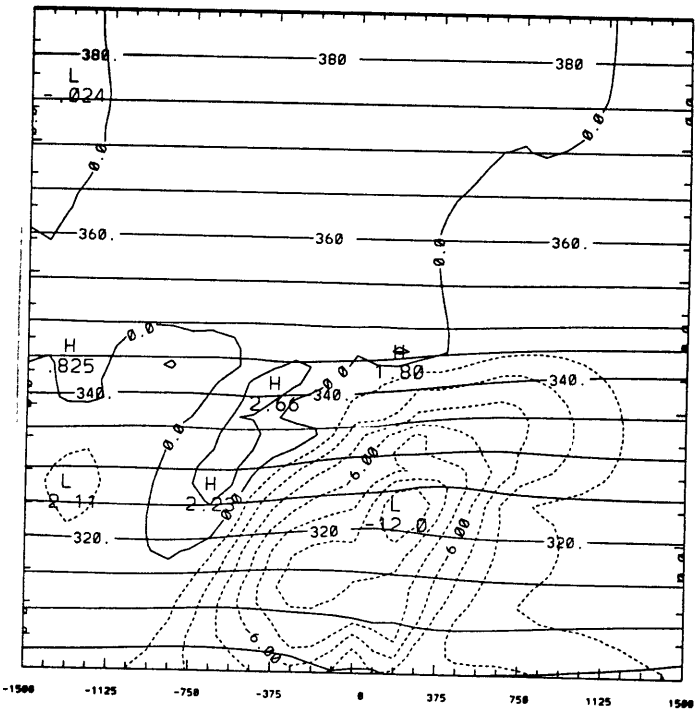

Fig. 18 meridional gradient of zonal mean PV. (a)

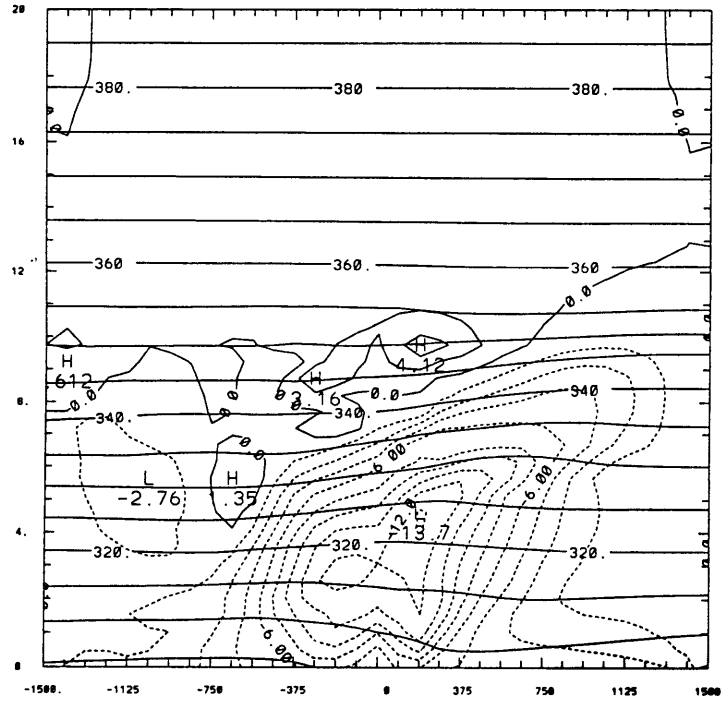

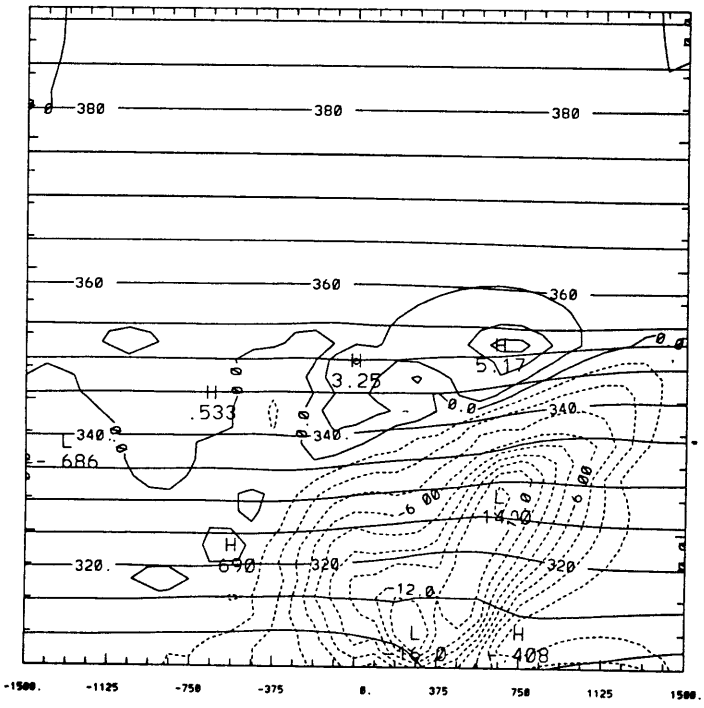

(b) (c)

Fig. 19 The y-z vertical cross-sections for mean zonal wind profile, interval of 2m/sec. (a) sensitivity with lower SST of 298K, (b) control run with SST of 300K, (c) sensitivity with higher SST of 302K.

The absolute magnitude of the jet, however, is somewhat less important. The results of these experiments show that weaker shear and a higher African easterly jet appears with lower SST. The results of Paradise et al. (1995) demonstrated that vertical shear below the African easterly jet is the most sensitive parameter in determining the African waves growth rate, wavelength, induced ascent and low-level convergence, although no direct linkage of these quantities to the height of the jet was addressed. The correlation of the activity and the strength of the African waves with SST will be examined in the next chapter, where perturbations are introduced at the lower boundary.

7.2 Different Temperature Gradients

As discussed in section 6.1, the height and strength of the jet is determined by the surface temperature gradient and the vertical temperature lapse rate. In fact, the surface temperature distribution over North Africa and the Gulf of Guinea is more complicated than we have used here. Presumably, it may lead to some differences between the observations and our numerical experiments. Since it's not our intention to perform case simulations in this paper, a detailed geographic distribution of temperature is thus not a requisite. However, at least we need to capture the basic characteristics of the temperature field that can be used in the zonally symmetric experiment. The daily average surface temperature from Burpee (1972) is shown in Fig. 20. Note that the isotherms are basically zonal, except in the region east of the Gulf of Guinea. Thus a zonally homogeneous temperature field with a hyperbolic gradient could capture the basic properties of the temperature distribution, especially in the region we are interested in. In this section different surface temperature gradients, as shown in Fig. 21, will be used to test the sensitivity.

Fig. 22ab and 14a show the zonal wind cross-sections at equilibrium state for the three different cases of temperature gradients. Higher temperature gradient results in a stronger but lower jet. This is certainly a natural response of thermal wind balance subject to different surface temperature gradients.

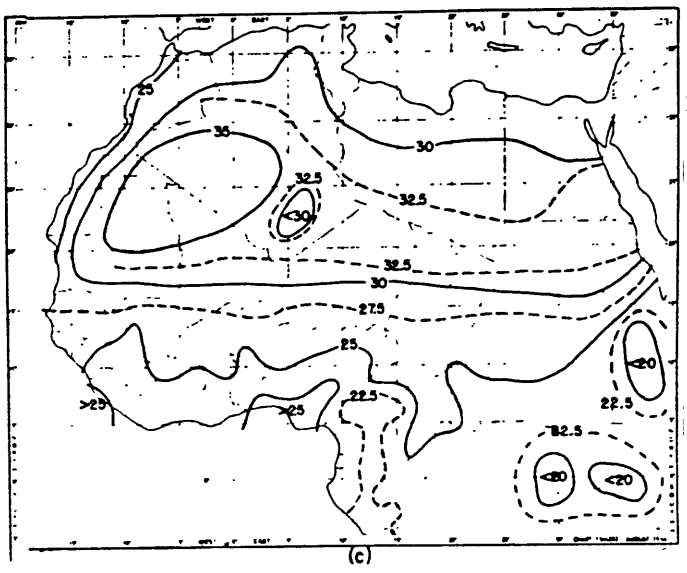

Fig. 20 Monthly mean maps for August daily average surface temperature.

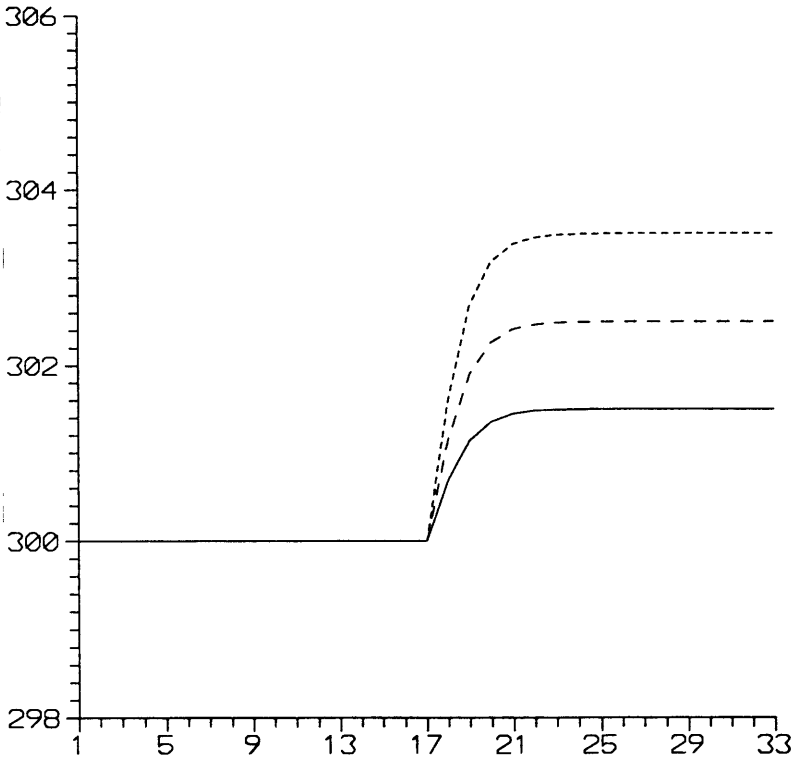

Fig. 21 Meridional distribution of surface temperature, short dashed with temperature difference bewteen land and ocean of 3.5 K, long dashed of 2.5 K for control run, solid curve of 1.5 K.

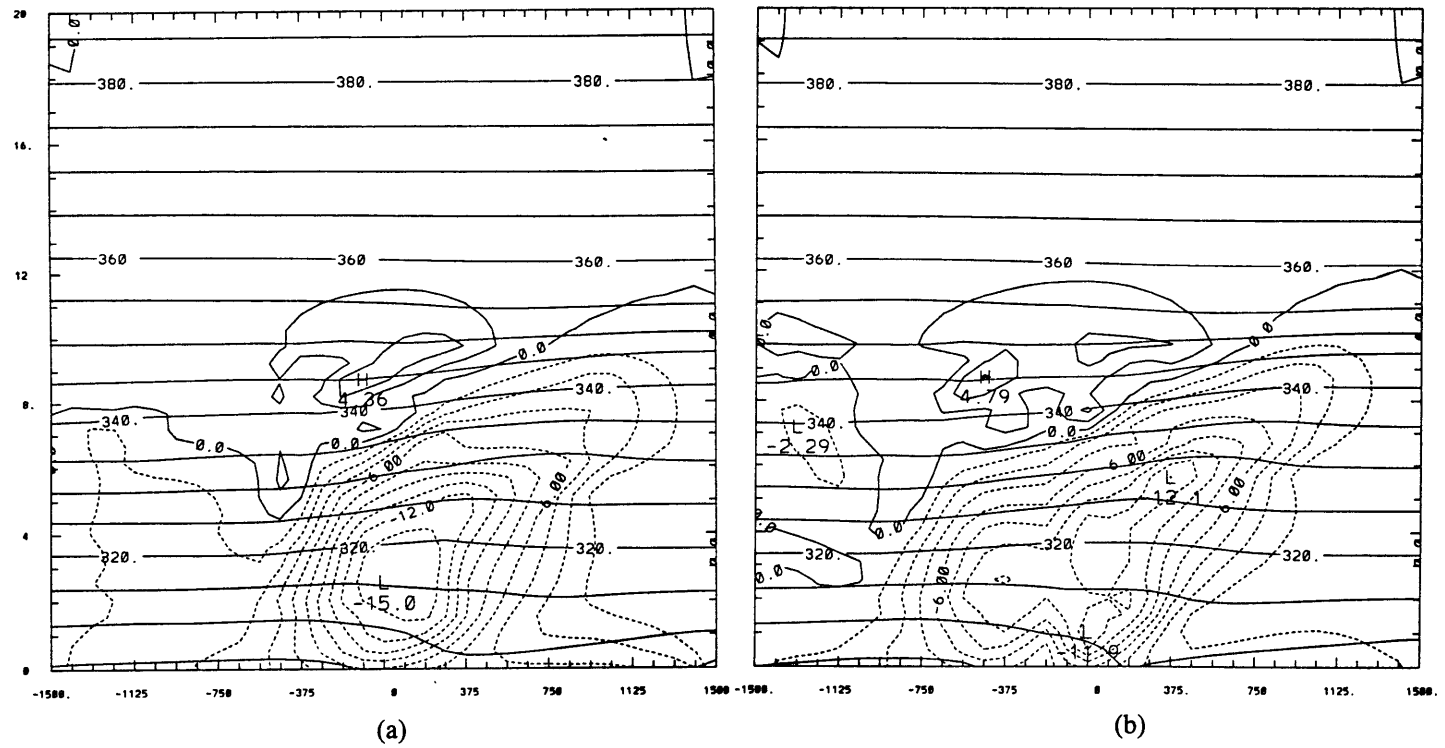

Fig . 22 The y-z vertical cross-sections for mean zonal wind profile, interval of 2m/sec. (a) sensitivity with higher temperature gradient than the control run, (b) sensitivity with lower temperature gradient than the control run.

7.3 Different Background Relative Humidity

Since we are treating this boundary condition problem from an aspect of quasi-equilibrium, the equilibrium state should not be sensitive to the background relative humidity. In this section we explore this sensitivity. An alternative initial background relative humidity is shown in Fig. 23. Relative humidity linearly decreases with height and also has variation in the y direction.

The results only show some minor difference between the two experiments. Comparing to table 2, the mean zonal wind for this experiment has jet core located at $4.0km$ with peak value of $13.4m/sec$. Vertical wind shear below the jet is $2.69m/(sec \cdot km)$. Basically, the results are almost the same as in the control run.

7.4 Different Water Vapor Fluxes

The surface water vapor fluxes are calculated using a simple bulk aerodynamic formula. The surface wind speed and degree of sub-saturation determine the magnitude of the flux. In this section we test the sensitivity of the equilibrium state to the water vapor flux when the contrast of water vapor flux between ocean and land is reduced.

Since the saturation water vapor pressure $e_s(T)$ is only a function of temperature, higher temperature has a higher value of e_s, and thus higher saturated specific humidity. To use the bulk aerodynamic formula to parameterize the water vapor flux from the ocean surface, we usually use a saturation value for the ocean surface. However, it is questionable to do the same thing over the land, especially for the very dry conditions over the Sahelian to sub-Sahelian regions. Thus, we modify the formula and use a surface specific humidity linearly decreasing northward. The formula has the form of

$$q_{surf} = q_s(SST) \times [1 - (j - j_0) \times Grad],$$

where $surf$ denotes the surface, $Grad$ denotes the gradient, j is the grid number in y direction and j_0 is a reference point. Thus, the surface specific humidity used for the land condition has a sub-saturation value since the land is relatively dry.

We change the gradient of surface specific humidity to explore the sensitivity. The control

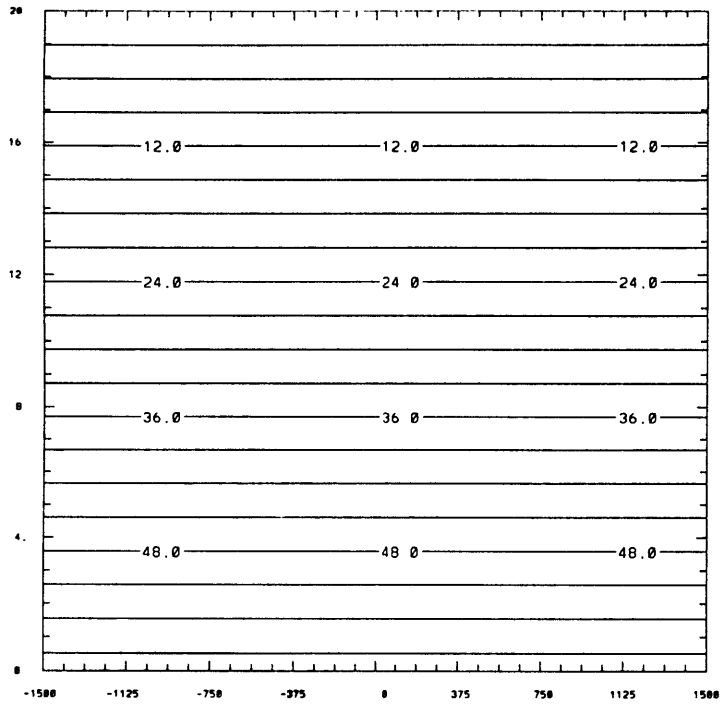

Fig. 23 The y-z vertical cross-section of background relative humidity.

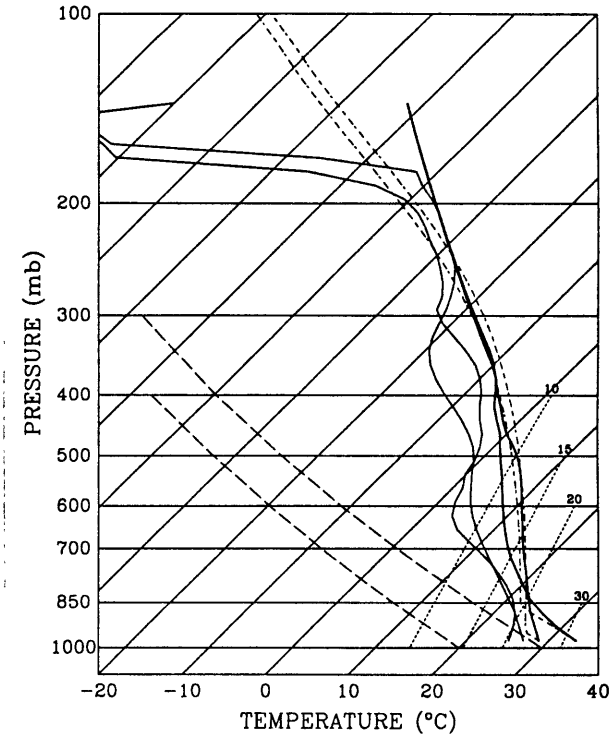

Fig. 24 The equilibrium sounding.

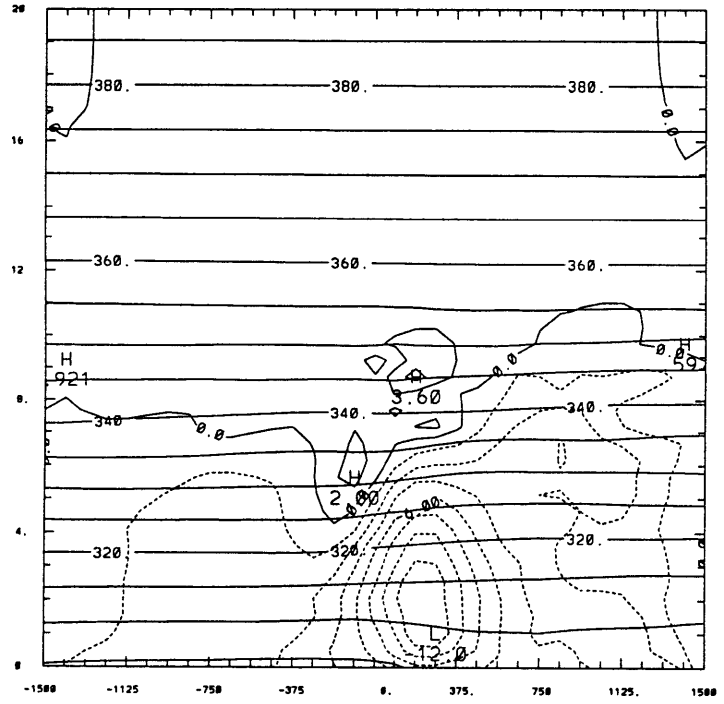

Fig. 25 The y-z vertical cross-section of mean zonal wind profile, contour interval of 2 m/sec.

run uses a $Grad$ of 0.014 and $j_0 = 7$. The experiment with a surface specific humidity gradient of 0.008 and $j_0 = 14$ shows substantial differences with the control run. Fig. 24 shows the equilibrium sounding as in Fig. 14b. Due to ample water vapor flux input from the lower boundary, the difference in relative humidity between the two soundings is greatly reduced. Note the temperature and dew point temperature profiles for the land especially. Fig. 25 is the zonal wind profile. The jet forms at a lower altitude than the control run with a weaker easterly maximum.

It's obvious that the result is sensitive to the water vapor flux over the land. To what extent using the simple Bulk aerodynamic formula to parameterize the water vapor flux over the arid area is a valid approximation still needs further investigation to validate. The effort to more accurately parameterize the fluxes over the land thus become one of the critical issues in the African wave dynamics.

Chapter 8

African Wave Experiments

In this chapter, zonally periodic temperature perturbations of low amplitude will be introduced at the lower boundary with small initial amplitude. The initial perturbations in part II are the same as in part I. However, the basic state is the equilibrium state obtained in the control run in last chapter. In order to see how the African waves act to change the surface fluxes, the lower boundary wind speed instead of a constant wind speed is used in the bulk aerodynamic formulae.

The stability of the equilibrium state without African waves has been surveyed and described in the last chapter. We will use the equilibrium state from last chapter as the basic state to examine the structure and energetics of the African waves below. Furthermore, the composite results of Reed et al. (1977. R77 hereafter), which show the vertical and horizontal structure of the African waves, are collected in Appendix 2 for comparison.

8.1 Vertical Structure

The x-z cross-sections along the jet core are now presented for fields of meridional wind, temperature, perturbation zonal wind, vorticity, perturbation potential vorticity, and vertical velocity after 7 days of integration.

The meridional wind shown in Fig. 26a has one maximum near the jet level at 4 km level and another maximum near the surface. The maximum at the surface is a dynamic response to the initial temperature anomalies put at the lower boundary. The other comes from the release

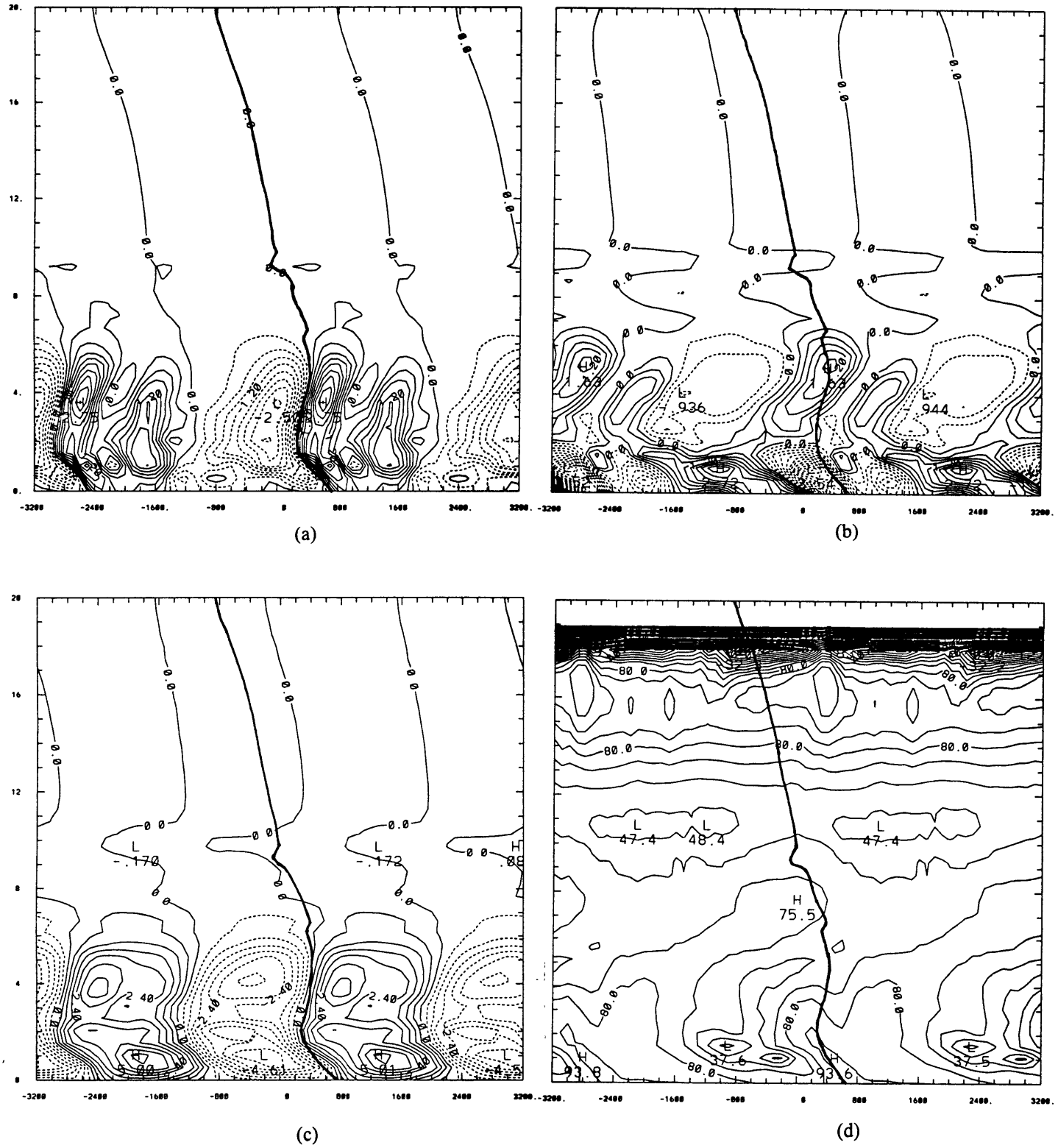

Fig. 26 The x-z vertical cross-sections along the jet meridian (a) meridional wind, contour interval of 0.3 m/sec, (b) perturbation potential temperature, contour interval of 0.3 K, (c) perturbation zonal wind , contour interval of 0.6 m/sec, (d) relative humidity, contour interval of 10%.

of shear instability. The trough can be identified as the location where the meridional velocity is zero and is marked by heavy solid line. The height of the easterly jet is 4.1 km, see Fig. 14a. As shown in this figure, the vertical profile of the trough line tilts eastward with height below the jet and above 1.5km but tilts westward with height above the jet. The tilting direction is basically against the wind shear of the base-state zonal flow. It is consistent with the results of Mass (1978). For the x-z cross-sections along the jet core, the vertical tilting displays a baroclinic structure, whereas for poleward and equatorward regions the tiltings become small (not shown here). Since the horizontal temperature gradients in the regions away from the jet zone are small, the system has small baroclinicity there.

The temperature fields have opposite signs, separated by the 2km height level, as seen in Fig. 26b. It should also be noted that the trough is cold core below 2 km and warm core between 2 to 6.5 km. The ridge line has opposite juxtaposition with warm core below and cold core above. This is consistent with the observations, see Appendix 2. The relative humidity field increases in the rear of the trough due to the northward humidity flux and ascent. Higher relative humidity is concentrated around the trough zone as shown in Fig. 26d.

The perturbation zonal wind, shown in Fig. 26c, also has structure to that of the trough. Note the region between 1.5 and 6.5 km where the trough line basically coincides with the zero line of u', which shows strong positive correlation between u' and v'. Fig. 27a shows a y-z cross section of the horizontal momentum flux $\overline{u'v'}$. With the distribution of the jet structure, the conversion from zonal mean kinetic energy to eddy kinetic energy (CK) is positive in the disturbances, as shown in Fig. 27b. The eddies are growing in expense of zonal mean wind through positive barotropic energy conversion.

Consistent with the thermal wind equation, the vorticity has a maximum of $3.28\times10^{-5}\text{sec}^{-1}$ near the jet level as shown in Fig. 28a. The order of magnitude is very close to the observed values. The GATE composite in R77 had a maximum of $3.0 \times 10^{-5}\text{sec}^{-1}$ just below the jet. The vorticity of the GATE composite is dominated by cyclonic vorticity around the jet level, with the largest anti-cyclonic vorticity at about 12km. It is clearly not a simple sinusoidal structure in R77, which suggests that nonlinear process might be important in nature. There is a clear eastward tilting with height above 1.5km towards the maximum near the jet level in Fig. 28a; above the jet there is only minor westward tilting with height. The x-z cross-section

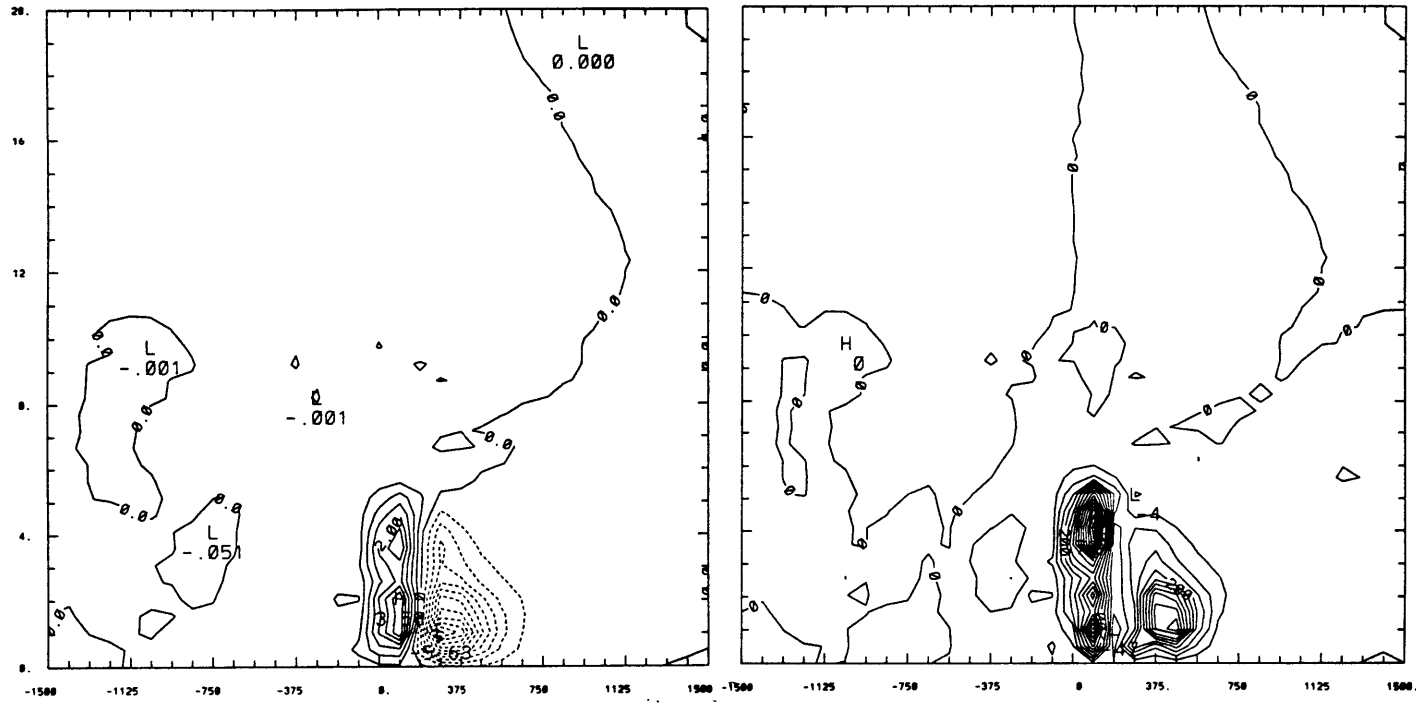

Fig. 27 The vertical cross-sections for (a) y-z profile of u'v', contour interval of 0.5 m^2/sec^2, (b) y-z profile of CK (ZKE->EKE), contour interval of 0.5-5sec-1, label scaled by 1.e+7.

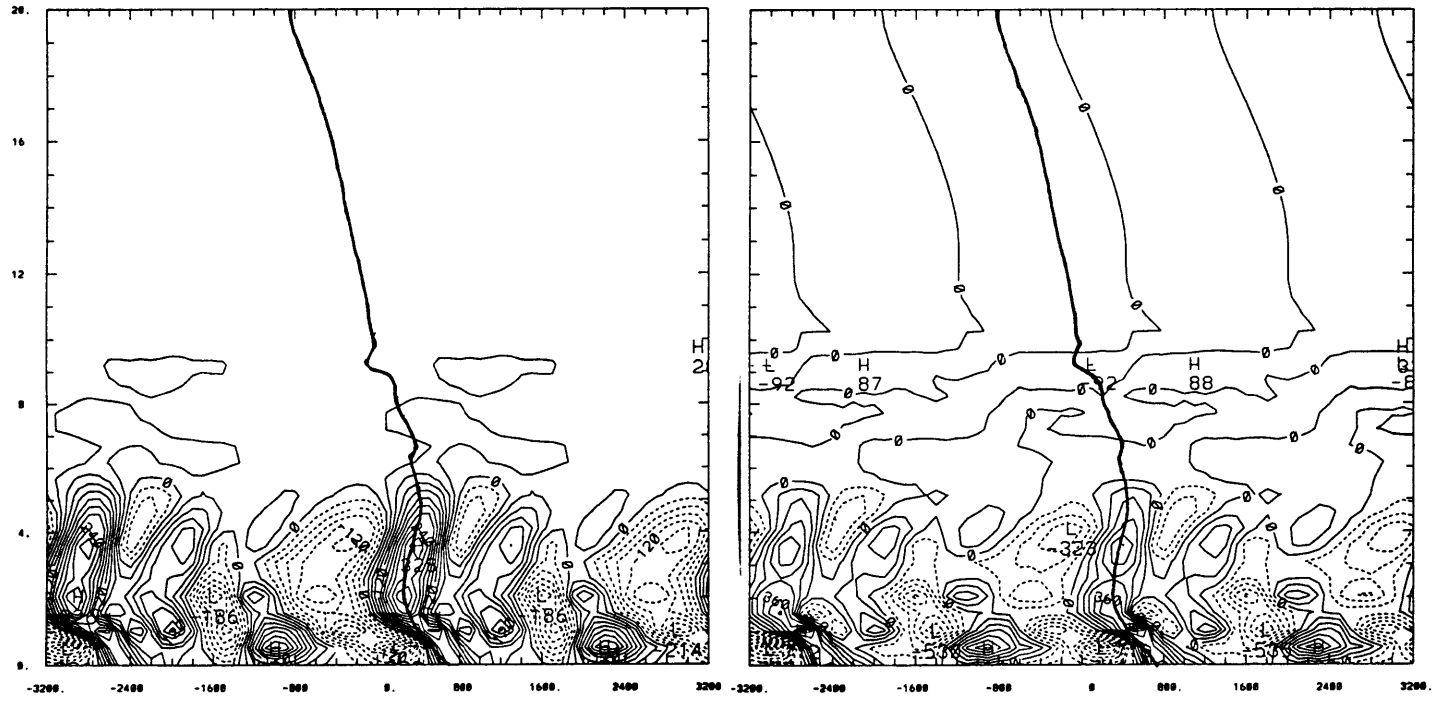

Fig. 28 The vertical cross-sections for (a) x-z profile of vorticity, interval of 0.3e-5 sec-1, label scaled by 1.e+7, (b) x-z profile of perturbation PV, interval of 0.9e-5 sec-1, label scaled by 1.e+7.

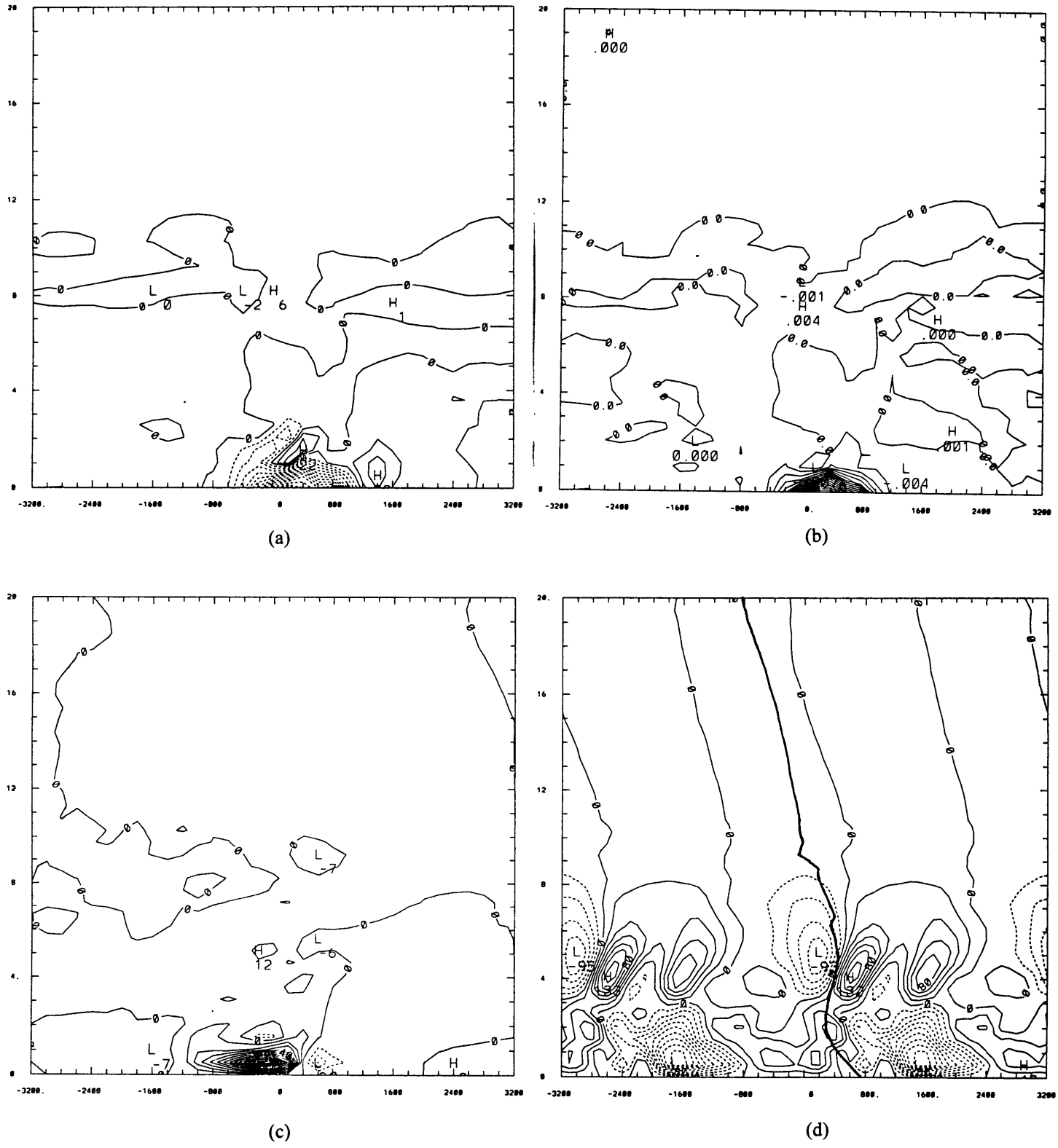

Fig. 29 The vertical cross-sections for (a) y-z profile of v'T', contour interval of 0.8e-2 K*m/sec, label scaled by 1000., (b) y-z profile of CA (ZAPE-->EAPE), contour interval of 0.8e-2 sec-1, (c) y-z profile of CE (EAPE-->EKE), interval of 0.1e-2, label scaled by 1.e+4, (d) x-z profile of vertical velocity, interval of 0.2e-2m/sec.

The x-z cross-section of perturbation potential vorticity is shown in Fig. 28b. Basically, the pattern is similar to that of the vorticity.

The eddy heat flux $\overline{v'T'}$ is shown in Fig. 29a. Negative value indicates that warm air moves with the northerly and cold air with southerly. With the distribution of base-state potential temperature, there exists a positive conversion CA from zonal mean available potential energy to eddy available potential energy as shown in Fig. 29b. The conversion is positive but confined to low levels. The vertical velocity diagnosed from the omega equation has a checkerboard pattern, as shown in Fig. 29d, which is consistent with quasi-geostrophic theory. A vorticity anomaly on a jet with opposite baroclinicity above and below immediately gives this checkerboard pattern (Hoskins and Pedder, 1980). Note that there is upward motion below the jet and downward motion west the trough above the jet. Fig. 29c show that the vertical heat fluxes $\overline{w'T'}$ are positive. It implies a positive baroclinic energy conversion CE from the eddy available potential energy to eddy kinetic energy through thermal direct circulation. As warm air moves southward, it is accompanied by upward motion, and vice versa.

8.2 Horizontal Structure

In this section, perturbation potential vorticity and absolute vorticity at 3 km level and temperature at the lowest level will be used to illustrate the horizontal structure of African waves. Fig. 30a shows the meridional velocity at z = 3km, with the position of the trough marked in the x - y plane. The wave axis has a pronounced northeast-southwest tilt at this level. This level is just below the jet core (Fig. 14a). As shown in last section, there is a strong northward transport of westerly momentum and a conversion of zonal kinetic energy into eddy kinetic energy. Potential vorticity anomalies are present in the different regions of potential vorticity gradient (Fig. 18). The largest potential vorticity anomalies are at the jet region while the weaker ones on the flanks. Where there is a positive mean potential vorticity gradient, a southward motion will induce positive potential vorticity anomalies. Thus, according to the potential vorticity gradient distribution shown in Fig. 18, a similar distribution of potential vorticity anomalies exist west of the trough, see Fig. 30b. The opposite distribution of potential vorticity anomalies exist east of the trough.

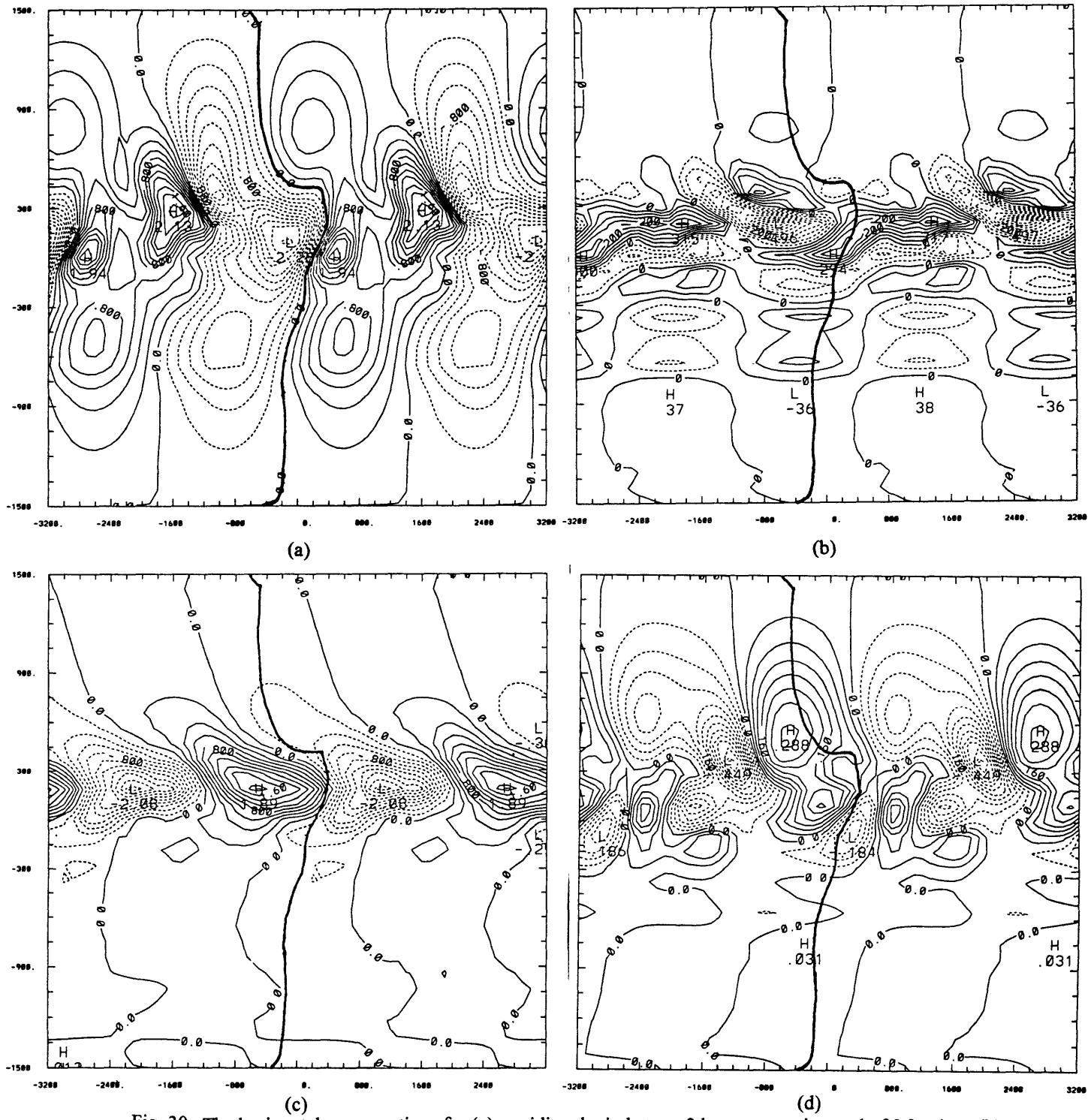

Fig. 30 The horizontal cross-sections for (a) meridional wind at z = 3 km, contour interval of 0.2 m/sec, (b) perturbation PV at z = 3 km , contour interval of 0.5e-5 sec-1, labels scaled by 1.e+7. (c) surface perturbation potential temperature, contour interval of 0.2 K, (d) perturbation potential temperature at z = 3 km, contour interval of 0.04 K, (e) vertical velocity at z = 3 km, contour interval of 0.8e-3 m/sec, labels scaled by 1.e+5, (f) precipitation rate, interval of 1mm/day.

The temperature perturbations at the surface, shown in Fig. 30c, have a simple sinusoidal variation. The relative vorticity perturbations at low levels are also consistent with this pattern, with cold temperature anomalies accompanied by negative vorticity anomalies and vice versa (not shown here). The surface temperature trough, shown in Fig. 31c, lags the streamline trough line about 1/4 wavelength at the jet zone. The temperature perturbations at 3km level, Fig. 30d, have a more complicated structure. This lagging phase leads to a negative correlation of $\overline{v'T'}$ at the jet zone meridian and trivial correlation elsewhere. This implies a down gradient heat transport. The vertical velocity field at 3km level is shown in Fig. 30e. Note that at the jet zone there is upward motion west of the trough. Away from the jet zone there is downward motion west of the trough. As seen in Fig. 30d the vertical motion is controlled by the temperature advection. At the jet zone, where the temperature gradient concentrates, the northerlies west of the trough accompany a positive temperature anomaly, leading to warm advection and induces upward motion, and vice versa. Thus the zonal available energy is transformed into eddy available energy which in turn is transformed to eddy kinetic energy. Therefore, we can conclude that eddies grow at the expense of zonal mean APE and KE through both barotropic and baroclinic processes. The strength of the jet weakens during the growing stage of the disturbances. However, the weakening is not substantial, since the boundary fluxes maintain the strength of the jet.

Fig. 30f shows the geographical distribution of the precipitation rate. The trough line at 4km level (about jet level) is marked to identify their relative position. The large precipitation rate is located in the jet zone, especially under and west of the trough. The arc-shape patterns is mainly associated with the mid-level trough. Apparently. the convective precipitation is leading the mid-level trough. Alternatively speaking, convection is enhanced by the approach of a mid-level trough in the easterlies as the observations indicate (Aspliden et al. 1976; McGarry and Reed 1977; Frank 1978; Thompson et al. 1979). The precipitation rate has a maximum value of 28mm/day which is very close to the observed value of greater than 20mm/day described in R77.

The vertical and horizontal structure shown above reveal that African waves grow through both baroclinic and barotropic energy conversions. The zonal mean wind profile is weakened both vertically and horizontally because the energy is converted into eddy APE and KE. Con-

vection is correlated with the approach of mid-level trough. The numerical results are both quantitatively and qualitatively in agreement with the observed structure and energetics. Convection is greatly enhanced due to large-scale forcing from African wave disturbances. The structure and evolution of the African wave disturbances are influenced by the inclusion of convective effects.

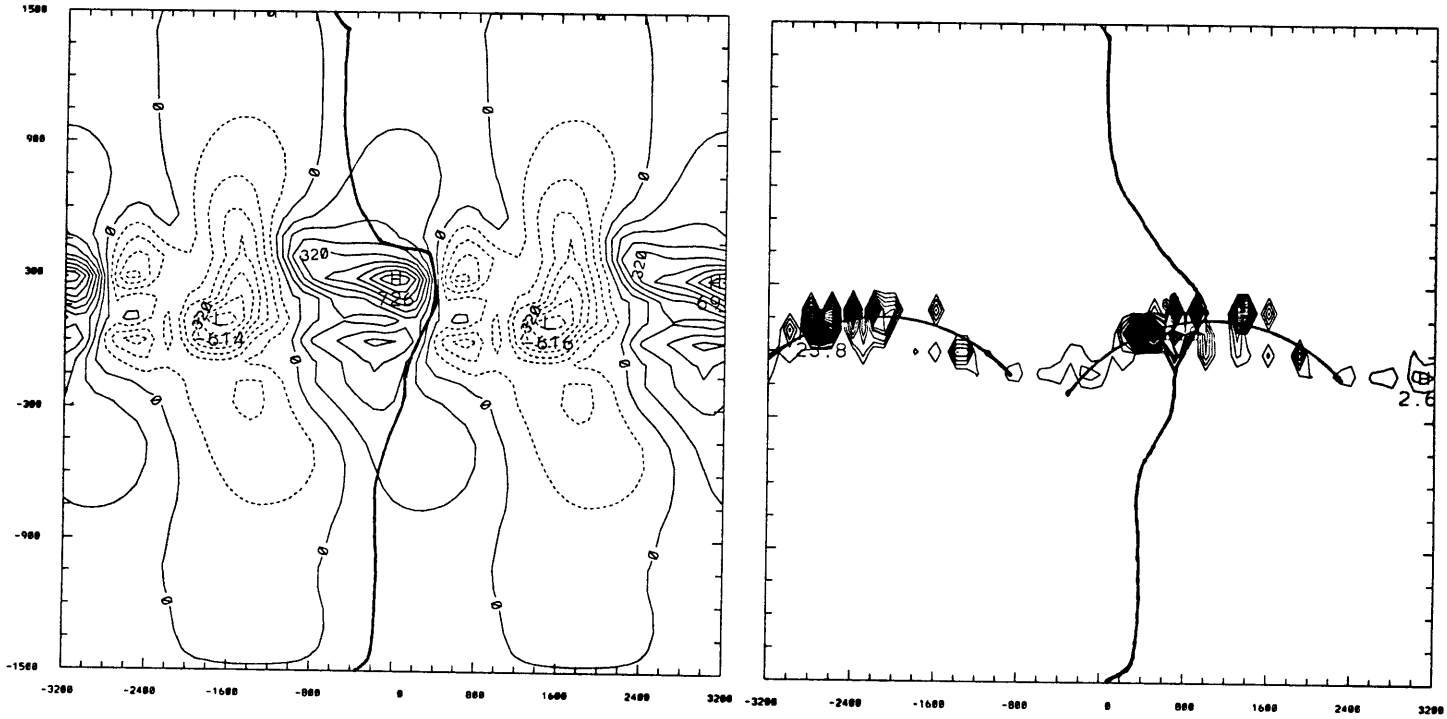

(e) (f)

Fig. 30 continued

Chapter 9

Conclusions and Implications

According to the above calculations and methodology we have used, the following conclusions can be made:

1. The evolution and structure share some common characteristics with the observations in the initial value experiments. However, the vertical motion is too weak compared to the observations.

2. The water vapor is not included in Part I. Thus, the relationship between convection and African waves cannot be discussed. The energy conversion and time series in the linear stage are quite similar to observations.

3. Sensitivity experiments show that in the relaxation experiment, which restores the basic state to the initial condition, the energy of the disturbances grows with time but has no sign of decaying. The experiment with Ekman damping shows that the conversion terms are significantly weaker than thore in the control run.

4. The experiment with both Ekman damping and relaxation shows that the system reaches a state of dynamic equilibrium. Total eddy energy, EKE and EAPE all reach and stay at an equilibrium level.

5. The jet-like easterly wind profile forms due to the contrasting surface fluxes. The equilibrium state potential vorticity gradient satisfies the Charney-Stern criterion for instability. The whole problem has been approached as a boundary value problem instead of an initial value problem. Any particular case study is not our intention here. We explicitly hypothesize quasi-equilibrium using the Emanuel scheme to include the convective effects.

6. The sensitivity experiments show that the SST is important in determining the height of the jet and strength of vertical wind shear below the jet. Further observational evidence and numerical study is needed to evaluate their relationship to the organization of convection over the Atlantic region. Reanalyses can be used to examine these. Higher SST increases the strength of the lifted African easterly jet and the vertical wind shear below the jet. This jet property may thus help to organize convection over the Atlantic ocean. On the other hand, observational evidence showed that increase in SST leads to reduced rainfall over sub-Sahelian region. The dynamics seems to be even more complicated. The delicate circulation needs further investigation with consideration of monsoon circulation for example. In that case, a zonally symmetric model (Zheng 1997; Plumb and Hou 1992) would be appropriate to see the effect of large-scale meridional circulation on the rainfall variability over the sub-Sahelian region. Our results show that the SST is linked to the dynamics of the sub-Sahelian region. I hypothesize that the change in SST leads to changes in the properties of African easterly jet and African waves, which in turn control the rainfall variability of the sub-Sahelian region.

7. Both the boundary fluxes and radiative cooling are important physical mechanisms to determine the final equilibrium state. The sensitivity experiment shows that the equilibrium state is sensitive to the water vapor flux over the land. Therefore, more accurate hydrological processes are needed to determine the influence of boundary fluxes on the behavior of African wave dynamics. The feedback of the atmosphere to the ocean fluxes is ignored here but could be important in nature. The effort to more accurately parameterize the fluxes over the land thus becomes one of the critical issues in the African wave dymanics.

8. In this paper, we use constant radiative cooling rates for the troposphere and stratosphere, respectively. A radiative transfer package should be used in order to account for the effects of water vapor in the vertical distribution of net radiative cooling. In Robe and Emanuel's (1996) simulations, the cloud mass flux is very sensitive to the imposed radiative cooling rate.

9. From the African wave experiments we can see that the basic structure and energetics of this simulation are similar to the observations. The disturbances grow in amplitude and magnitude through both barotropic and baroclinic energy conversions. The trough line has cold core below and warm core above structure. Maximum vorticity has the same order of magnitude and position as the observations show.

10. The distribution of precipitation rate has maximum located below the mid-level trough and westward. The approach of mid-level trough enhances the convection. Obviously, the distribution shows a leading phase to the trough. The results are similar to the observation both in position and magnitude.

11. The quasi-equilibrium experiment shows that the structure and evolution of the African wave disturbances are influenced by the inclusion of convective effects. Convection is greatly enhanced due to large-scale forcing from African wave disturbances. The mutual two-way interaction between convection and African waves once again becomes evident.

12. Topography over North Africa is an important feature ignored in this paper. In African wave experiment, the initial disturbances are assigned as periodic anomalies at the lower boundary. In order to study the initiation of wave disturbances, it would be desirable to include topography in future experiments. Simple topography can be adopted to investigate the dynamic role of topography in the initialization and tracking of disturbances by interfering the upstream flow.

13. Cumulus clouds are believed to play an important role :in the large-scale dynamics. However, further examination of the momentum and vorticity budget including cumulus downdrafts is necessary in order to correctly account for the effects of convection on the large-scale flow. Hopefully, understanding in this issue will help in improving convective parameterization.

14. The African monsoon flow obviously contributes to the large-scale low-level convergence. Although it is not considered in this paper, its importance cannot be negated.

15. The tropical easterly jet near 200 mb is another important feature over this region. The vertical coupling of divergence fields between the African jet and the Tropical easterly jet can cooperate to enhance the convection. Since we are solving a boundary condition problem here, the Tropical easterly jet cannot be included. However, they can be investigated by using an idealized zonal mean state.

16. The quasi-geostrophic model is useful in isolating the physical processes and interpreting their dynamic mechanisms. Nonetheless, if the goal is to simulate any particular case or to consider more complex situation, a more accurate model is necessary. Since we are here to approach this problem from an aspect of quasi-equilibrium, the quasi-geostrophic model can still serve this need.

17. As discussed in chapter 1, the African jet and African waves usually have the important effect of promoting strong cumulus-scale and meso-scale convection. Nevertheless, the effects of convection is not explicitly resolved but parameterized. One interesting and informative experiment is to see how an explicitly resolved convective system behaves under the large-scale forcing. The idea is that we can use the broad trough region of the equilibrium state as a background state and redo the experiments similar to Fovell and Ogura's (1989) or Robe and Emanuel's (1996) experiments to see the effect of dynamic forcing of the African wave on the convective systems. The common feature in their studies is that they all run the model until the system reaches a state of statistical equilibrium. We have approached the topic from a different direction. Here we have concentrated on the large-scale circulation but theirs concentrated on mesoscale circulations.

Appendix 1: The Energy Equations, EP flux and ω equation

The appropriate equations for investigating the growth of wave energy were first derived by Lorenz (1955). He expressed the time rate of change of eddy kinetic energy and eddy available energy as follows:

$$\frac{\partial K_E}{\partial t} = C_E + C_K$$

and

$$\frac{\partial A_E}{\partial t} = C_A - C_E$$

where K_E is the eddy kinetic energy, A_E the eddy available potential energy, C_K the conversion of zonal kinetic energy to eddy kinetic energy, C_E the conversion of eddy available potential energy to eddy kinetic energy, C_A the conversion of zonal available potential energy to eddy available potential energy and t is time. The expressions for these energies and conversions appear below.

$$K_E = \int_0^{z_t} \rho_s \left[\frac{\overline{u'^2 + v'^2}}{2}\right] dz,$$

$$A_E = \left(\frac{g}{f_0\theta_0}\right)^2 \int_0^{z_t} \rho_s \left[\frac{\overline{\theta'^2}}{2S}\right] dz,$$

$$C_K = -\int_0^{z_t} \rho_s \left[\frac{\partial \overline{u}}{\partial y}\overline{u'v'}\right] dz,$$

$$C_A = -\left(\frac{g}{f_0\theta_0}\right)^2 \int_0^{z_t} \rho_s \left[\frac{\partial \overline{\theta}}{\partial y}\frac{\overline{\theta'v'}}{S}\right] dz,$$

$$C_E = \frac{g}{\theta_0} \int_0^{z_t} \rho_s \left[\overline{w'\theta'}\right] dz,$$

In the above expressions $\overline{(\quad)}$ represents a zonal average and $[\overline{(\quad)}]$ represents a meridional average of the zonal average. A prime indicates a deviation from a zonal average.

Eliassen-Palm (EP) flux and its divergence is a very useful way of summarizing the barotropic and baroclinic energy fluxes. Edmon *et al.*(1980) showed how this diagnostic can be related

to wave-action and group-velocity concepts. In z coordinate, the quasi-geostrophic EP flux is given in standard notation as

$$F = (0, -\rho_0 \overline{u'v'}, \frac{\rho_0 f_0}{\partial\theta/\partial z} \overline{v'\theta'}).$$

Vertical velocity is diagnosed by solving the W-equation. The W-equation in z coordinate is

$$\nabla^2 W + S^{-1} \frac{1}{\rho_s} \frac{\partial^2}{\partial z^2}(\rho_s W) = \frac{1}{S f_0} \left(\nabla^2 [-V_g \cdot \nabla(\frac{\partial \psi}{\partial z})] - \frac{\partial}{\partial z}[-V_g \cdot \nabla(\nabla^2 \psi + \beta y)] + \frac{g}{f_0 \theta_0} \nabla^2 (\frac{Q}{C_p}) \right)$$

with the boundary conditions of $W = 0$ at both $z = 0$ and $z = z_t$.

Appendix 2: The figures from Reed *et al.* 1977

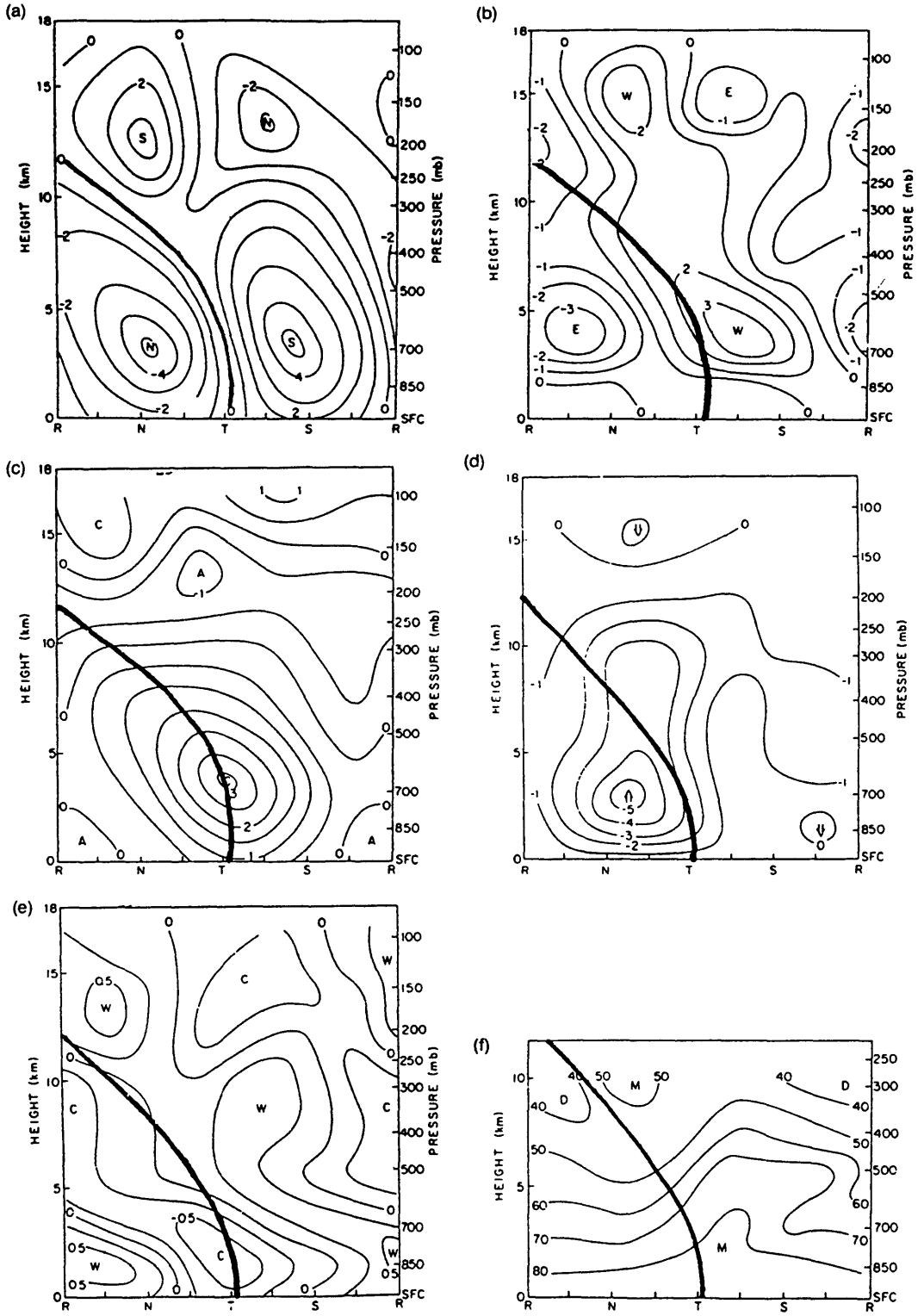

Vertical cross sections along reference latitude (11°N) of the composite easterly wave from Reed et al. (1977): (a) meridional wind (m s^{-1}), (b) zonal wind (m s^{-1}), (c) total relative vorticity (10^{-5} s^{-1}), (d) vertical motion (mb h^{-1}), (e) temperature (°C), and (f) relative humidity (%). Symbols R, N, T, and S refer to ridge, north wind, trough, and south wind sectors of the wave, respectively. The trough is indicated as a thick line.

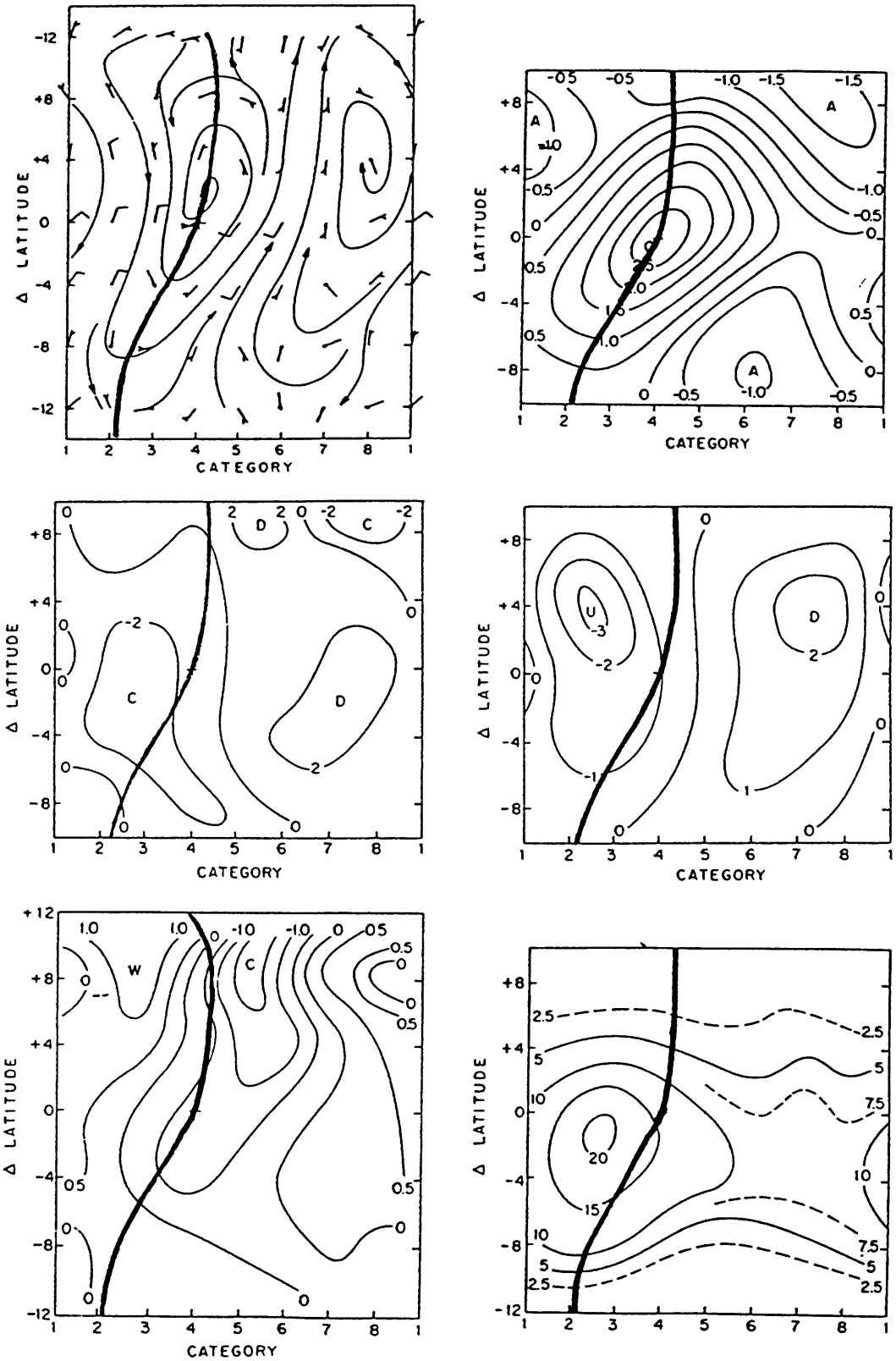

Horizontal structure of the composite easterly wave from Reed et al. (1977): (a) streamlines at 700 hPa, (b) total relative vorticity (10^{-5} s^{-1}) at 700 hPa, (c) divergence (10^{-6} s^{-1}) at surface, (d) vertical motion (mb h^{-1}) at 850 hPa, (e) temperature (°C) at 850 hPa, and (f) average precipitation rate (mm day^{-1}). The trough at 700 hPa is indicated as a thick line. The wave is divided in 8 categories: category 4 shows the trough and category 8 the ridge. Here Δ latitude = 0 corresponds to average latitude of the disturbance path (11°N).

Appendix 3: The figures from Norquist *et al.* 1977

The meridional distribution of energy conversions C_K, C_A and C_E calculated by Norquist et al. (1977) are shown below for comparison.

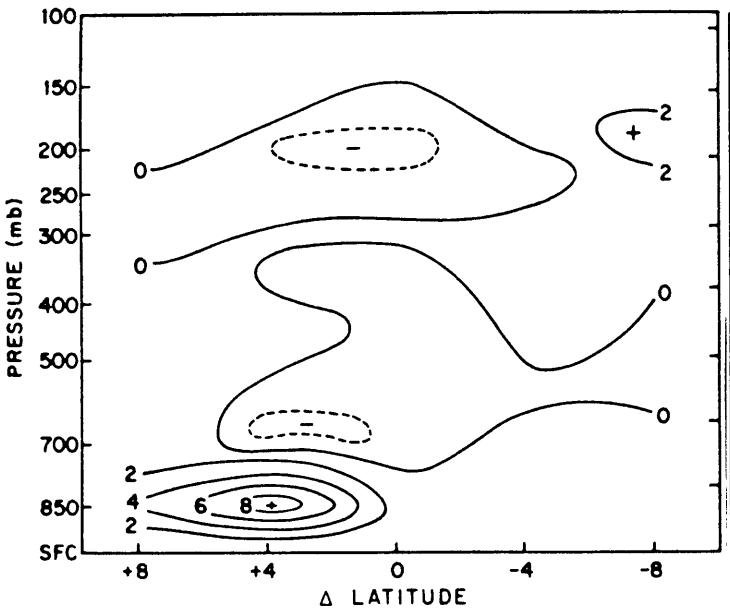

Meridional distribution of $-g\bar{\sigma}^{-1}[v'T']\partial[T]/\partial y$ for the combined region. Units are 10^{-5} m^2 s^{-3}.

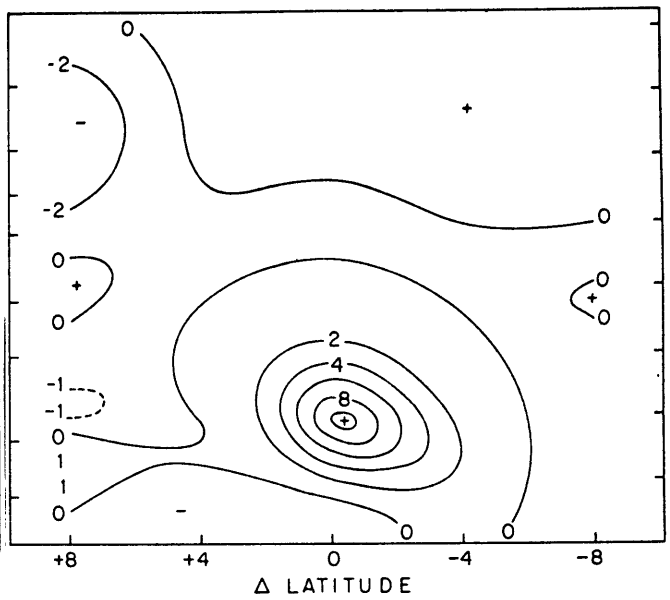

Meridional distribution of $-[u'v']\partial[u]/\partial y$ for the combined region. Units are 10^{-5} m^2 s^{-3} (or W kg^{-1}).

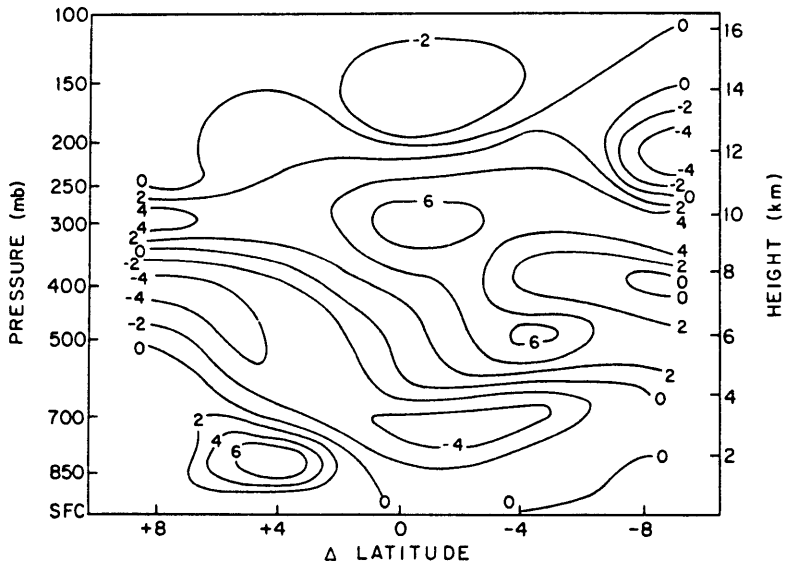

Meridional distribution of $-R\bar{p}^{-1}[\omega'T']$ for the combined region. Units are 10^{-5} m^2 s^{-3} (or W kg^{-1}).

Bibliography

[1] Anthes R. A., 1982: Tropical Cyclones: Their Evolution, Structure, and Effects. *Meteor. Monogr.*, No. **41**, Amer. Meteor. Soc., pp. 208.

[2] Arakawa A. and W. H. Schubert, 1974: Interaction of a cumulus cloud emsemble with the large-scale environment, Part I. *J. A. S.*, **31**, pp. 674-701.

[3] Aspliden C. I., Y. Tourre and J. B. Sabine, 1976: Some climatological aspects of West African disturbances lines during GATE. *Mon. Wea. Rev.*, **104**, pp.1029-1035.

[4] Avila L. A., 1991: Eastern North Pacific hurricane season of 1990. *Mon. Wea. Rev.*, **119**, pp. 2034-2046.

[5] Avila L. A. and R. J. Pasch, 1992: Atlantic tropical systems of 1991. *Mon. Wea. Rev.*, **120**, pp. 2688-2696.

[6] Bah A., 1987: Towards the prediction of Sahelian rainfall from sea surface temperatures in the Gulf of Guinea. *Tellus*, **39A**, pp. 39-48.

[7] Bakun A., 1978: Guinea current upwelling. *Nature*, **271,** pp. 147-150.

[8] Bretherton F. P., 1966: Critical layer instability in baroclinic flows. *Q. J. R. Meteorol. Soc.*, **92**, pp. 325-334.

[9] Brown R. G. and C. S. Bretherton, 1997: A test of the strict quasi-equilibrium theory on long time and space scales. *J. A. S.*, **54**, pp. 624-638.

[10] Burpee R. W., 1972: The origin and structure of easterly waves in the lower troposphere of North Africa. *J. A. S.*, **29**, pp. 77-90.

[11] Carlson T. N., 1969: Synoptic histories of three African disturbances that developed into Atlantic hurricanes. *Mon. Wea. Rev.,* **97**, pp. 256-276.

[12] Charney J. G. and M. E. Stern, 1962: On the instability of internal baroclinic jets in a rotating atmosphere. *J. A. S.*, **19**, pp. 159-172.

[13] Chen Y.-L. and Y. Ogura, 1982: Modulation of convective activity by large scale flow patterns observed in GATE. *J. A. S.*, **39**, pp. 1260-1279.

[14] Cook Y.-L. and Y. Ogura, 1982: Modulation of convective activity by large scale flow patterns observed in GATE. *J. A. S.*, **39**, 1137-1152/

[15] Druyan L. M., 1989: Advances in the study of sub-Sahara drought . *Int. J. Climatol.*, **9**, pp. 77-90.

[16] Druyan L. M. and T. Hall, 1996: The sensitivity of African wave disturbances to remote forcing. *J. Appl. Meteor.*, **35**, pp. 1100-1110.

[17] Druyan L. M., P. Lonergan and M. Saloum, 1996: African wave disturbances and precipitation at Niamey during July-August 1987 and 1988. *Climate Res.*, **7,** pp. 71-83.

[18] Druyan L. M., P. Lonergan and J. Cohen, 1997: Case studies of African wave disturbances in gridded analyses. *Mon. Wea. Rev.,* **125**, pp. 2520-2530.

[19] Duvel J. P., 1990: Convection over tropical Africa and the Atlantic ocean during northern summer. Part II: Modulation by easterly waves. *Mon. Wea. Rev.,* **118**, pp. 1855-1868.

[20] Edmon H. J., Hoskins B. J. and J. G. Jing, 1983: Eliassen-Palm cross-sections for the atmosphere. *J. A. S.*, **37**, pp. 2600-2616.

[21] Emanuel K. A., 1986: An air-sea interaction theory for tropical cyclones. Part I: Steady-state maintenance. *J. A. S.*, **43**, pp.585-604.

[22] Emanuel K. A., 1987: An air-sea interaction model of intraseasonal oscillations in the tropics. *J. A. S.*, **44**, pp. 2324-2340.

[23] Emanuel K. A., 1991: A scheme for representing cumulus convection in large-scale models. *J. A. S.*, **48**, No. 21, pp. 2313-2335.

[24] Emanuel K. A., J. D. Neelin and C. S. Bretherton, 1994: On large-scale circulations in convecting atmospheres. *Q. J. R. Meteorol. Soc.*, **120**, pp. 1111-1143.

[25] Fontaine B., S. Janicot and V. Moron, 1995: Rainfall anomaly patterns and wind field signals over West Africa in August(1958-1989). *J. Climate*, **8**, pp. 1503-1510.

[26] Fovell R. G. and Y. Ogura, 1989: Effect of vertical wind shear on numerically simulated multicell storm structure. *J. A. S.*, **46**, pp. 3144-3176.

[27] Folland C. K., T. N. Palmer, and D. E. Parker, 1986: Sohel rainfall and worldwide sea temperatures, 1901-85. Nature ,**320**, pp. 602-605.

[28] Frank N. L., 1969: The "inverted V" cloud pattern—an easterly wave? *Mon. Wea. Rev.*, **97**, pp. 130-140.

[29] Frank W. M., 1978: The life cycles of GATE convective systems. *J. A. S.*, **35**, pp. 1256-1264.

[30] Gill A. E., 1982: Atmosphere-Ocean Dynamics. Academic Press. pp.662. 0

[31] Hoskins B. J., 1983: Dynamical processes in the atmosphere and the use of models. *Q. J. R. Meteorol. Soc.*, **109**, pp. 1-21.

[32] Hoskins B. J., M. E. McIntyre and A. W. Robertson, 1985: On the use and significance of isentropic potential vorticity maps. *Q. J. R. Meteorol. Soc.*, **111**, pp. 887-946.

[33] Hoskins B. J. and M. Pedder, 1980: The diagnosis of middle latitude synoptic development. *Q. J. R. Meteorol. Soc.*, **106**, pp. 707-719.

[34] Hoskins B. J. and A. J. Simmons, 1975: A multi-layer spectral model and the semi-implicit method. *Q. J. R. Meteorol. Soc.*, **101**, pp. 637-655.

[35] Jenkins G. S., 1997: The 1988 and 1990 summer season simulations for West Africa using a regional climate model. *J. climate*, **10**, pp.1255-1 272.

[36] Kidson J. W., 1977: African rainfall and its relation to the upper air circulation. *Q. J. R. Meteorol. Soc.*, **103**, pp. 441-456.

[37] Kuo. H. L., 1965: On formation and intensification of tropical cyclones through latent heat release by cumulus convection. *J. A. S.*, **22**, pp. 40-63.

[38] Kuo H. L., 1974: Further studies of the parameterization of the influence of cumulus convection on large-scale flow. *J. A. S.*, **31**, pp. 1232-1240.

[39] Kwon H. J., 1989: A reexamination of the genesis of African waves. *J. A. S.*, **46**, No. 24, pp. 3621-3631.

[40] Kwon H. J. and M. Mak, 1990: A study of the structural transformations of the African easterly waves. *J. A. S.*, **47**, pp. 277-292.

[41] Lamb P. J., 1978: Large-scale tropical Atlantic surface circulation patterns associated with sub-Sahara weather anomalies. *Tellus*, **30**, pp. 240-251.

[42] Lamb P. J., 1982: Persistence of sub-Sahara drought. *Nature*, **299,** pp. 46-48.

[43] Landsea C. and W. M. Gray, 1992: The strong associations between western Sahelian monsoon rainfall and intense Atlantic hurricanes. *J. Climat e*, **5**, pp. 435-453.

[44] Lindzen R. S., 1974: Wave-CISK in the tropics. *J. A. S.* , **31**, pp. 156-179.

[45] Lorenz E. N., 1955: Available potential energy and the maintenance of the general circulation. *Tellus*, **7**, pp. 157-167.

[46] McGarry M. M., and R. J. Reed, 1978: Diurnal variations in convective activity and precipitation during phases II and III of GATE. *Mon. Wea. Rev.*, **106**, pp. 101-103.

[47] Mass, C., 1977: A numerical and observational study of African wave disturbances. Ph.D. thesis, University of Washington.

[48] Miller R. L. and R. S. Lindzen, 1992: Organization of rainfall by an unstable jet with an application to African waves. *J. A. S.*, **49**, pp. 1523-1540.

[49] Molinari J., D. Knight, M. Dickson, D. Vollaro, and S. Skubis, 1997: Potential vorticity, easterly waves, and eastern Pacific tropical cyclogensis. *Mon. Wea. Rev.*, **125**, pp. 2699-2708.

[50] Moncrieff M. W. and M. J. Miller, 1976: The dynamics and simulation of tropical cumulonimbus and squall lines. *Q. J. R. M. S.*, **102**, pp. 373-394.

[51] Neelin J. D., I. M. Held and K. H. Cook, 1987: Evaporation-wind feedback and low-frequency variability in the tropical atmosphere. *J. A. S.*, **44**, pp. 2341-2348.

[52] Newell R. E. and J. W. Kidson, 1984: African mean wind changes between Sahelian wet and dry periods. *J. Climate*, **4**, pp. 27-33.

[53] Nitta T. and M. Yanai, 1969: A note on the barotropic instability of the tropical easterly current. *J. Meteorol. Soc. Jpn.*, **47**, pp. 127-130.

[54] Nitta T.: Response of cumulus updraft and downdraft to GATE A/B-scale motion systems. *J. A. S.*, **34**, pp, 1163-1186.

[55] Norquist D. C., E. E. Recker and R. J. Reed, 1977: The energetics of Africanwave disturbances as observed during phase III of GATE. *Mon. Wea. Rev.*, **105**, pp. 334-342.

[56] Paradis D., J.-P. Lafore and J.-L. Redelsperger, 1995: African easterly waves and convection. Part I: Linear simulations. *J. A. S.*, **52**, N0. 10, pp. 1657-1679.

[57] Pedlosky J.: 1979: Geophysical Fluid Dynamics. 2nd edition. Springer-Verlag, Berlin and New York. pp. 710.

[58] Plumb R. A. and A. Y. Hou, 1992: The response of a zonally symmetric atmosphere to subtropical thermal forcing: threshold behavior. *J. A. S.*, **49**, 1790-1799.

[59] Raymond D. J., 1975: A model for predicting the movement of continuously propragating convective storms. *J. A. S.*, **32**, pp. 1308-1317.

[60] Raymond D. J., 1976: Wave-CISK and convective mesosystems. *J. A. S.*, **33**, pp. 2392-2398.

[61] Raymond D. J., 1984: A wave-CISK model of squall lines. *J. A. S.*, **41**, pp. 1946-1958.

[62] Reed R. J. and E. E. Recker, 1971: Structure and properities of synoptic scale wave disturbances in the equatorial Western Pacific. *J. A. S.*, **28**, pp. 1117-1133.

[63] Reed R. J., D. C. Norquist and E. E. Recker, 1977: The structure and properties of African wave disturbances as observed during phase III of GATE. *Mon. Wea. Rev.*, **105**, pp. 317-333.

[64] Reed R. J., E. Klinker, and A. Hollingsworth, 1988: The structure and characteristics of African easterly wave disturbances as determ ined from the ECMWF operational analysis/forecast system. *Meteor. Atmos. Phy s.*, **38**, pp. 22-33.

[65] Reeves R. W., C. F. Ropelewski, and M. D. Hudlow, 1979: Relationships between large-scale motion and convective precipitation during GATE. *Mon. WEA. REV.*, **107**, pp. 1154-1168.

[66] Rennick A. J., 1976: The generation of African waves. *J. A. S.*, **33**, pp. 1955-1969.

[67] Rennó N. O., K. A. Emanuel and P. H. Stone, 1994: Radiative-convective model with an explicit hydrologic cycle. 1. formulation and sensitivity to model parameter. *J. Geo. Res.*, **99**, pp. 429-441.

[68] Robe F. R. and K. A. Emanuel, 1996: Moist convective scaling: some inferences from three-dimensional cloud ensemble simulations. *J. A. S.*, **53**, pp. 3265-3275.

[69] Robinson W. A., 1987: Two applications of potential vorticity thinking. *J. A. S.*, **44**, No. 11, pp. 1554-1557.

[70] Rotunno R. and K. A. Emanuel, 1987: An air-sea interaction theory for tropical cyclones. Part II: Evolutionary study using a nonhydrostatic axisymmetric numerical model. *J. A. S.*, **44**, pp. 542-561.

[71] Rotunno R., J. B. Klemp and M. L. Weisman, 1988: A theory for strong, long-lived squall lines. *J. A. S.*, **45**, pp.463-485.

[72] Semazzi F. H. M., V. Mehta, and Y. C. Sud, 1988: An investigation of the relationship between sub-Sahara rainfall and global sea surface temperatur es. *Atmos.-Ocean*, **26**, pp. 118-138.

[73] Semazzi F. H. M., N.-H. Lin, Y.-L. Lin, and F. Giorgi, 1993: A nested model study of Sahelian climate responses to sea-surface temperature anamolies. *Geophys. Res. Letts.*, **20**, pp. 2897-2900.

[74] Simmons A. J., 1977: A note on the instability of the African easterly jet. *J. A. S.*, **34**, pp. 1670-1674.

[75] Stark T. E., 1976: Wave-CISK and cumulus parameterization. *J. A. S.*, **34**, pp., 1670-1674.

[76] Stevens D. E., R. S. Lindzen and L. J. Shapiro, 1977: A new model of tropical waves incoporating momentum mixing by cumulus convection. *Dyn. Atmos. Oceans,* **1**, pp. 365-425.

[77] Stevens D. E. and R. S. Lindzen, 1978: Tropical wave-CISK with a moisture budget and cumulus friction. *J. A. S.*, bf 35, pp. 940-961.

[78] Stevens D. E., 1979: Vorticity, momentum, and divergence budgets of synoptic-scale wave disturbances in the tropical eastern Atlantic. *Mon. Wea. Rev.*, **107**, pp. 535-550.

[79] Thompson R. M., Jr., S. W. Payne, E. E. Recker and R. J. Reed, 1979: Structure and properties of synoptic-scale wave disturbances in the intertropical convergence zone of the eastern Atlantic. *J. A. S.*, **36,** pp. 53-72.

[80] Thorncroft C. D. and H. A. Flocas, 1997: A case study of Sahara cyclogensis. *Mon. Wea. Rev.*, **125**, pp. 1147-1165.

[81] Thorncroft C. D. and B. J. Hoskins, 1994: An idealized study of African easterly waves. I: A linear view. *Q. J. R. Meteorol. Soc.*, **120**, pp. 953-982.

[82] Thorncroft C. D. and B. J. Hoskins, 1994: An idealized study of African easterly waves. II: A nonlinear view. *Q. J. R. Meteorol. Soc.*, **120**, pp. 983-1015.

[83] Wallace J. M., 1970: Time-logitude sections of tropical cloudiness (December 1966-November 1967). ESSA Tech. Rept. NESC **56**, pp 37.

[84] Xu K.-M. and K. A. Emanuel, 1989: Is the tropical atmosphere conditionally unstable? *Mon. Wea. Rev.*, **117**, pp. 1471-1479.

[85] Zheng X., 1997: Mosit zonally-symmetric models and their applications to west African monsoons. Ph. D. thesis, MIT.